THE PHOTODISSOCIATION OF OCS AND HN_3 : UNDERSTANDING DYNAMICS IN THE FIRST ABSORPTION BAND

A Thesis

by

COLIN J. WALLACE

Submitted to the Office of Graduate and Professional Studies of
Texas A&M University
in partial fulfillment of the requirements for the degree of

DOCTOR OF PHILOSOPHY

Chair of Committee,	Simon W. North
Committee Members,	George R. Welch
	David H. Russell
	Dong H. Son
Head of Department,	Simon W. North

December 2019

Major Subject: Chemistry

ABSTRACT

This dissertation is focused on describing the photodissociation dynamics of both OCS and HN_3 in the first UV absorption band. The photodissociation of OCS in the first UV absorption band has continuously been a test case for theoretical models. Experimental measurements using Velocity Map Ion Imaging (VELMI) at 214 nm uncovered previously unseen vibrational excitation of the CO fragment. The photodissociation of OCS is known to result in a j-dependent β parameter. The origin of the j-dependence has been hypothesized to occur via two different mechanisms: a two electronic state model and a non-axial recoil model. This work has confirmed the origin of the j-dependent β originates from two nearby electronic states, the A($2^1A'$) and B($1^1A''$) electronic states, of OCS with opposite symmetry. Using these measurements in addition to experimental data from the literature the fractional contributions of each state excited state is determined. The contribution of the B state (f_B) did not agree well with theory over the first absorption band. Additionally, experimental measurements at 214 nm have indicated an underestimation in the surface hopping trajectories in the photodissociation of OCS, possibly originating from discrepancies in the calculated initial impulse along the bending coordinate or the coupling between the ground X($1^1A'$) and A($2^1A'$). The photodissociation of HN_3 in the first UV absorption band near 256 nm, 271 nm, and 285 nm were measured using VELMI. A series of images across the HN rotational distribution were collected at each wavelength. The experimental measurements at 285 nm are in good agreement with previous measurements in the literature. Speed dependent vector correlations were successfully measured using the recently developed 2+1 REMPI equations. The speed dependent vector correlations measured from the HN fragment provided insight into the correlated dynamics of the N_2 cofragment. The speed dependent vector correlations at 285 nm indicated the low j_{N_2} originated primarily from the ν_5 in plane bend, with increasing dependence on the ν_6 torsion with increasing j_{N_2} . In the future, additional measurements of the N_2 fragment using a 2+2 REMPI scheme at 283 nm are possible. Ion images of the N_2 fragment would allow for the direct determination of the N_2 vector properties providing a way to validate the speed dependent vector

correlations measured using the 2+1 HN REMPI scheme at 285 nm. Additional measurements at 256 nm and 271 nm are necessary to determine the accuracy of the vector correlations in the current data.

Keywords: Photodissociation, VELMI, vector correlations

DEDICATION

I dedicate this work to my mentor and friend Dr. Daniel Havey. He taught me the how to think like a scientist and provided me with the foundation to reach my goals. His memory continuously inspires me to improve myself, take nothing for granted, and appreciate the wonders that surround us each day.

ACKNOWLEDGMENTS

First thank you to my advisor Dr. Simon North for always guiding me back to the right path and for motivating me in my times of need. Graduate school is a long road and I will forever be appreciative of your thoughtful guidance both personally and professionally. I would not stand where I am today without your help.

Thank you to my Mom and Dad for always being there to support me in my times of need. I know the road through graduate school was hardly the journey that I envisioned, so thank you for always being my parents. I truly thankful to know that I always have your support.

Thank you to my other parents Shawn and Cindy Pace. You both helped support me through some of the toughest years of my life. You provided me with peace of mind when I was in need. I am happy to have you both as my parents.

Wei and Carolyn thank you both for all of your help through graduate school. You have helped me more than you can possibly know.

Thank you to Dr. George C. McBane. You guidance during our collaboration was immensely valuable to me. Your meticulous nature taught me the finer details of being a scientist and I am forever grateful to all of the advice you shared with me.

The biggest thanks goes to my wife, Emma. Without your unfaltering love and support for me I surely would not have made it through graduate school. Knowing you are at my side through all the ebbs and flows of life provides me with an inner peace that I draw my strength from. You are my foundation and I love you.

CONTRIBUTORS AND FUNDING SOURCES

Contributors

This work was supported by a thesis committee consisting of Professor Simon W. North, David H. Russell, and Dong He Son of the Department of Chemistry and Professor George R. Welch of the Department of Physics. The OCS work was conducted in collaboration with Carolyn E. Gunthardt. Helpful discussions with Dr. Wei Wei were an essential to understanding some of the OCS experimental data. The HN_3 work was conducted in collaboration with Nick Shuber.

The theoretical trajectory calculations in the OCS results and discussion section were conducted by Dr. George C. McBane of the Department of Chemistry at Grand Valley State University.

All other work conducted for this dissertation was completed by the student independently under the advisement of Dr. Simon North of the Department of Chemistry.

Funding Sources

This work was made possible by the Department of Chemistry at Texas A&M University and the Robert A. Welch Foundation under Grant Number: A-1405.

NOMENCLATURE

VELMI	Velocity Map Ion Imaging
TMP	Turbo Molecular Pump
PDL-1	Pulsed Dye Laser 1
WEX	Wavelength Extender
S/N	Signal-to-Noise
StP	Speed-to-Pixel
POP	Polar Onion Peeling
TST	Transition state theory
QCT	Quasi-classical trajectory
β	Image Anisotropy
$\beta_{\mu j}$	Bipolar moment - Alignment Parameter
$\beta_{\mu v}$	Bipolar moment - Spatial Anisotropy
β_{vj}	Bipolar moment - Forces and torques during dissociation
j_{CO}	Rotational angular momentum of CO
j_{HN}	Rotational angular momentum of HN_3
$j_{\mathrm{N_2}}$	Rotational angular momentum of N_2

TABLE OF CONTENTS

Page

LIST OF FIGURES

FIGURE Page

LIST OF TABLES

TABLE Page

1. INTRODUCTION

1.1 Background[1]

Chemical dynamics is the study of elementary chemical reaction mechanisms in the gas or condensed phase. The goal when studying chemical dynamics is the development of predictive models using a variety of theoretical methods, while experimental measurements are used as a rigorous test of these models. Gas phase chemical dynamics can be broken down into one of two categories: unimolecular and bimolecular reactions. Photodissociation, a unimolecular reaction, can be described as the breaking of one or many bonds in a molecule caused by the absorption of light. The absorption of light can either be the absorption of a single photon or multiple photons. When a molecule absorbs a photon(s) several different processes can occur: the molecule can then emit a photon (fluorescence), nonradiatively relax back to its lowest energy state (quenching), or if the the energy of the photons(s) exceeds the dissociation energy of the weakest bond the molecule can break along that bond resulting in two or more photofragments.[1, 32] Each of these pathways can been seen in Figure 1.1 adapted from Ref. [1]. The work in this thesis is focused on the photodissociation pathway.

[1]Reprinted with permission from Photodissociation Dynamics: Spectroscopy and Fragmentation of Small Polyatomic Molecules by Reinhard Schinke, Cambridge University Press, Cambridge United Kingdom. 1993, University of Cambridge.

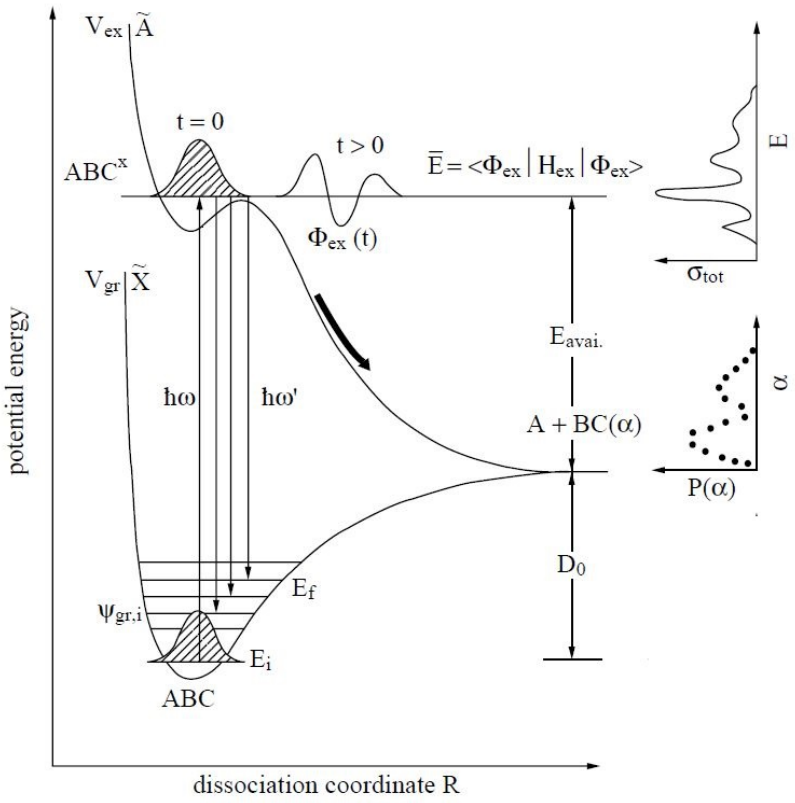

Figure 1.1: A schematic of the excitation of a general triatomic molecule (ABC), from the ground $\tilde{X}$ state to the excited $\tilde{A}$ state, using a single photon($\hbar\omega$) is shown above. Once excited, ABC^X can go through one of three different pathways: ABC^X can go through the fluorescence pathway where a photon($\hbar\omega'$) will be emitted and ABC^X return the $\tilde{X}$, ABC^X can be quenched and non-radiatively relax back to the $\tilde{X}$, or ABC^+ can break apart to A and BC(α) photofragments where $P(\alpha)$ refers to a probability of occupying the α quantum state of the BC photoproducts. This figure is adapted from Ref. [1].[1]

In order to understand the photodissociation dynamics of a reaction it is both necessary to understand the dynamics of the state the dissociation is taking place on, either the excited or ground state, as well as the photoexcitation process. The dynamics of the excited state can be investigated by using photodissociation as a spectroscopic tool referred to as 'asymptotic spectroscopy'. A plethora of information can be determined by looking at the photofragments: the nature of the excited state or states involved in the dissociation process, the life time of the molecule in the excited state(s), what bond(s) break and the nature of the bond breaking process (concerted or multiple steps), as well as the energy partitioning of the available energy after dissociation which

can simply be described by Equation 1.1,

$$E_{avail} = h\nu - D_0 \tag{1.1}$$

where $h\nu$ is the energy of the dissociation photon, D_0 is the dissociation energy of the bond that is broken, and E_{avail} is the total energy available after the bond is broken.[1]

The answer to many of these questions will be explored for two molecules of interest: carbonyl sulfide (OCS) and hydrazoic acid (HN_3). The experimental method, centered around 1-color 2+1 Resonance Enhanced Multiphoton Ionization (REMPI)[2], coupled with the 2+1 REMPI equations developed previously are employed in an effort to grasp both the limitations and advantages of this technique to understand the photodissociation dynamics of small molecules not just at single wavelengths, but across entire absorption bands.

1.1.1 Carbonyl Sulfide (OCS)[3]

Carbonyl Sulfide (OCS) is a linear triatomic molecule and is the most abundant sulfur containing compound in Earth's atmosphere.[33] OCS is produced by a variety of both anthropogenic and natural sources such as fossil fuel combustion, volcanic activity, forest fires.[34, 35] OCS has a lifetime of ~2 years in the troposphere which allows transportation to the stratosphere where OCS is much longer lived. OCS is a sink for OH radical in the stratosphere, $k = 2 \pm^{0.4}_{0.8} \times 10^{-15}$ where it reacts to form SO_2 which in turn reacts to form a variety of sulfur containing aersols.[36, 37, 38]

The photodissocation of OCS has been studied dating back to the early 1930's by Locte-Holtgreven and Bawn who concluded that the principal products of the photodissociation of OCS at 255 nm were ground state CO($^1\Sigma^+$) and excited sulfur(^1D).[39] The sulfur branching ratio was later refined to a 0.95:0.05 S(^1D):S(^3P) at 223 nm.[40] These two reaction paths can be seen below in Equations 1.2 and 1.3.

[2]Resonance Enhanced Multiphoton Ionization is described in depth in section 2.2.2 experimental section

[3]Reprinted with permission from Ultraviolet photodissociation of OCS: Product energy and angular distributions by G.C. McBane; J.A. Schmidt; M.S. Johnson; R. Schinke, 2013. Journal of Chemical Physics, 138, 094314, Copyright [2013] by AIP Publishing LLC

$$OCS + h\nu \rightarrow CO(^1\Sigma^+) + S(^1D)\ [95\%] \tag{1.2}$$

$$OCS + h\nu \rightarrow CO(^1\Sigma^+) + S(^3P)\ [5\%] \tag{1.3}$$

The first absorption spectrum of OCS was detected in 1939 by Forbes and Cline who detected a broad absorption near 220 nm.[41] Later studies revealed weak vibrational structure in the absorption spectrum.[42, 16]

The photodissociation of OCS in the stratosphere occurs via the first UV absorption band.[42] The first absorption band is primarily composed of four different electronic states: $2^1A'$, $1^1A''$, $2^1A''$ and $2^3A''$. These states will be referred to as the A($2^1A'$), B($1^1A''$), C($2^1A''$) and c($2^3A''$) states, following the naming of Schmidt *et al.* (Ref [4]). Both the A and B states of OCS are dissociatve states which are the main contributors to the absorption cross section in the first absorption band, while both the C and c states of OCS are bound states which are responsible for the superimposed vibrational structure of the first absorption band. The calculated and experimental absorption cross sections can be seen in Figure 1.2a, a modified version of Figure 2 from ref [2], where the calculated absorption cross section is shown in blue and is scaled by 1.3× to match the experimental absorption spectrum shown in black.

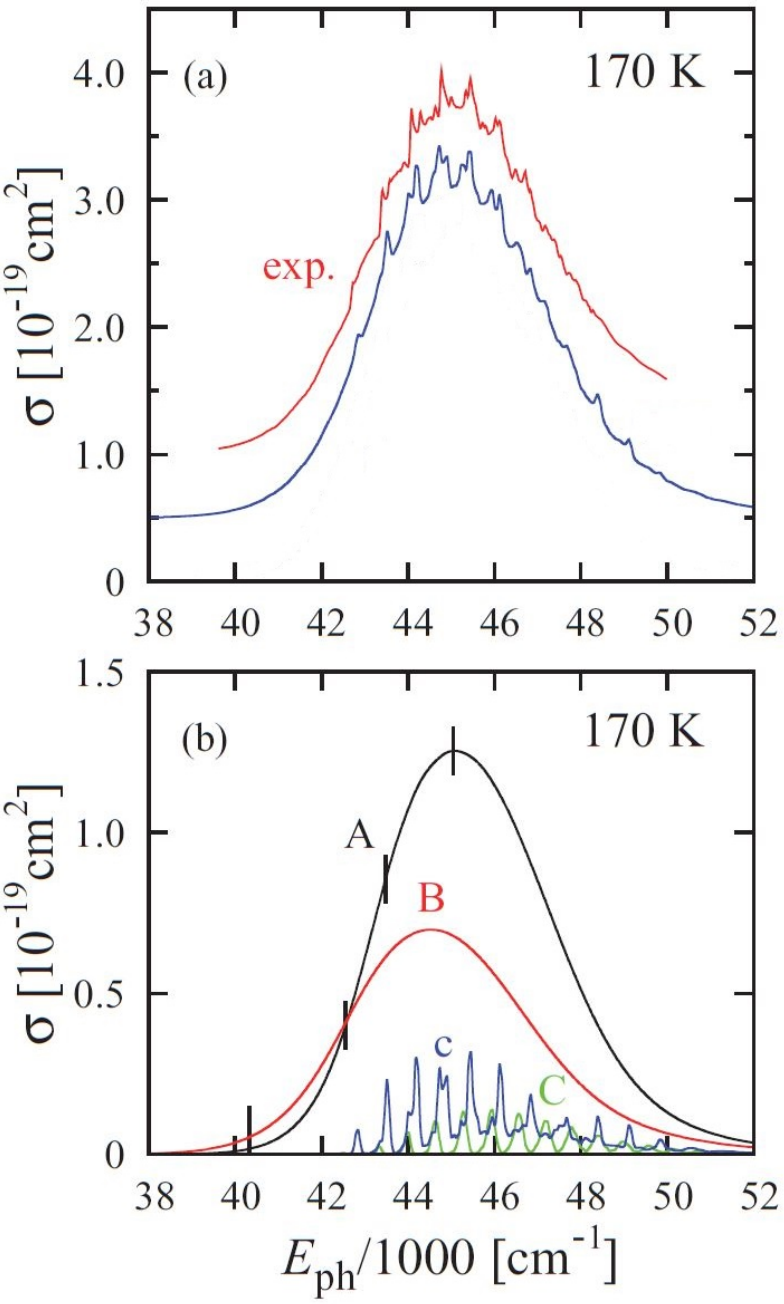

Figure 1.2: (a) The experimental absorption cross section is shown above in black and the calculated absorption cross section is shown in blue. The calculated absorption cross section is scaled by a factor of 1.3× in order to better fit the intensity of the experimental absorption cross section. (b) The A, B, C, and c electronic states of OCS are shown above as black, red, green, and blue respectively. The vertical black bars refer to places where CO rotational distributions have been collected. Experiments at 214 nm are not shown on this figure. This figure is adapted from ref [2].[3]

The theoretical and experimental measurements were conducted measured at 170 K. [2, 16] The individual contributions to the calculated cross section seen are shown in Figure 1.2b where A state is shown in black, the B state is shown red, the C state is shown in green, and the c state is shown in blue. The A and B absorption cross sections are smooth indicative of their dissociative nature, while the C and c states have vibrational structure indicative of their bound nature. The vibrational structure originates from the OC-S stretch coupled with the OCS bend.[4, 2]

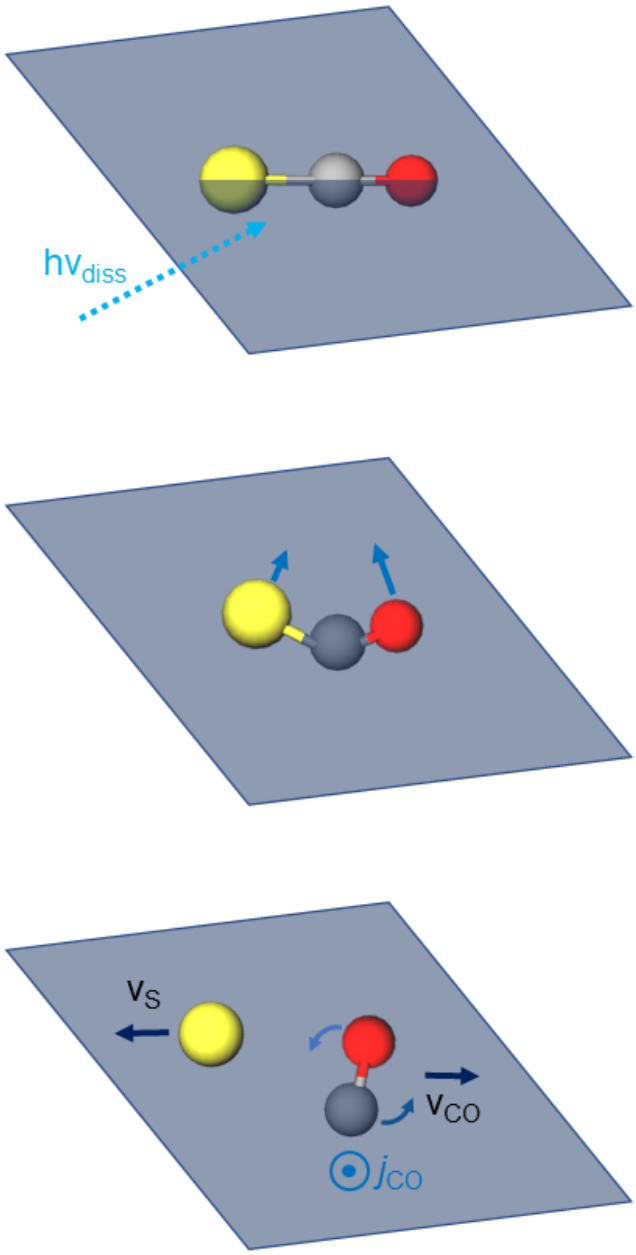

Figure 1.3: The photodissocation of OCS begins with slightly bent OCS in the ground state(X). The OCS molecule is primarily excited to the A or B state by the dissocation laser($h\nu_{diss}$). As the OCS molecule is excited it begins to bend further reaching a bent configuration on both of the A and B excited state potentials. As the OCS molecule is bending on these two electronic states, the OCS molecule is also dissociating. This bending motion during dissociation results in highly excited j_{CO} fragments with near limiting $v \perp j$.

The photodissociation of OCS, in the first absorption band, has remained the focus of many more recent studies.[6, 40, 43, 7, 44, 45, 46, 47, 8, 48] In general, the absorption cross section increases with increased bending in the ground state of the OCS molecule. The photodissociation of OCS results in highly rotationally excited CO product with little vibrational excitation. The high rotational excitation has been attributed to the linear to bent transition in OCS where nearly linear ground state OCS is excited to a bent excited state with a bending angle near 40°.[4, 5, 6] A schematic of the excitation and subsequent dissociation of OCS is shown in Figure 1.3. The calculated excited state surfaces of the A and B states of OCS are shown in Figure 1.4. The A, B, and X electronic states at a bending angle ($\alpha = 0°$) are shown in Figure 1.4a and at a bending angle of 15° ($\alpha = 0°$) in Figure 1.4b.[3]

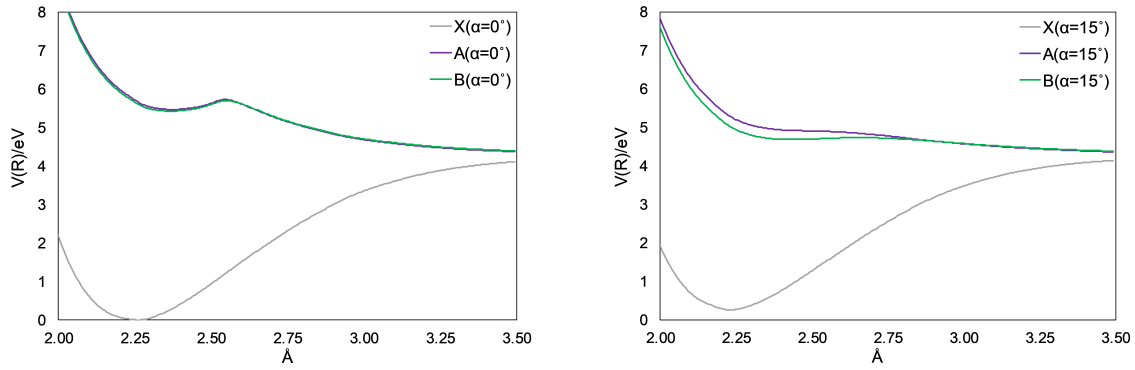

Figure 1.4: Modified CO potentials for the X, A, and B states of OCS used for the quasi-classical trajectory (QCT) calculations shown in Section 3. The X, A, and B states are shown as black, red, and green curves. (a) The modified OCS potentials at a bending angle $\alpha = 0°$. (b) The modified OCS potentials at a bending angle of $\alpha = 15°$. This figure is adapted from the supplemental section of Ref. [3].

The rotational state distribution is bimodal at longer photolysis wavelengths near 248 nm and merges into a single distribution with a small shoulder near 214 nm.[5, 7, 22] The origin of this bimodal distribution is presently understood to originate from three different dynamical pathways. The lower CO fragment angular momentum (j_{CO}) portion of the distribution is a mixture of OCS molecules that dissociation on the A and B state surfaces, while the high j_{CO} part of the distribution

is the result of a surface hop from the A state to the X state of OCS. The OCS molecules that dissociation on the A and B state experience a restoring force reducing the intensity of the bending motion of the OCS molecule and thus the final j_{CO} . The OCS molecules that surface hop do not experience the restoring force on the A or B surface. The CO fragments originating from OCS molecules that surface hop are responsible for the highest populated states in the CO rotational distribution. OCS molecules that hop from the A to X state will be labels as (X) for the rest of this work. In addition to the product distribution, the angular distribution resulting from the photodissociation of OCS and have shown a strong dependence of the β parameter with respect to the j_{CO} .[40, 43, 46, 8, 47, 22, 49, 3] The vibrational excitation of OCS has been measured at various wavelengths ranging from 193 nm to 248 nm. The fraction of CO($v = 1$) increases with photolysis energy between the range of 214 nm to 248 nm.[22, 50, 44, 46, 6] This result is currently not well understood. One would not expect much vibrational excitation of the CO fragment since the CO bond length is only 3% shorter than the CO bond length in the OCS.

Several theoretical studies have been conducted in an effort to understand these numerous experimental observations.[5, 4, 2, 51, 52] Initial studies of the j-dependent β parameter attributed the varying β to a two state model.[6] The β parameter (anisotropy paramter) can be defined as

$$I(\theta) \propto 1 + \beta P_2(cos\theta) \tag{1.4}$$

where $P_2(cos\theta)$ is a Legendre polynomial and θ is the angle between the fragment velocity and electric field vector. For a parallel transition β = 2 and for a perpendicular transition β = -1.

As the OCS molecule bends in the ground state, the symmetry of bent OCS can be described as an A' state, while the A state is A' symmetry and the B state is A'' symmetry. Both the A and B electronic states of OCS are at approximately 5 eV above X state OCS with a bending angle of $\sim 15^\circ$ which can be seen in Figure 1.4b.[4, 3] Sivakumar *et al.* hypothesized that the slightly bent ground state OCS could undergo two different electronic transitions.[6] OCS could either be excited to the A state, an $A' \leftarrow A'$ transition which is a parallel transition where β = 2, or excited to the B state of OCS, a $A'' \leftarrow A'$ transition which is a perpendicular transition where β = -1.

The varying β parameter as a function of j was concluded to be the result of excitation to both electronic states where the ratio of the excitation between the two states could be compared using the measured β value. Sivakumar *et al.* presented the fraction of dissociative events occurring on the A state as f which was shown to smoothing increase from $j_{CO} = 50$ to $j_{CO} = 68$.[6]

In 2007, Brouard *et al.* proposed a new hypothesis using a single state model. Excitation to the B state was determined to be insignificant. The j-dependent β parameter was attributed to large amounts of non-axial recoil of the OCS molecule caused by the transition dipole moment lying far away from the linear OCS axis ($\geq 60°$).[8] In order to achieve good theoretical agreement between their geometric model and experimentally measured β parameters, the transition dipole moment (TDM) for the A state was set to orientation far from the molecular axis (108° at 230 nm).[8] The later work of Schmidt *et al.* in 2012 confirmed the result of a one state dissociation process.[4] The calculations presented by Schmidt *et al.* concluded that the TDM of the A state was responsible for the majority of the contribution to the cross section of the first absorption band. The difference between the A and B TDMs resulted in an A state absorption cross section that is $\sim 20\times$ larger than the B state.[4]

In a subsequent study, McBane *et al.* (identical authors as Ref. [4]) revised their TDM functions and electronic potentials.[2] This new work concluded the j-dependent β parameter was likely to be cause by a two state model, a complete reversal from their earlier work and a return to the original two state theory. The recalculated TDMs indicated an A:B absorption cross section ratio of $\sim 2:1$ down from $\sim 20:1$ at the peak of the first absorption band. This revised work refuted the non-axial recoil explanation presented by Brouard *et al.* and instead confirmed the original two state hypothesis proposed by Sivakumar *et al.* in 1987.[6]

These new calculations also attempted to describe both the rotational and vibrational product distributions across the first absorption band. The trajectory calculations predicted that the CO($v = 1$) population should be small, but increase with increasing energy. The CO($v = 1$) population increased from 0.023 at 248 nm to 0.135 at 222 nm.[2] An additional value of 0.132 CO($v = 1$) at 214 nm was published later.[22] The rotational distributions predicted by the trajectory calculation

resulted in qualitatively similar distributions, but systematically resulted in j_{max} values that were $\sim 3j$ higher than the experimentally measured distributions. In order to correct for the systematically high j-distribution, an *ad hoc* correction was applied to the potential energy surface to increase the restoring force in exit channel of the potential energy surface to further reduce the rotational excitation of the CO fragment. The restoring force can be explained as force that the OCS molecule experiences if the bending angle becomes too acute. If the OCS bending angle becomes too narrow, the O and S atoms will repel each other resulting in a reopening of the OCS bond angle which in turn reduces the rotational excitation of the CO fragments. This empirical correction helped the trajectory calculations better agree with the experimentally derived rotational populations, but worsens the further away the dissociation energy is from 235 nm, where the "ad hoc" correction team was applied. This is expected since the restoring force is wavelength dependent.[2]. The calculated and experimental rotational distributions can be seen in Figure 1.5.[4]

[4]The 214 nm data is not shown until later. This figure was generated through a private communication with Dr. McBane prior to the experiment.[9]

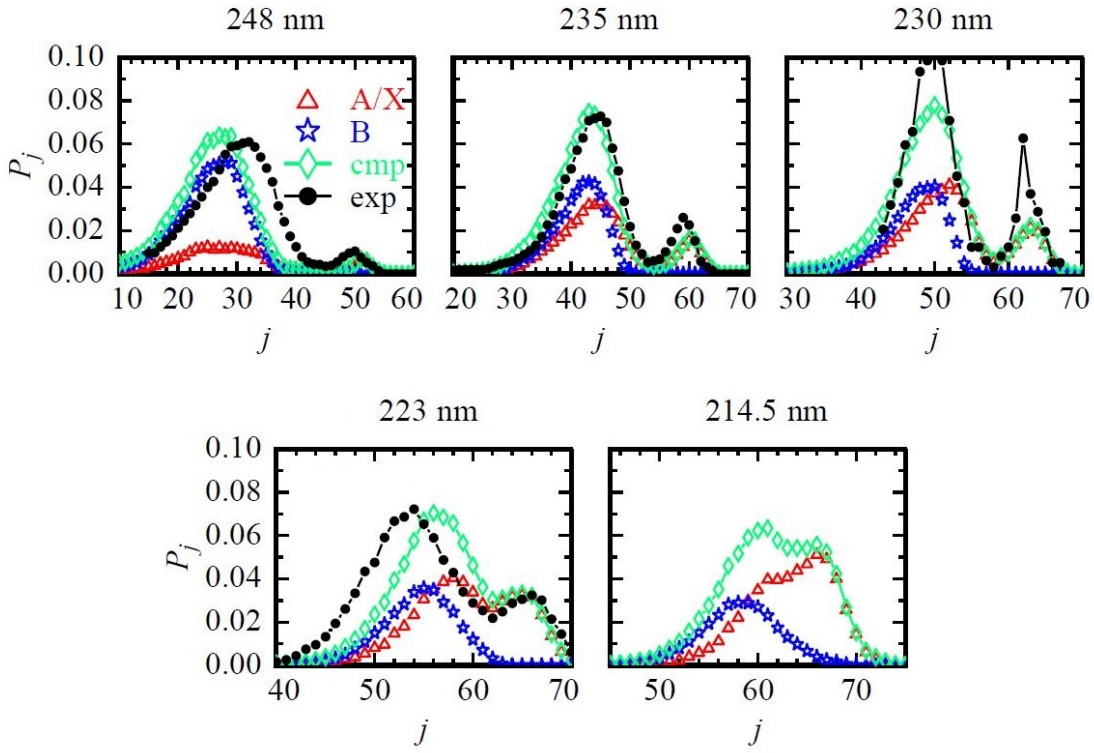

Figure 1.5: Both simulated and experimental rotational distributions at 248 nm, 235 nm, 230 nm, 223 nm, and 214.5 nm. The red triangles correspond to the CO fragments that started on the A state surface, blue starts correspond to the CO fragments that started on the B state, green diamond correspond to the sum of A and B populations, and the black circles correspond to the experimental data. Measurements at 214.5 nm will be presented in depth in the results and discussion section.[4, 5, 6, 7, 8, 9]

The goal of this work had three main objectives: first to use experimental measurements to confirm the two state model used to describe the j-dependent β, to extract rotational populations from the photodissocation of OCS near 214 nm in order better understand the effectiveness of the *ad hoc* correct term applied to the potential energy surfaces at a wavelength further from 235 nm, and finally to experimentally deconstruct the first absorption band into the contributions from the A and B electronic states in order to compare to the theoretically determined absorption cross sections.

1.1.2 Hydrazoic Acid (HN_3)[5]

Hydrazoic acid is a four atom molecule that is formed in the atmosphere primarily by the protonation of NaN_3 an increasingly common pollutant due to both the proliferation of airbags, its increased usage in airbags as a propellant, and the lack of proper disposal procedure for airbags. The peak of the HN_3 absorption falls below 200 nm with a secondary shoulder at ~262 nm. Despite this, HN_3 can be photolyzed in the troposphere by the sun resulting in a half life of 2-3 days. The absorption cross section of HN_3 and vs the solar flux can been seen below in Figure 1.6.

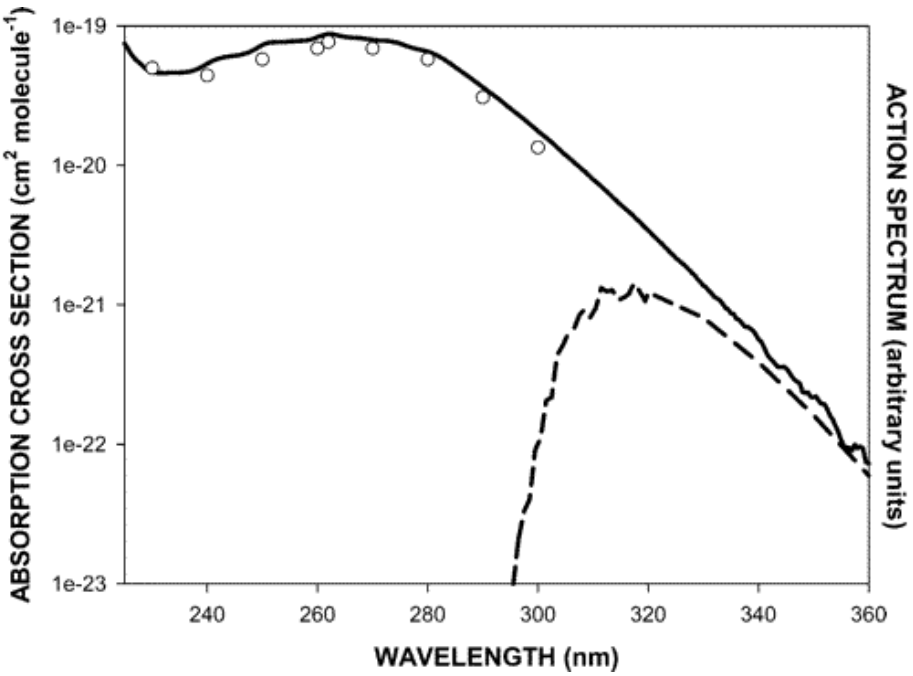

Figure 1.6: The UV absorption spectrum for HN_3 is shown as a solid black line. This experimental spectrum is compared to the work of McDonald *et al.* which can been seen as open circles.[10] It was necessary to scale the data as previously suggested by Rohrer *et al.* to achieve good agreement between the two absorption measurements.[11] These two experimental spectra were collected at room temperature. The dotted line is an action spectrum of HN_3 the surface of the Earth. This action spectrum describes the relationship between the actinic flux and the absorption cross section of HN_3 as a function of wavelength. This figure is adapted from Ref. [12].[5]

[5]Reprinted with permission from Atmospheric Chemistry of Hydrazoic Acid (HN3): UV Absorption Spectrum, HO Reaction Rate, and Reactions of the N3 Radical by J.J. Orlando; G.S. Tyndall; E. A. Betterton; J. Lowry; S.T. Stegall, 2005. Environmental Science and Technology, 39, 1632, Copyright [2005] by American Chemical Society

HN_3 is a sink for the OH radical ($k = 1.3x10^{-12}$ cm^{-1}) to form water and azide radical ($\cdot N_3$). The azide radical subsequently reacts with oxygen to form NO_X.[53, 12] HN_3 is a liquid at room temperature and is an extremely sensitive explosive. The two main photodissociation pathways of HN_3 ,

$$HN_3 + h\nu \rightarrow \cdot HN(a^1\Delta) \ + \ N_2 \tag{1.5}$$

$$HN_3 + h\nu \rightarrow \cdot H \ + \ \cdot N_3 \tag{1.6}$$

where channel 1.5 is formed in unity at $\lambda \geq 248$ nm and is the main reaction pathway from 193 nm to 248 nm. Other electronic states of HN have been detected at $\lambda \leq 193$ nm.[54, 55, 56, 11] The quantum yield for the formation of the H-atom has been measured at three different wavelengths: $\phi_{193} = 0.14, \phi_{248} = 0.20$ and $\phi_{266} = 0.04$.[57, 58]

The photodissociation of HN_3 has been of interest to the dynamics community for several decades dating back to the 1960's due to the observation of Λ-doublets preferences in the HN photoproducts, the excitation and dissociation of the central N=N bond, and due to its difficulty to theoretically model.[26, 24, 59, 60, 61] The photodissociation of HN_3 and subsequent detection of HN radical is one of the earliest radicals studied in a supersonic beam and the first experimental molecule to indicate the fragment distribution depends on the initial state of the precursor or parent molecule.[62] In Dekoven and Baronavski, nascent NH resulting from the photodissociation of HN_3 was detected using LIF where HN_3 was dissociated in both a static gas bulb and a supercooled beam. The resulting rotational distributions of the HN fragment were shown to depend on the internal energy of the parent HN_3 molecule.[62]

The stereodynamics of the photodissociation of HN_3 has been described at several wavelengths in the first absorption band by primarily probing the HN fragment. NH rotational distributions have been measured at three different wavelengths 248 nm, 266 nm, and 308 nm.[11, 24, 26, 63] Additionally there has been one measurement of the N_2 rotational distributions at 283 nm.[25] Typically when beginning an experiment it is preferable to chose the fragment with the larger fragment rota-

tional angular momentum (j), which in the case of the photodissociation of HN_3 is the N_2 fragment. The fragment with larger j will be less susceptible to effects from the angular momentum of the parent molecule. However probing the N_2 is difficult due to its high ionization energy which necessitates the use of an extra ionization photon, requiring a 2+2 REMPI scheme.[64] Additionally there is an intense background at m/z = 28 due to the high power required by the probe laser to use a 2+2 REMPI scheme.[25] Attempts have been made to characterize the vector correlations by probing the N_2 fragment, but due to the large background and to the nature of one-color experiments, where the polarization of the pump vs. probe lasers can not be changed, it was not possible to quantitatively describe the dynamics of the HN_3 dissociation.[25] The rotational excitation of the HN fragment is modest peaking around j_{HN} = 5-6 and both the rotational distribution and translational energy of the HN fragment are largely invariant with respect to the dissociation wavelength. The N_2 rotational distribution is much more excited compared the HN cofragment. Unlike the HN rotational distribution, the rotational distribution of N_2 does vary with respect to the dissociation wavelength. The most populated j_{N_2} , $\langle j_{N_2} \rangle$ is equal to 37, 56, and 73 at 308 nm, 266 nm and 248 nm respectively.[65] The significant excitation of the N_2 fragment requires a strong bending motion in either along the NNN bond either by the in-plane NNN bend (ν_5) or the NN-NH torsion (ν_6).[65] A schematic of the dissociation of HN_3 is shown below in Figure 1.7.

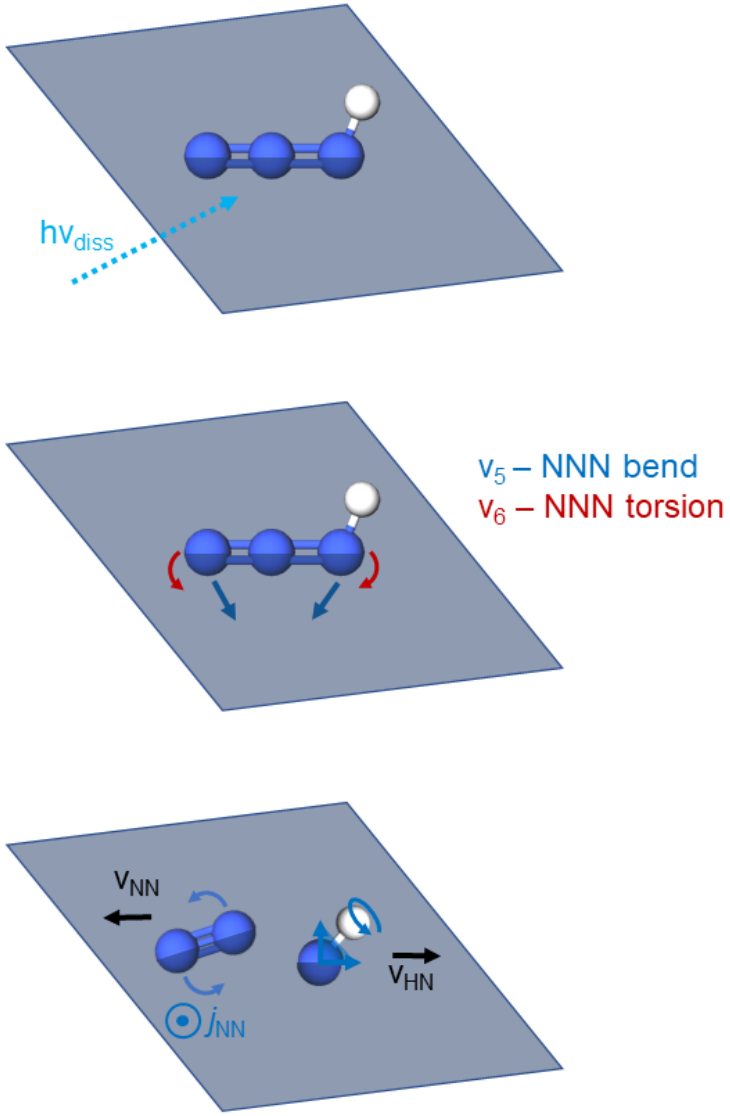

Figure 1.7: A schematic of the bond breaking of HN_3 . When the HN_3 molecule is excited, it begins to bend either through the in-plane NNN bend (ν_5) or the NN-NH torsion (ν_6). Due to the multiple possible bending motions, the rotation of the HN fragment is poorly defined and on average rotates near a 45° angle. The these two vibrational motions result in very strong rotational excitation of the N_2 fragment.

The HN fragment can be excited up to $\nu = 3$. The $\nu = 1$ population has a bimodal structure peaking near the dissociation wavelengths of 235 nm and 245 nm. The relative population of the NH($v = 1$)/NH($v = 0$) can be seen in Figure 1.8 below.[13] The vibrational excitation could be

explained by a strong change in the NNN-H bond in the exit channel of the HN_3 ($\tilde{A}^1A''$) surface, but the vibrational excitation of the NH fragment has not been described theoretically.[66, 57, 13]

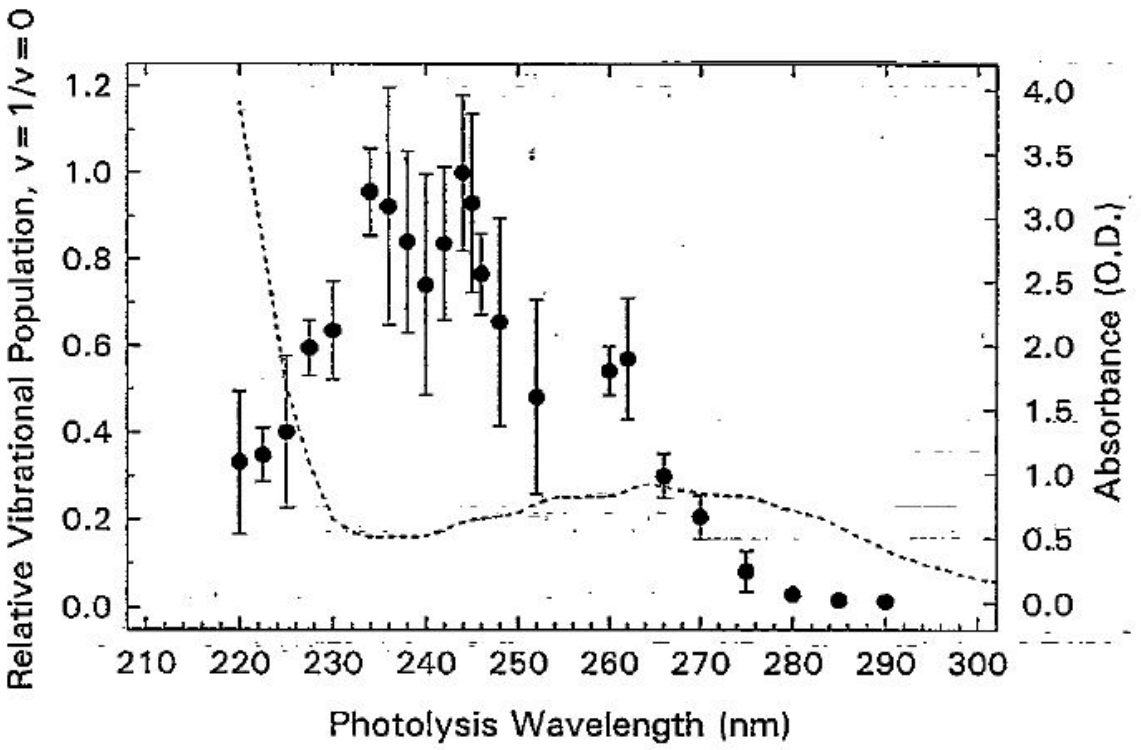

Figure 1.8: Above is a plot of the NH($a^1\Delta$) $v = 1/v = 0$ state over a range of photolysis wavelengths. The dotted line refers to the absorption spectrum of HN_3 . This figure is adapted from Ref [13].

Unlike the HN fragment, the N_2 fragment is not vibrationally excited. This is an expected result since the N-NNH bond length is nearly the same in the ground HN_3 ($\tilde{X}^1A'$) as the HN_3 ($\tilde{A}^1A''$) excited state. The dissociation time of HN_3 is $\leq$ 100 fs. This short lifetime implies a direct dissociation on the excited state surface. There is likely a small barrier on the the excited state surface based on the small oscillations observed in the absorption spectrum.[54, 65]

The primary goal of this work was to test the 2+1 equations and one-color 2+1 REMPI experimental method to accurately measure speed-dependent vector correlations. Due to the difficulties

associated with probing the N_2 fragment, it is difficult to determine the stereodynamics of the N_2 fragment directly. Instead, by using velocity map imaging, HN_3 images can be analyzed as a function of the radius to determine the stereodynamics of its N_2 co-fragment. Secondly, this work will serve to fill in large gaps between the dissociation wavelengths that have been investigated in the literature which will help validate the theoretical understanding of the dissociation dynamics of HN_3 .

The rest of this dissertation is organized into a three chapters. The first chapter describes the experimental apparatus and data analysis procedure in detail. The second chapter describes the experimental finding from the OCS study and the preliminary results from the HN_3 study. Briefly, the OCS study found decrepancies between the theoretical estimates and the experimental in both the surface hopping component and the contributions from the B state of OCS. The preliminary results from the HN_3 study have demonstrated the ability to measure speed dependent vector correlations using the data analysis method developed for the OCS experiment. Finally there is an appendix reviewing attempted experiments involving acetaldehyde and ketene where both experiments were limited due to a pulse valve dependent, non resonant CO signal.

2. EXPERIMENTAL

2.1 The VELMI Instrument

The velocity map ion imaging (VELMI) is a powerful analytical technique that can be used to investigate the energetics and photodissociation dynamics of small molecules. Several experimental conditions must be met in order to perform these experiments. First the experiment must be conducted in a collision free environment. Using a combination of rotary, diffusion, and turbomolecular pumps (TMP) the pressure is reduced to the 10^{-7} torr regime, in the region where the photodissociation takes place, where the mean free path of molecules (10^{9-10} molecules/cm^2) is far greater than the distance to wall ($\lambda > 1$ km). Secondly, it is necessary to mitigate any out-of-plane ($x - y$) velocities with respect the time-of-flight z-axis in order to measure the dynamics of the photofragmentation process. Using the VELMI apparatus, both of these conditions can be satisfied.

The VELMI apparatus consists of three distinct sections: source, main, and detector which can be seen in Figure 2.1. The source region is differentially pumped using a diffusion pump backed by a (Edwards E2M-30) rotary vane pump and is capable of achieving $< 10^{-7}$ torr. The main region is differentially pumped using a turbomolecular pump (Leybold TMP 1000C) and (Edwards E2M-30) rotary vane pump and is capable of achieving $< 10^{-7}$ torr. Using each respective rotary vane pump, the source and main regions are kept at 10^{-3} torr when the instrument is not in operation. The detector region is differentially pumped using a turbomolecular pump (Leybold TMP 151) and (Alcatel 2004A) rotary vane pump. The pressures in this region are maintained at $< 10^{-8}$ torr both during operation and when the chamber is not in operation. When the chamber is on standby a gate valve isolates the detector region from the rest of the chamber (at 10^{-3} torr) allowing the detector region to maintain ultra-high vacuum at all times.

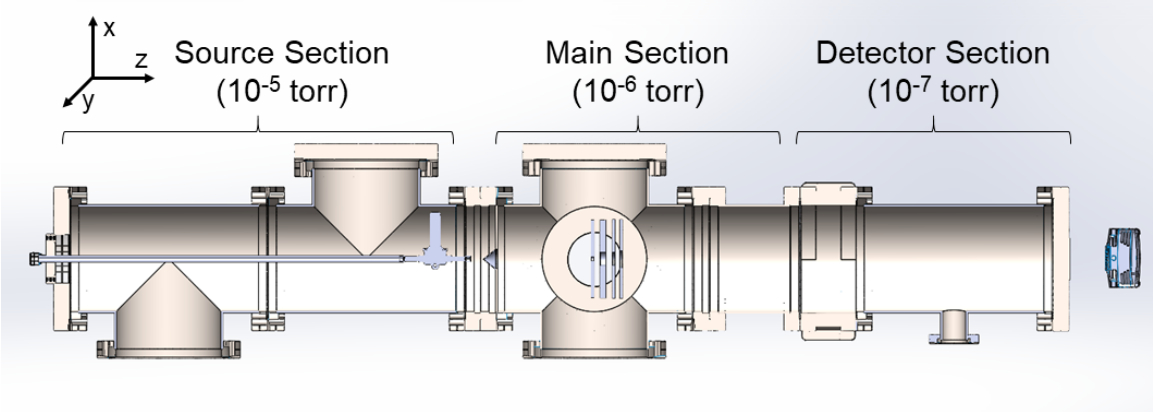

Figure 2.1: A SolidWorks drawing of the VELMI apparatus showing the position of the PV, skimmer, and ion optics. The detection axis (z-axis) is marked on the chamber above. The lab-frame orientation of the x, y, and z axises are shown on the bottom left corner.

The source region contains a General Valve 9 solenoid valve which is pulsed at 10 Hz with an opening time typically around 500 μs. The analyte is first seeded in a buffer gas, typically helium, and then enters the chamber during this 500 μs opening time. The pulse of gas then flows through the electro-form skimmer connecting the source and the main regions of the chamber. This electro-form skimmer has a 0.2 mm diameter opening at the tip. The edges of the opening are razor sharp which helps collimate the pulse of gas entering the main chamber. This collimation is essential to remove any parent molecule with x or y velocity which can convolute the results of the experiment. Once this collimated beam of gas enters the main chamber it is photodissociated by the pump laser and the resulting photofragments are resonantly ionized using the probe laser.

In a typical two-color experiment, the pump beam originates from the pulsed dye laser 1 (PDL-1) side of the chamber while the Scanmate is used as the probe due to its superior scanning capabilities. The lower half of Figure 2.2 shows the pump laser setup where the 150-10 Nd:YAG laser seeds the PDL-1 Dye laser with 532 nm photons with an average power ~300 mJ. The 532 nm photons are converted into tunable light via stimulated emmision of the dye circulating through the PDL-1. Once the tunable light exits the PDL-1 it enters into a wavelength extender (WEX) where the tunable light is frequency doubled by a BBO-I crystal. This tunable UV light is then

sent into the chamber via a periscope which serves two purposes. First the periscope is used to raise the laser beam to the appropriate height and secondly the perpendicular orientation of the mirrors rotates the polarization of the laser 90° from the horizontally polarized light that exits the WEX to vertically polarized light with respect to the detection axis. Similarly the top half of Figure 2.2 shows the probe laser setup where the 230-10 Nd:YAG laser fires an average energy of ~300 mJ/pulse of 355 nm light into the Scanmate dye laser. This light is then converted into tunable wavelengths of light and is also frequency doubled in the WEX using a BBO-I crystal. The probe light also utilizes a periscope to rotate the polarization. In some experiments, a Double Fresnel Rhomb is used to rotate the polarization instead of the periscope. When ~214 nm light was used, it was necessary to use a periscope to change the polarization since it would burn the polarization optics due to the high energy of the ~214 nm photons.[1] Each laser is directed into the chamber via each periscope and is focused into the interaction region inside the main region of the chamber. The pump laser timing is set to reach the interaction region typically between 20-50 ns before the probe laser to ensure the target species is first dissociated then resonantly ionized. In the case of a 1-color experiment the this UV beam originating from the Scanmate would act as both the pump and probe laser simultaneously dissociating and resonantly ionizing the target species.

[1]No polarization optics suitable for 214 nm could be found commericially necessitating the use of this periscop setup where the specially coated 214 nm mirrors could rotate the polarization by 90°.

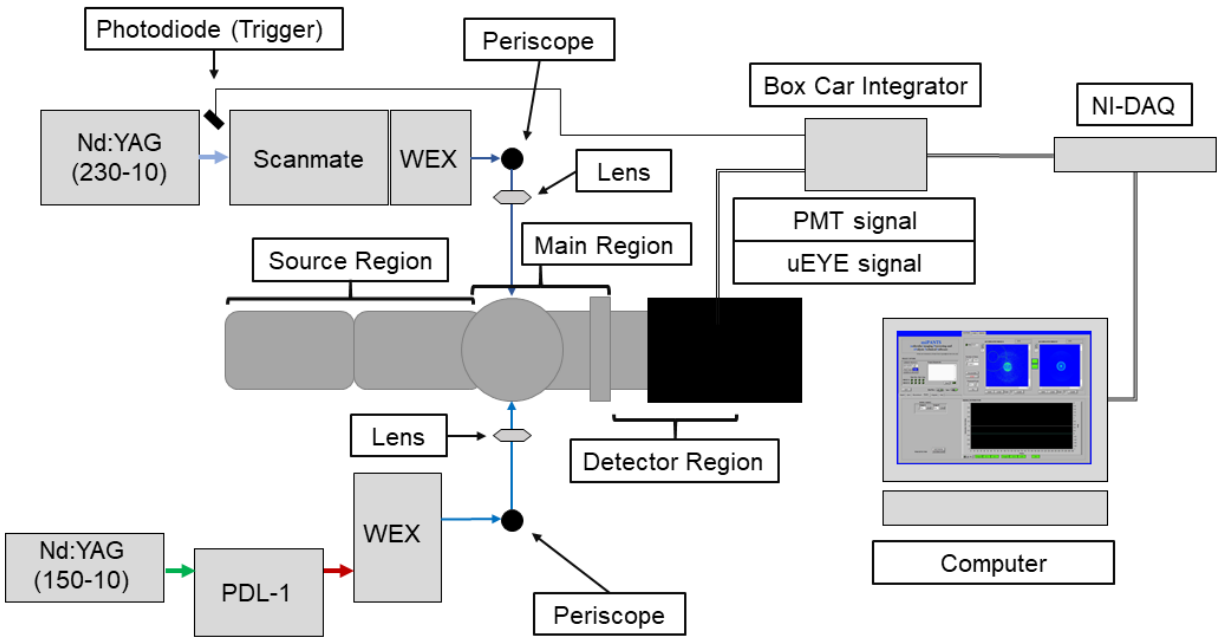

Figure 2.2: Experimental diagram for a two-color experiment.

This newly generated sphere of ions are then accelerated towards the detector and are velocity focused using a series of four Einzel lenses referred to hereafter as as ion optics. The first ion optic, referred to as the repeller (V_R), accelerates the ions toward the detector while the remaining three ion optics, known as lens 1, 2, and 3 (L_1, L_2, L_3), are used to focus the ions. There are two possible configurations for the ion optics, one for crushed imaging and one for DC sliced imaging. These two types of images are explained in more detail in the image analysis section below. In a crushed configuration, only V_R and L_1 are needed for good velocity resolution. In a DC slicing configuration all four optics are used to both temporally stretch the ion cloud as well as accelerated and focus the ions.[67] These accelerated ions are then detected by a pulsed microchannel plate phosphor screen array.

Each ion impact on the chevron stacked microchannel plate array creates a cascade of electrons due to the high applied voltage. The microchannel plates are floated at a voltage of ~1.3 kV and are pulsed up to ~2.4 kV by a DEI PVX-4150 pulser for a duration of 100 ns for crushed images or 40

ns for sliced images. It is necessary to keep the microchannel plate array at a floating voltage due to limitations of the DEI PVX-4150 pulser which is limited to a range of ±1.5 kV. The electrons then exit the microchannel plates and impact the phosphor screen creating a phosphorescent white dot which is recorded by a IDS uEYE CCD camera. The resulting image is an average of tens of thousands of laser shots, each generating ~1000 ions. A Hamamatsu R928 photomultipler tube (PMT) is used to record the total signal from the phosphor screen microchannel plate array. Information about both the energetics and stereodynamics of the photodissociation process is contained inside the radius and angular distribution of each image.

2.1.1 Ion Optics

Before any photodissociation experiments can be conducted the ion focusing conditions of the VELMI apparatus must be determined. Simion® was used to design the VELMI apparatus and simulated various sets of focusing conditions. By varying the applied potentials on each ion optic in Simion® the corresponding electric field is calculated. Using these electric fields, the ion flight paths can be calculated and our focusing conditions can be optimized prior to running a experiment.

In Figure 2.3 the top panel shows a CO ion flight path using crushed imaging conditions (two ion optics) where the V_R = 4000 V and L_1 = 3080 V.[67] In the interaction region shown in the bottom left panel, there are three different ion origin points. Each origin point has 8 ion trajectories each separated by 45°. When the ions impact the detector, shown on the bottom right, each ion with the same x, y velocities are focused onto the same point despite the minor differences in their starting positions. This ion focusing is the velocity mapping in VELMI.[68]

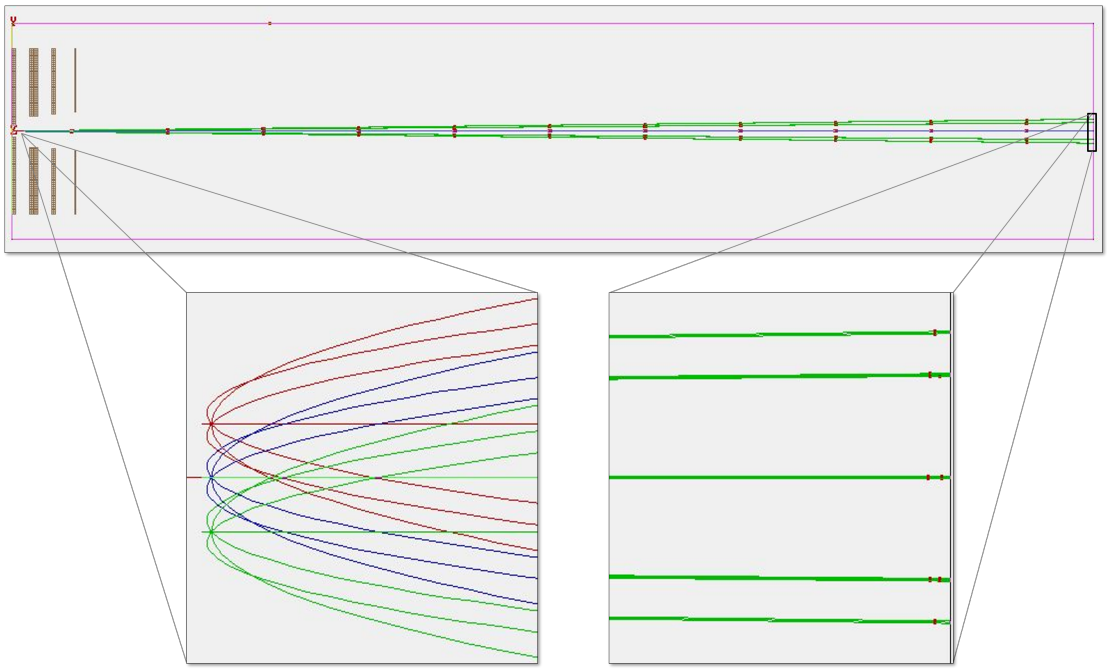

Figure 2.3: An example Simion® simulation of a crushed image ion flight with V_R = 4000 V and L_1 = 3080 V viewed from above the chamber where the interaction region and the detector region are expanded to show the velocity focusing.

2.1.2 Co-propagating vs Counter-propagating Laser Design

Traditionally the North Group conducted all 2-color imaging experiments using co-propagating lasers, meaning both the pump and probe lasers entered the chamber from the same side. In order to achieve this overlap a dichroic mirror was used to allow either the pump or probe laser to pass through the backside of the dichroic mirror with high transmission, while the other laser is reflected off the front of the dichroic mirror. Using this specialized optic, the pump and probe lasers can be overlapped on the dichroic mirror and aligned onto the molecular beam inside the chamber. Both lasers are then focused into the chamber using the same lens.

During the initial OCS experiments, using wavelengths near 214 nm, it quickly became apparent this technique would no longer be viable since wavelengths near 214 nm required specialized coatings and there were no 214 nm dichoric mirrors commercially available. The decision was made to move the VELMI apparatus to make room for a counter-propagating laser system.

Counter-propagation has two distinct advantages over co-propagation: first the experiment is not restricted to pump and probe wavelengths that can be used with a dichroic mirror and secondly two independent focal lenses are used allowing for more flexibility when aligning the two lasers over the molecular beam. The change to counter-propagating lasers opened up a wide range of pump and probe wavelengths that could not previously be accessed.

2.2 Photodissociation and Ionization

The photodissociation and ionization of OCS and HN_3 use a variety of pump probe schemes and the details for each experiment will be presented later in each individual section. In general, each pump and probe scheme is developed with two goals in mind, first to achieve adequate dissociation of the target molecule and second to achieve state selective ionization of one of the photofragments originating from dissociation. In order to state selectively ionize the photofragment of interest, a technique called Resonance Enhance Multiphoton Ionization (REMPI) is used. In the following experiments the pump and the probe laser can be the same laser or two different lasers. Both one-color or two-color experiment were performed. In the case of a one-color experiment a single laser pulse acts to both dissociate the parent molecule and resonantly ionize the selected photofragment. A one-color experiment is often the best place to begin since the alignment required is far simpler than the alignment needed for a two-color experiment. Since the pump beam is not fixed in a one-color experiment, it is necessary to verify the small changes in wavelength do not effect the results of the experiment. In the case of a two-color experiment, the pump and probe laser will require careful alignment to overlap both lasers in space onto the molecular beam inside the main chamber which can be challenging.

2.2.1 Photodissociation

Photodissociation is the process where a molecule interacts with photons and undergoes a chemical bond breaking resulting in two or more fragments. In order for a dissociation reaction to occur, first the photon must be absorbed by the target species and second the photon must contain enough energy to break the a bond in the molecule. It is good practice to determine the percentage

of molecules that can be dissociated using the available experimental conditions prior to attempting an experiment to ensure there are a sufficient number of photofragments for adequate signal. The fraction of molecules dissociated can be readily calculated follow Equation 2.1,

$$f_{diss} = 1 - e^{\frac{\rho \cdot \sigma_{diss}}{A_{spot}}} \tag{2.1}$$

where ρ is the photon density of each pulse from the dissociation laser, σ_{diss} is the absorption cross section at the dissociation wavelength which can typically be found on the Mainz Spectral Database[69], and A_{spot} is the spot size of the dissociation laser in the interaction region where is laser is highly focused.

In order to calculate the area of the laser, the radius of the dissociation laser in the interaction region must first be calculated. Using the Gaussian beam waist equation,

$$2\omega_0 = \frac{4\lambda}{\pi}\frac{F}{D} \tag{2.2}$$

where ω_0 is the Gaussian beam radius, λ is the dissociation wavelength, F is the focal length of the lens, and D is the diameter of the lens.[70]

Once the radius has been determined, the spot is assumed to be a circle and the area is calculated.

The ρ can calculated following Equation 2.3

$$\rho = \frac{E_{measured}}{E_{h\nu}} \tag{2.3}$$

where $E_{measured}$ is the energy of the laser pulse measured by the power meter, in mJ, before entering the chamber and $E_{h\nu}$ is the photon energy of each pulse in mJ/photon. $E_{h\nu}$ can be calculated by following 2.4,

$$E_{h\nu} = \frac{hc}{\lambda_{diss}} \tag{2.4}$$

where h is Planck's constant, c is the speed of light and λ_{diss} is the wavelength of the dissociation laser. For example the fraction of molecules dissociation for OCS at 214 nm can be calculated as follows. First using Equation 2.4,

$$E_{h\nu} = 9.28 \text{ x } 10^{-16}\ mJ\ photon^{-1} = \frac{6.626 \text{ x } 10^{-34} J \cdot s \text{ x } 299792458\ m\ s^{-1} \text{ x } 1000\ mJ\ J^{-1}}{214\ nm \text{ x } 10^{-9}\ m\ nm^{-1}} \quad (2.5)$$

where a factor of 10^{-9} in the denominator is used to convert nm to m and a factor of 1000 in the denominator is used to convert J to mJ. Now that $E_{h\nu}$ has been calculated for a λ = 214 nm, the photon density ρ can be calculated. Using equation 2.3,

$$\rho = 1.10 \text{ x } 10^{15}\ photon\ pulse^{-1} = \frac{1\ mJ}{9.28 \text{ x } 10^{-16}\ mJ\ photon^{-1}} \quad (2.6)$$

where the resulting ρ can then be used in Equation 2.1. The next step is to determine the Gaussian beam width and subsequently the area of the laser beam using the calculated Gaussian beam radius. By using Equation 2.2 where,

$$0.00341cm = \frac{4 \cdot 214\ nm}{\pi\ 1 \times 10^{7}} \frac{250mm}{2 \cdot 1\ mm} \quad (2.7)$$

the Gaussian beam waist can be found. By assuming the beam is approximately a circle, the an approximate A_{spot}, 3.64 $\times 10^{-5}$ cm^2 can be determined. Using these calculated value in conjunction with Equation 2.1,

$$f_{frac} = 0.99 = 1 - e^{(-\frac{1.10 \text{ x } 10^{15}\ photon\ pulse^{-1} \text{ x } 2.20 \text{ x } 10^{-19}\ cm^2\ molecule^{-1}}{3.64\ \times\ 10^{-5}\ cm^2})}. \quad (2.8)$$

Once the dissociation percentage has been calculated and the viability of the experiment has been confirmed, an appropriate REMPI scheme must be chosen. The easiest place to start is by beginning with the simpler one-color experiment where the REMPI wavelength can also sufficiently

dissociate the target molecule.

2.2.2 REMPI

Resonance Enhanced Multiphoton Ionization is a versatile technique that allows for state-selective ionization and does not require VUV photons which are both hard to use and difficult to generate. When describing a REMPI scheme it is necessary to define the number of photons used and can be generally written in the following form, $n + m$ REMPI where the n refers to the number of photons to resonantly excite the fragment of interest from one electronic state to a higher electronic state and the m refers to the number of photons used to ionize the fragment from the higher electronic state. It is possible to have a variety of configurations such as 1+1, 2+1, and 1+1′ REMPI. The prime is indicates that the photon is not the same wavelength as the others. Theoretically there is no constraint on the number of photons and the number of different wavelengths that can be used in a REMPI scheme, however, since the absorption cross section is exponentially dependent on the number of photons used in each step, practically the fewer photons used, the more efficient the experiment will be. It is important to note that each additional photon in the resonance step increases the complexity of the image analysis described later. All of the experiments described in this dissertation utilized a 2+1 REMPI scheme. A figure of the 2+1 $E - X$ REMPI scheme for CO is shown below. [71, 72, 73]

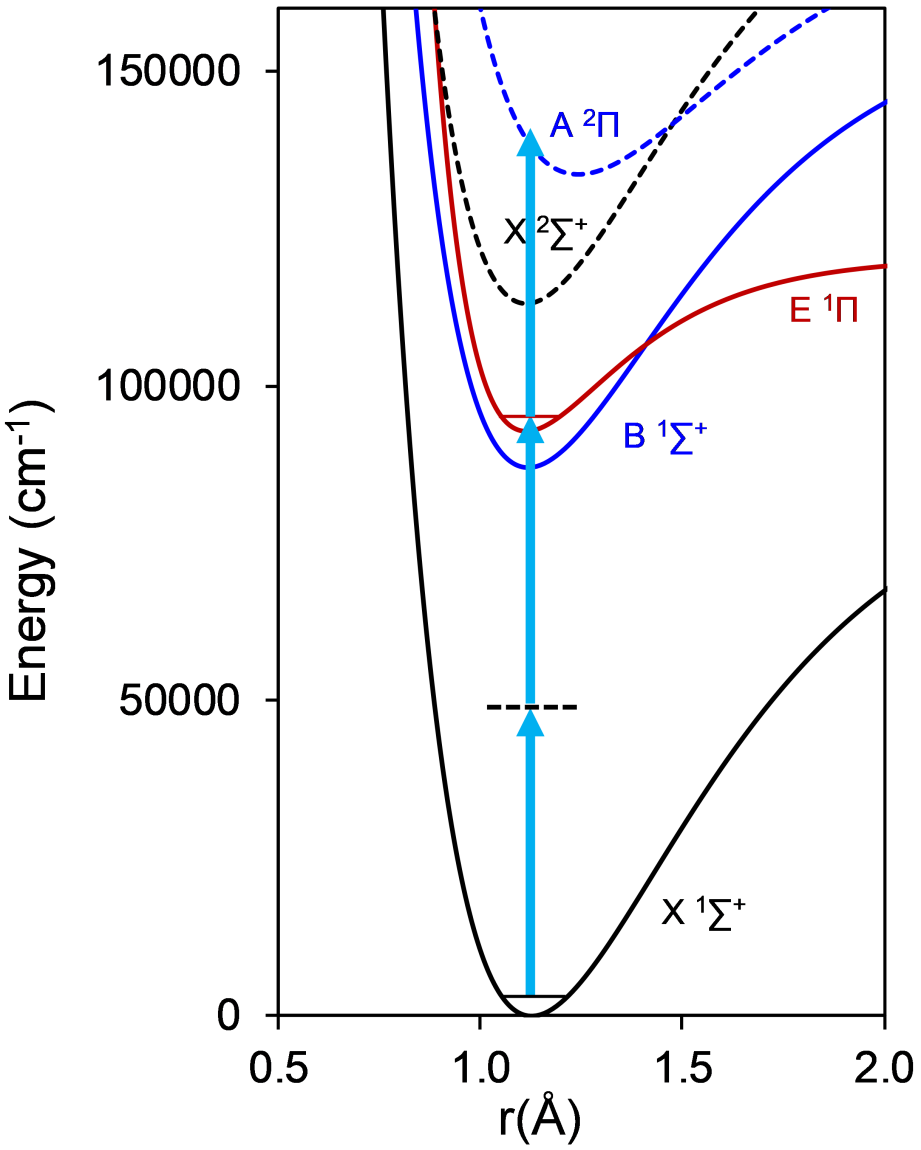

Figure 2.4: The 2+1 REMPI of CO ($E \leftarrow X$) transition where the $E(^1\Pi)$ state of CO is shown in red. The blue Morse potential represents the B($^1\Sigma^+$) state of CO. The dashed Morse potentials for the $CO^+(X^2\Sigma^+)$ and $CO^+(A^2\Pi)$ states are shown in black and blue respectively. Each blue arrow represents a ~214 nm photon and the horizontal dotted line represents the virtual state that the molecule transitions through as it absorbs each photon. The above potentials were calculated using the Morse potential energy equation.

In Figure 2.4 the CO potentials used in the OCS experiments are shown. The potentials were calculated using the Morse potential energy equation using the spectral constants listed in Table

1.1. Each individual blue arrow is representative of a single ~214 nm photon. The horizontal dotted line is representative of the virtual state that the CO molecule transitions through as it is resonantly excited by each photon. The virtual state in a REMPI process can be described as an intermediate state. These laser induced virtual states are related to the photon energy where its harmonics help drive the molecule into highly excited states. A virtual state does not have eigenstates and thus do not "acquire" populations during the excitation process.[74] All of the other REMPI schemes used herein can be similarly described.

	(CO)			(CO^+[IE = 113001.186 cm^{-1}])	
	$X^1\Sigma^+$	$B^1\Sigma^+$	$E^1\Pi$	$X^2\Sigma^+$	$A^2\Pi$
T_e (cm^{-1})	0	86945.2	92903	0*	20733.3*
D_e (cm^{-1})	8989.605	73316.245	27611.4	80845.59	45081.4375
ω_e (cm^{-1})	2169.81358	2112.7	2153.8	2214.2	1562
r_e (Å)	1.13	1.12	1.12	1.12	1.24

Table 2.1: Constants used to generate Morse potentials shown in Figure 2.4. The asterisk(*) indicates the values are in reference to the ground state of the CO^+ ion. These constants can be found on the NIST webbook for CO. The well depth, D_e were calculated using these constants.[20]

An example 2+1 REMPI spectrum and simulation is shown below in Figure 2.5. The REMPI was collected using room temperature CO, shown in black, and the corresponding simulation uses a Boltzmann distribution at 300 K for the rotational populations. In Figure 2.5 all five branches: S, R, Q, P, and O can be seen from left to right.

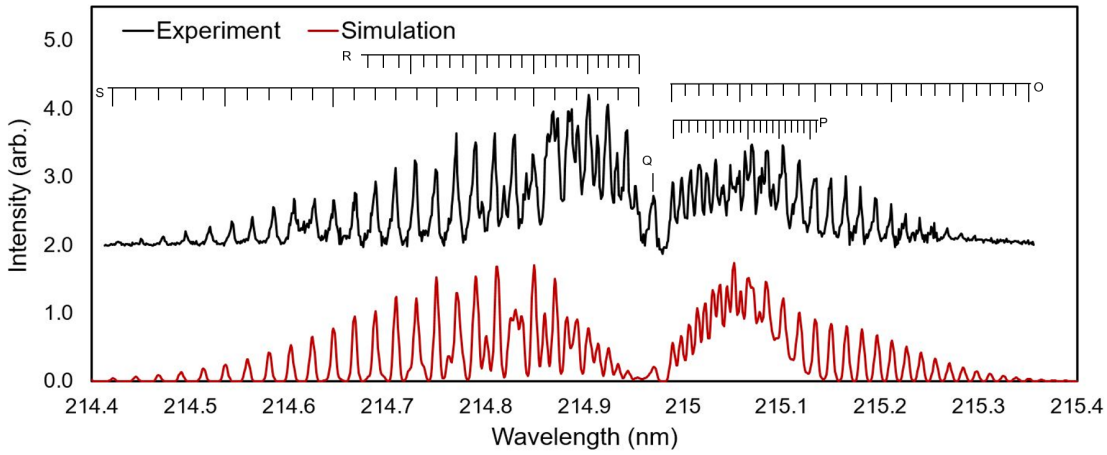

Figure 2.5: The 2+1 REMPI of CO $E - X$ transition using room temperature CO is shown in black and the corresponding simulation is shown in red where the populations use a Boltzmann distribution at 300 K.

2.3 Image Analysis

After tens of thousands of laser shots and photodissociation events, the accumulated ion signal is saved and recorded in a 768x768 dimensional U8 array. This two dimensional array is the ion image. The size and shape of the ion image contains detailed information about the energetics and dynamics of the photochemical reactions which occurred in the interaction region. In this section the data analysis method used to extract this information is described. This raw ion image can be analyzed in two distinct ways: first by analyzing the image intensity as a function of radius which contains information about how the energy is partitioned during the photodissociation process and second by analyzing the image intensity as a function of angle which contains information about the alignment and stereodynamics of the photodissociation process.

The first step in the image analysis process is to convert the ion image from I(x,y) to I(r,θ) by using equation 2.9 and 2.10,

$$r = \sqrt{(x - x_{center})^2 + (y - y_{center})^2} \tag{2.9}$$

$$\theta = \arctan \frac{x - x_{center}}{y - y_{center}} \tag{2.10}$$

where (x_{center}, y_{center}) are determined by hand. The ion images are fourfold symmetrized about the (x_{center}, y_{center}) in order to increase the signal-to-noise (S/N) of the image. By iteratively adjusting (x_{center}, y_{center}) until the reflections are perfectly overlapped, the (x_{center}, y_{center}) can be determined.[75] The end result is a higher S/N raw image known as a symmeterized image which can be analyzed in place of the raw image. The symmetrization procedure is shown, in one dimension, below in Figure 2.6.

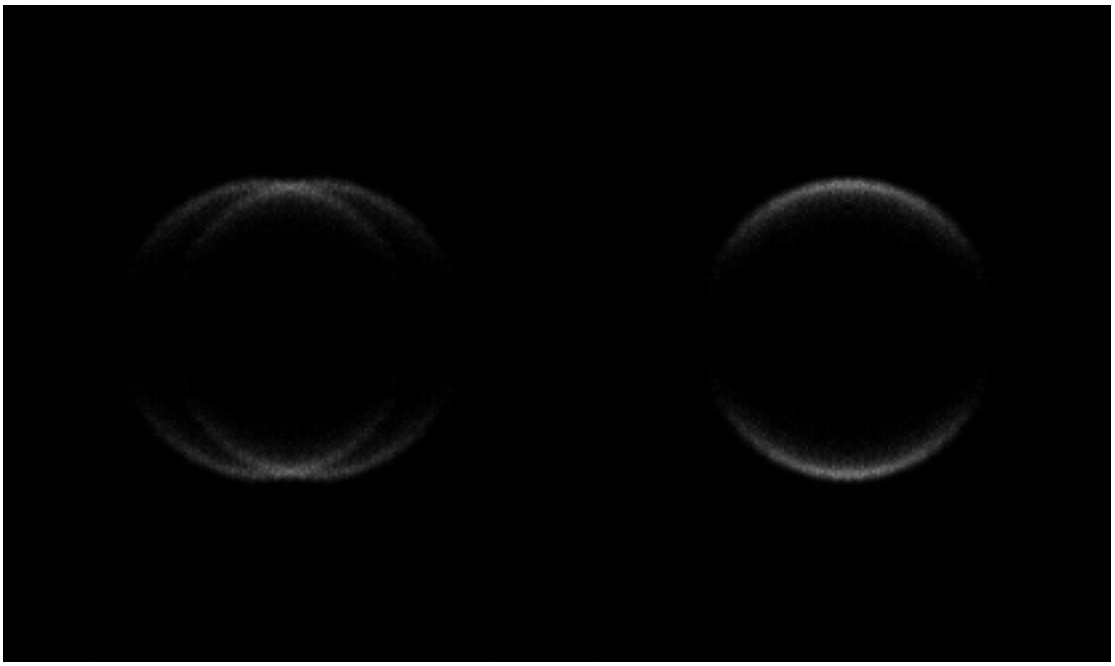

Figure 2.6: In the figure above both images are of CO($v = 0$, $j = 68$) resulting from the photodissociation of OCS at 230 nm. The image on the left is incorrectly symmeterized, where x_{center} is offset by 10 pixels. The image on the right is correctly symmeterized using experimentally determined x_{center} and y_{center}.

In Figure 2.6 above two versions of the same CO($v = 0$, $j = 68$) raw image originating from the photodissociation of OCS at 230 nm are shown. The image on the left is incorrectly symmeterized

where the x_{center} is offset by ten pixels. The image on the right hand side of Figure 2.6 has the correct x_{center} and y_{center}. The additional rings that are visible on the left hand image are offset reflections. Once the image has been symmeterized the analysis can take one of two paths. If the image is crushed then the image is first reconstructed. If the imaged is DC sliced, then the reconstruction process is not necessary since the image already correctly represents a center slice of the 3-D Newton sphere and thus passes on to the next stage of analysis.[67] When an image is crushed, the 3-D sphere is projected into a two dimensional plane. Since some of the ions will have a small amount of $\pm z$ velocity, the resulting crushed image contains these velocities which must be removed. The reconstruction process takes the 2-D crushed image and 'reconstructs' the 3-D newton sphere that was formed during the photodissociation process and a center slice of this reconstructed 3-D sphere is taken (which is equal to a sliced image). The reconstruction algorithm used in MiPANTS is called Polar Onion Peeling (POP).[76, 75] The algorithm is only valid if the image is cylindrically symmetric which only occurs when both the pump and probe lasers are polarized perpendicular to the detection axis.[2][76] In cases where other polarizations are used, it is no longer valid to use crushed imaging and it is then necessary to slice.[77]

2.3.1 Radial Distributions

Once the image has been appropriately process into a sliced image, either through DC slicing or reconstruction, the speed distribution can be extracted. The speed distribution of an image contains information about the energetics of the photochemical reaction. Practically a radial distribution of an image is the intensity of the image as a function of radius. An example speed distribution is shown in Figure 2.7.

[2]This geometry is the $\updownarrow\updownarrow$ configuration.

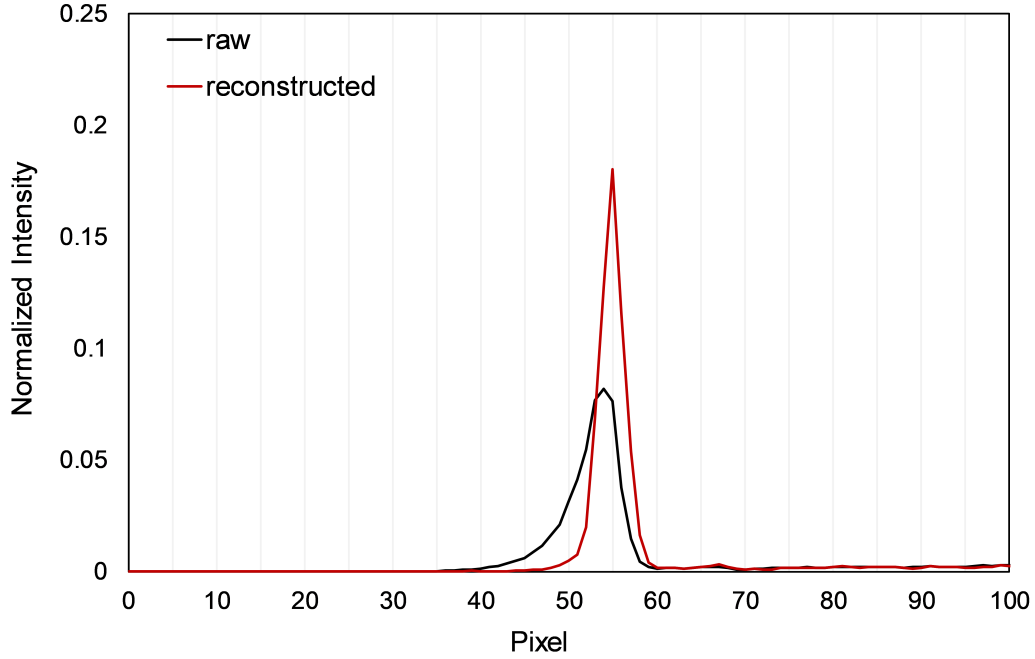

Figure 2.7: An example radial distribution for a raw 2-D crushed image and a 3-D reconstructed image are shown in black and red respectively. The long tail to lower speed, when comparing the raw to the reconstructed image, is an expected result and illustrates the necessity to reconstruct ion images. The radial distributions originate from the same image presented in Figure 2.6, CO(v = 0, j = 68) from the photodissociation of OCS at 230 nm.

In Figure 2.7 a radial distribution for both a raw (an image that is only symmeterized) and reconstructed image are shown black and red respectively. Here the effect reconstruction has on the quality of an image can be seen. The long tail of the raw speed distribution between 40 and 50 pixels is reduced depicting the removal of the $\pm z$ velocity captured in 2-D crushed image. This is a well known result and Figure 2.7 illustrates the necessity to reconstruct the raw image.

In order to make a quantitative determination of the correlated internal energy distributions of the photofragments it is necessary to first convert the x-axis from pixels to speed using a calibration curve. The first step is to calculate the expected speed for each possible quantum state that is energetically available. In Equation 2.11, using OCS as an example,

$$E_{avail} = h\nu_{diss.} - D_0(OC - S) + E_{int}(OCS) = E_{int}(CO) + E_{int}(S) + E_{trans} \tag{2.11}$$

$h\nu_{diss.}$ is the photon energy of the dissociation laser, $D_0(OCS)$ is the dissociation energy of OCS, $E_{int}(CO)$ is the internal energy partitioned into the CO fragment, $E_{int}(S)$ is the energy partitioned into the S fragment, $E_{int}(OCS)$ is any energy that was in the parent molecule prior to dissociation, and E_{trans} is the energy partitioned into translation. In order to convert the radius of our images in pixels to speed Equation 2.11 is used to connect E_{trans} to specific quantum states of CO. In the case of OCS several of the terms are well established: $h\nu_{diss.}$ is simply the energy of the dissociation laser, D_0 is a well established value in the literature, $E_{int}(S)$ is known as the dissociation of OCS results in $S\,^1(D)$ at near unity, and $E_{int}(OCS)$ is assumed to be zero due to the rapid cooling during the free jet expansion through the pulse valve. The assumption that $E_{int}(OCS)$ only applies to the rotational energy of the parent. If there are any vibrationally excited parent molecules, this vibrational energy remains a part of the parent OCS molecule and must be accounted for in Equation 2.11. From here it is necessary to calculate the expected velocity for each energetically possible quantum states of CO. This is done by calculating the j-dependent $E_{int}(CO)$ using the Equation 2.12,

$$E_{int}(CO) = Bj(j+1) - Dj^2(j+1)^2 \tag{2.12}$$

which is simply the rigid rotor approximation with the centrifugal distortion term included. The j-dependent $E_{int}(CO)$ is then used to calculate the E_{trans} using Equation 2.11 which is subsequently converted into speed following Equation 2.13 where,

$$v(j_{\mathrm{CO}}) = \sqrt{\frac{2E_{trans}}{\mu}} * \frac{m_S}{m_{OCS}} \tag{2.13}$$

where each $v(j_{\mathrm{CO}})$ corresponds to an individual j_{CO} state. Since the spacing between each j_{CO} state is spaced by approximately j^2, it is possible to collect a series of images to compare the measured pixel values against the calculated $v(j_{\mathrm{CO}})$ as seen in Figure 2.8. Once the speed to pixel has been determined, one can readily convert radial distributions into speed distributions for further analysis. With the energetics and expected speed now calculated, the speed-to-pixel

(StP) calibration is determined by collecting images with known speed distributions and making a calibration curve which can be seen below in Figure 2.8.

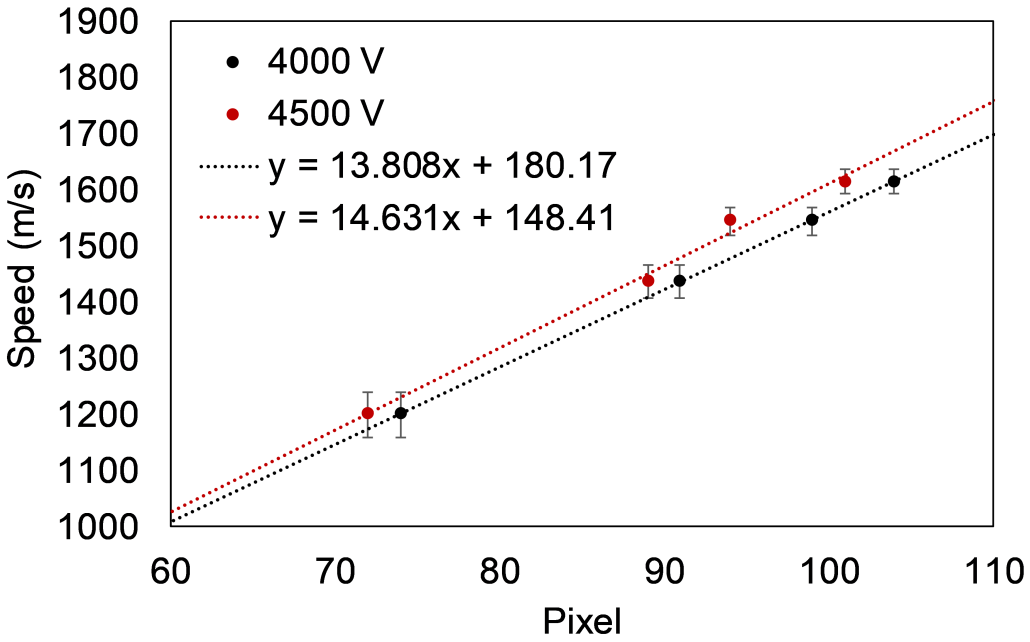

Figure 2.8: Two different speed-to-pixel calibration curves for repeller voltages of 4000 V and 4500 V shown as black and red respectively. The linear fit to each curve is shown where the slope is the conversion factor between pixels and speed. The error bars are representative of speeds equivalent to j±1

In the example StP calibration curve above there are two curves corresponding to two different V_r, 4000 V and 4500 V. The slope of each of the corresponding fits is 13.808 and 14.631 respectively. The slope of the linear fit allows one to readily convert from pixels to speed and speed to translational energy by following Equation 2.13.

2.3.2 Angular Distributions

In the previous section, the radial distribution connected the intensity of the of ion image as a function of radius to the energetics of the photodissociation reaction. In this section the focus will be on the angular distribution, which with careful analysis can provide a great deal of information

about the stereodynamics of the photochemical reactions. The angular distribution, I(r, θ), contains information about the forces and torques between the photofragments, the excited state symmetry of the parent molecule, as well as the timescale of photodissociation process.

When the molecular beam enters the main chamber, the molecules in the beam are randomly oriented with no preferential alignment and are randomly oriented. Since lasers are linearly polarized, when the dissociation laser interacts with the molecular beam, only molecules whose transition dipole moments are appropriately aligned with the electric field of the laser will be dissociated. This can be simply explained by Equation 2.14

$$P \propto |E \cdot \mu|^2 = ||E|| * ||\mu|| cos^2(\theta) \tag{2.14}$$

where the probability, P, of an electronic transition is dependent on overlap of the electric field vector, E, with the transition dipole moment μ. With each additional photon, another $cos^2(\theta)$ term must be added. For these experiments it is necessary to consider up to $cos^6(\theta)$ terms, one for the dissociation laser if it is vertically polzarized and one additional $cos^2(\theta)$ term for each of the n steps that are vertically polarized in the 2+1 REMPI scheme.[78, 30, 79]

Angular distributions are typically expressed as an expansion of Legendre polynomials where each $cos^n(\theta)$ term can be written in terms of β_n^{XY} coefficients of $P_n(cos(\theta))$. The image intensity as a function of angle can be described as

$$I(\theta) = 1 + \beta_2^{XY} P_2(cos\theta) + \beta_4^{XY} P_4(cos\theta) + \beta_6^{XY} P_6(cos\theta) \tag{2.15}$$

where X and Y describe the lab frame geometry of the pump and probe laser respectively. As Equation 2.15 indicates, the $I(\theta)$ is dependent on the orientation of the polarization of each laser. A vertical arrow (↕) indicate the laser is polarized along the image plane, which is referred to as "vertically polarization", while this symbol (⊙) indicates that the laser is polarized perpendicular to the plane of the image, which will be referred to as "horizontally polarization". For the remainder of this thesis both the pump and probe laser are vertically polarized unless otherwise noted. Any

one-color experiment described herein used a vertical-vertical geometry (↕↕). A vertical-vertical geometry has the added benefit of preserving the cylindrical symmetry allowing for these images to be reconstructed.[76, 80] Additionally it is possible to extract "sliced" angular distributions from raw images by taking a narrow pixel range (~7-10 pixels) of the outermost edge of the crushed image. A small pixel range of the outermost intensity of a raw image is equivalent to an angular distribution obtained from a experimentally sliced image.[77, 81]

2.3.3 Forward Convolution Fitting

In order to extract the vector properties from the angular distributions, a forward convolution method was chosen where trial angular distributions are generated and compared to the experimental data using the total χ^2 to determine the goodness of the fit. This method was chosen instead of a Direct Inversion method, where the bipolar moments are directly determined from the angular distributions, due to the difficulty associated with such a method. Typical imaging experiments measure a total of six different image anisotropy parameters, β_k^{XY}, while in a 2+1 REMPI experiment there are nine bipolar moments. This results in an underdetermined set. Additionally, the direct inversion method can result in unphysical results.[82] Rather than directly solve for the nine bipolar moments associated with a 2+1 REMPI image, a forward convolution method incorporating Dixon's five limiting cases is used to constrain the phase space to only physical results.

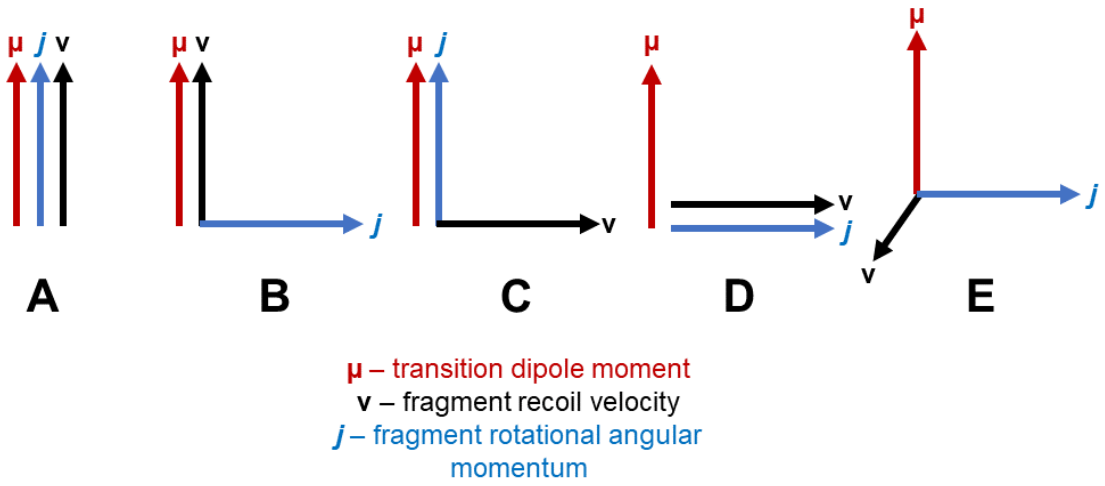

Figure 2.9: Dixon's five limiting cases which represent the five possible extreme orientations of the $\boldsymbol{\mu}$, **v**, and **j** vectors in photodissociation.[14]

Dixon's five limiting cases represent the five possible perpendicular or parallel orientations of the $\boldsymbol{\mu}$, **v**, and **j** vectors.[14] The values for the nine bipolar moments associated with each limiting case are shown in Table 1.2 A linear combination of these five cases used in conjunction with the 2+1 REMPI equations, described in detail in Ref. [82], can be used to calculate image anisotropy parameters, β_k^{XY} where k is the order. Angular distributions can then be calculated from these image anisotropy parameters following Equation 2.15 which are subsequently compared to the experimental data.

Table 2.2: Bipolar moments associated with Dixon's five limiting cases.[14, 30]

Bipolar Moments	Case A	Case B	Case C	Case D	Case E
$\beta_0^2(20) - \beta_{\mu\nu}$	1	1	-0.5	-0.5	-0.5
$\beta_0^2(02) - \beta_{\mu j}$	1	-0.5	1	-0.5	-0.5
$\beta_0^0(22) - \beta_{\nu j}$	1	-0.5	-0.5	1	-0.5
$\beta_0^2(22)$	-1	0.5	0.5	0.5	-1
$\beta_0^2(42)$	1	-0.5	0.375	-0.5	0.125
$\beta_0^0(44)$	1	0.375	0.375	1	0.375
$\beta_0^2(24)$	1	0.375	-0.5	-0.5	0.125
$\beta_0^2(44)$	-1	-0.375	-0.375	0.5	0.75
$\beta_0^2(64)$	1	0.375	-0.3125	-0.5	-0.0625

Based on Table 1.2, the $\beta_0^0(44)$ will range from 0.375 to 1 when using a linear combination of Dixon's five limiting cases to fit the angular distributions. This is problematic since the range of $\beta_0^0(44)$ actually spans from $-\frac{3}{7}$ to 1. In order to overcome this issue $\beta_0^0(44)$ parameter was used as an additional fitting parameter in conjunction with the five limiting cases. Generally, floating $\beta_0^0(44)$ resulted in better fits.[82, 32] This statement is validated in the following section. In practice the forward convolution method is done in one of two ways: the experimental data is fit manually by varying the limiting cases and $\beta_0^0(44)$ using chemical intuition in conjunction with χ^2 to achieve the best fits, or using Monte Carlo simulations to randomly determine the best possible fit using only χ^2 to determine the goodness of fit. The hand fitting procedure is inherently bias due to the expectations of the individual fitting the results. The Monte Carlo is used to remove the human element from the fitting procedure, but this method has its own drawbacks which are elaborated on in the next section.

2.3.4 Monte Carlo Simulations

Monte Carlo is a computational technique based on using random numbers to sample the parameter space of a distribution. In this case the Monte Carlo samples all possible orientations of the $\boldsymbol{\mu}$, $\mathbf{v}$, and $\mathbf{j}$ vectors by varying the ratio between the five limiting cases. The $\beta_0^0(44)$ bipolar moment is independently sampled over its possible range without consideration for the ratio of the five limiting cases. The randomly generated angular distributions are compared to the experimental angular distributions using χ^2 to determine whether the randomly generated angular distribution should be accepted or rejected. A schematic of the work flow beginning from image collection through the automated saving of the Monte Carlo results into excel is shown in Figure 2.10.

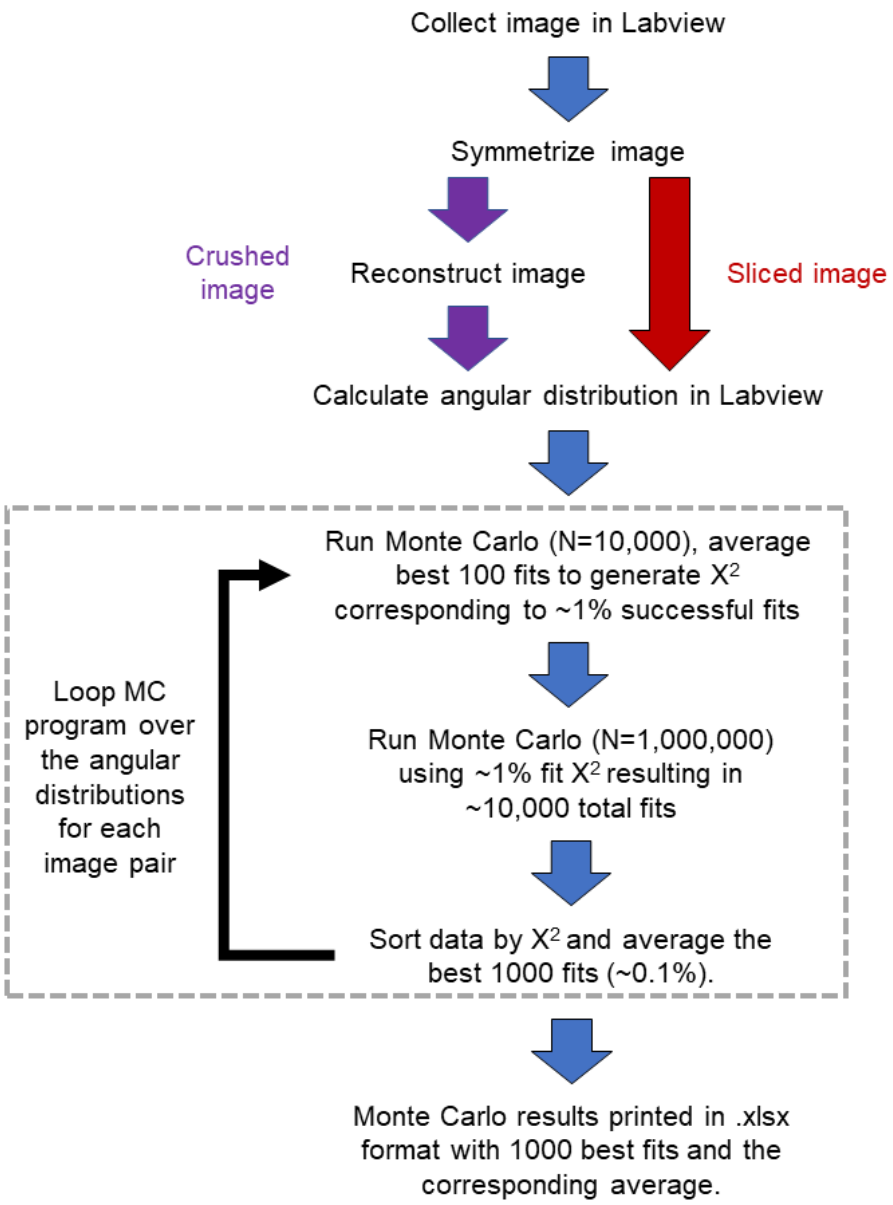

Figure 2.10: The work flow of the Monte Carlo forward convolution procedure beginning from image collection. Once the angular distributions have been calculated, the MC work flow is fully automated.

The Monte Carlo method used in this work has been continuously refined since its inception. The Monte Carlo simulations involving OCS results approximately follow the schematic shown in Figure 2.10. The early versions of the Monte Carlo fitting program required an initial guess χ^2

value which is inconsistent between data sets. The general goal was to run one million random samples with 100-200 accepted fits (~0.1 to 0.2%). In order to achieve this number of acceptable fits numerous test Monte Carlo simulations were run with a smaller number of samples, typically around ten thousand. Each test Monte Carlo simulation would slowly decrease the χ^2 value until ~0.01 to 0.02% of the ten thousand simulates were acceptable fits. Once the χ^2 was determined, the actual Monte Carlo simulation could then be conducted. In the OCS work presented in Section 3, the hand fit result was used as the data value while the standard deviation of the accepted fits were used as error bounds.

In the HN_3 experiments the number of Monte Carlo simulations needed was in the hundreds as opposed to the twenty to thirty Monte Carlo simulations run in the OCS experiments. The sheer number of Monte Carlo simulations motived the modification of the Monte Carlo program towards full automation. Due to the significant number of computations required by a Monte Carlo simulation it is important to consider the computer hardware. One million fits run on a laptop with an Intel i7-5500U CPU running 2.40 GHz with 8 GB of RAM running at 2400 mHz would take ~10 minutes while an AMD 1700x CPU running at 3.4 gHz with 16 GB of RAM running at 3200 mHz would take ≤4 minutes. In an effort to decrease the computation time required for the Monte Carlo simulations the χ^2 comparison function that was used inside the for loop was removed from the Monte Carlo calculation. Instead the best 1000 fits were selected from the one million trials by using a sorting function to order the one million trials by χ^2. This method was quite unsuccessful, increasing the computation time to ≥10 hours. While the computational time required for the for loop was reduced, the sorting function was found to be exponentially dependent on the number of rows that were needed to sort. The sorting function was nearly unusable at $N \geq 100000$. An alternative method was devised, shown in Figure 2.10, where a single trial Monte Carlo simulation is run with N=10000 with no limiting χ^2 value set. These ten thousand random angular distributions can be quickly sorted by the Labview sorting function. Once sorted the average χ^2 from the best one hundred fits is then used to limit the actual Monte Carlo to generate ~10000 total fits which are then sorted. The best one thousand angular distributions are

automatically saved in an excel file and are then averaged and plotted against the experimental angular distribution. The plotted image is saved as a bitmap to allow for easy review of each result. While the computational time of every one million simulations was not reduced, the reduction in time between the runs of each Monte Carlo simulation greatly accelerated the simulation process.

A set of synthetic data (data set 1 in Table **??**) was fit using $\beta_0^0(44)$ generated from the linear combination of the five limiting cases and was fit floating $\beta_0^0(44)$ in order to test the effect of floating the $\beta_0^0(44)$ parameter on the three lower order bipolar moments. The resulting best 1000 fits can be seen in Figure 2.11.

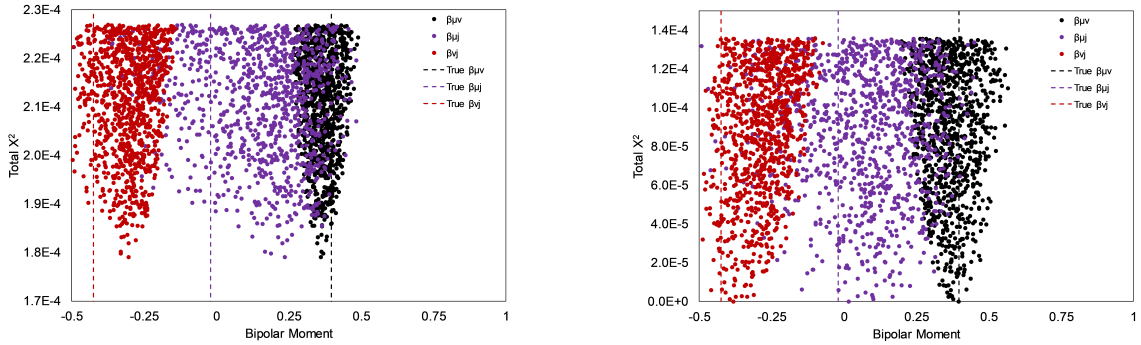

Figure 2.11: (a)The results of fits to a synthetic data set using $\beta_0^0(44)$ generated from the linear combination of the five limiting cases. (b) The results of fits to a synthetic data set floating $\beta_0^0(44)$. The three lower order moments are plotted as a function of χ^2 where the vertical lines represent the true value of each moment.

The $\beta_{\mu\nu}$, $\beta_{\mu j}$, and $\beta_{\nu j}$ have very similar features in Figure 2.11a and Figure 1.3 where each bipolar moment is generally centered on the true value. The $\beta_{\mu\nu}$ and $\beta_{\nu j}$ distributions have tighter distributions which is an expected result due to the coefficients in the 2+1 equations.[82] It is important to note that the overall χ^2 is much lower for the floated $\beta_0^0(44)$ fits than the limiting cases $\beta_0^0(44)$ fits. This indicates that the worst fit from the floated $\beta_0^0(44)$ is better than the best fit originating from the limiting cases $\beta_0^0(44)$ fits. Despite these differences, the deviation from the average of the best 1000 fits both the limiting cases $\beta_0^0(44)$ results and the floated $\beta_0^0(44)$ results from the true values are very similar. The example shown above was the best limiting cases result

for the three synthetic data sets tested. In the other two data sets, the floating values preformed better for each of the three lower bipolar moments. Floating $\beta_0^0(44)$ typically results in better overall fits which have lower total χ^2 when compared to the limiting case $\beta_0^0(44)$ fits. The average of the best 1000 fits for each of the three tests can be found in Table 1.3.

Table 2.3: Comparing the results from the best 1000 best fits to a synthetic data set using $\beta_0^0(44)$ generated from the linear combination of the five limiting cases and independently floating $\beta_0^0(44)$.

Bipolar Moments	Data Set	True Value	5 Limiting Cases	Float $\beta_0^0(44)$
$\beta_0^2(20)$ - $\beta_{\mu v}$	1	0.3975	0.364	0.364
$\beta_0^2(02)$ - $\beta_{\mu j}$	1	-0.0205	0.151	0.069
$\beta_0^0(22)$ - $\beta_{v j}$	1	-0.426	-0.302	-0.283
$\beta_0^2(20)$ - $\beta_{\mu v}$	2	0.35	0.246	0.293
$\beta_0^2(02)$ - $\beta_{\mu j}$	2	-0.15	-0.376	0.110
$\beta_0^0(22)$ - $\beta_{v j}$	2	-0.5	-0.38	-0.298
$\beta_0^2(20)$ - $\beta_{\mu v}$	3	0.1	0.146	0.099
$\beta_0^2(02)$ - $\beta_{\mu j}$	3	0.1	0.344	0.228
$\beta_0^0(22)$ - $\beta_{v j}$	3	0.1	0.223	0.010

2.4 Experimental Conditions for OCS, Acetaldehyde, Ketene, and Hydrazoic Acid

In this section the preparation of each analyte, the experimental conditions of both the pump and probe lasers, as well as any other necessary experimental modifications will be described. Each individual experiment had unique experimental challenges that needed to be overcome. Which will be discussed in the next several sections.

2.4.1 OCS

Carbonyl Sulfide (OCS) is a gas at room temperature with a boiling point of -50.2 °C. In a typical experiment, only a small fraction of analyte is entrained into a helium flow. A simple

way to regulate the percent of analyte in the flow is to manipulate the vapor pressure of a liquid by changing the temperature. In the case of OCS(Sigma Aldrich ≥ 97.5% purity), it is trapped in a glass bubbler in a Acetone/Dry Ice bath at -78 °C. By referencing Figure 2.12, seen below, it is possible to determine the fraction of OCS in the flow using a dry ice/acetone bath (-78 °C) marked as an open circle on both the vapor pressure curve and the fraction of OCS curve, shown in black and red respectively. At the temperature of -78 °C the percentage of OCS in the sample is approximately 17.5%.[15]

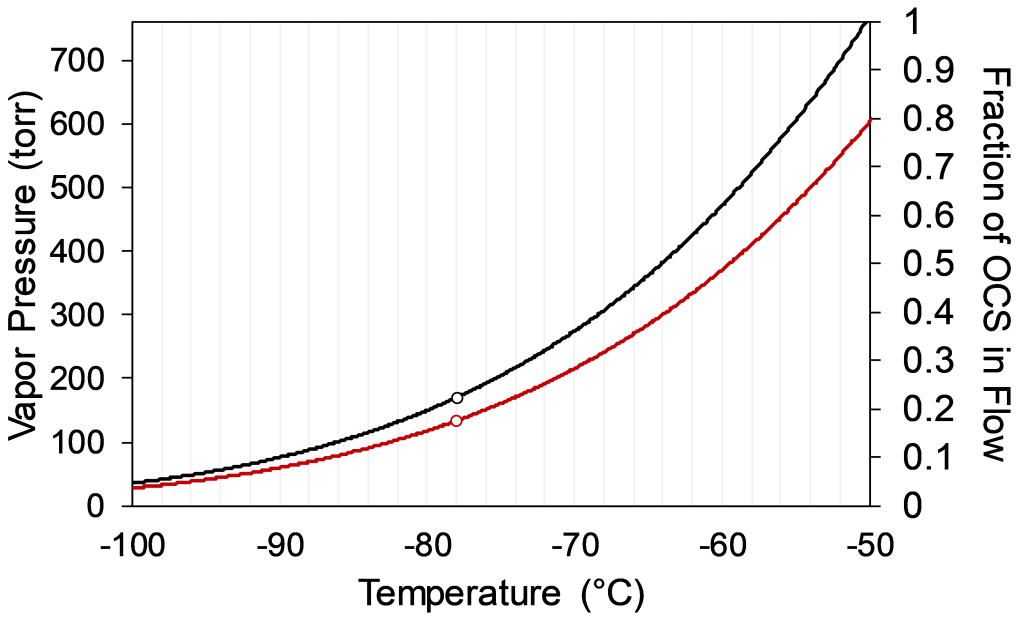

Figure 2.12: The vapor pressure of OCS, in atmospheres, as a function of temperature shown in black and the fractional percentage of OCS entrained in the flow with the He regulator set at ~0.25 atm which corresponds to a total pressure of ~1.25 atm in He. The open circles on each curve refer to the temperature of a dry ice/acetone bath (-78 °C).[15]

Once the concentration of OCS has been set by adjusting the temperature of the sample, the OCS is entrained into the helium flow into the chamber through the pulse valve. The OCS/He flow is then pulsed into the chamber undergoing a free jet expansion which rapidly cools the OCS parent molecules to a average rotational temperature near 10 K.[22] After the rapid cooling, the

OCS molecules enter the main chamber through a electroform skimmer collimating the molecular beam. Once the flow enters the main chamber it is first dissociated and then ionized via a 2+1 REMPI scheme. The majority of the OCS experiments were conducted at 214 nm while a small fraction of the experiments were conducted at 230 nm. All of the OCS experiments where the CO fragment was investigated were one-color experiments. The few OCS experiments where the S($^1D_2$) fragment was probed were two-color experiments which utilized a vertical horizontal geometry.

The ~214 nm light initially used a Stilbene 420/methanol dye mix. Typical powers for this dye mixture were ~ 15 mJ/pulse of average dye power and 0.5 μj of average doubled power when seeded with ~200 mJ/pulse of 355 nm light. Stilbene was a very difficult dye to work with due to the very short working lifetime of the dye of ~2 hours. The short lifetime resulted in a constant power decay which required the dye to be refreshed 3-4 times during a single experiment. Due to these difficulties the dye mixture was changed to Exalite 428/1,4-Dioxane. Typical powers for this dye mixture were ~20 mJ/pulse of average dye power and 1.5 mJ/pulse of average doubled power when seeded with ~300 mJ/pulse of 355 nm light. The increase in the power of the 355 nm light was the result of replacing the a Spectra-Physics Lab 150-10 Nd:YAG with a Spectra-Physics Pro 230-10 Nd:YAG. The Exalite 428 dye blend would last more than a month with minimal effects on the power which in turn resulted in incredible increases to the stability of the dye output compared to the Stilbene 420 dye.

In Figure 2.13 the absorption cross section as a function of wavelength is shown where the filled red triangles mark the absorption cross section at 214 nm and 230 nm.[16] Practically, acceptable signal required a minimum of ~0.5 mJ/pulse and ~0.1 mJ/pulse was needed at each wavelength respectively. A typical experiment with excellent S/N used ~1.5 mJ/pulse and ~0.5 mJ/pulse of average laser power respectively.

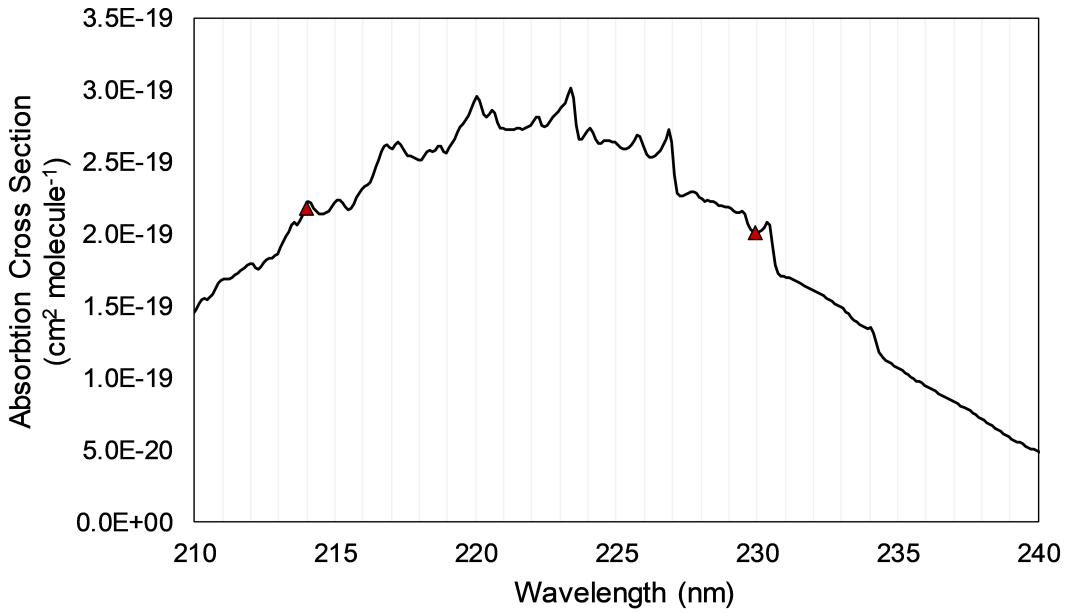

Figure 2.13: The absorption cross section of OCS at 177 K, as a function of wavelength. Each of the red triangles, at 214 nm and 230 nm, refers to a wavelength that used to dissociate OCS.[16]

In the case of OCS a 2+1 REMPI scheme was employed through two different excited states of CO, the $E(^1\Pi) - X(^1\Sigma^+)$ and $B(^1\Sigma^+) - X(^1\Sigma^+)$ transitions, and one S($^1D_2$) excited state via a $^3P_1$ intermediate state at 291.18 nm.[71, 72, 83, 84, 73] Shown below in Table 1.4 are the spectral constants used to fit the REMPI spectra. Once the fragment has been resonantly ionized it is velocity focused downfield by the ion optics onto the MCP/phosphor screen assembly where it is collected by the u-EYE CCD camera and recorded using Labview for analysis.

	CO		
	$X^1\Sigma^+$	$B^1\Sigma^+$	$E^1\Pi$
T_e (cm^{-1})	0	86945.2	92903
ω_e (cm^{-1})	2169.813	2112.7	2153.8
$\omega_e\chi_e$ (cm^{-1})	13.28832	15.22	42
B_e (cm^{-1})	1.93128	1.9612	1.9771
D_e (10^{-6} cm^{-1})	6.1214	7.1	6.5

Table 2.4: Shown above are the spectral constants used to fit the various CO REMPI spectra.[20]

2.4.2 Hydrazoic Acid (HN_3)

In this section the experimental conditions for HN_3 are discussed in detail beginning with the synthesis of HN_3 gas to the experimental REMPI schemes used to ionize the HN radical fragments. Hydrazoic acid (HN_3), also known as hydrogen azide, is a colorless, volatile, and explosive liquid at room temperature and pressure. Due to the volatile and explosive nature of HN_3 it is necessary to keep the HN_3 diluted. In these experiments HN_3 is kept at a concentration of ~10% in helium.

First the hydrazoic acid must be synthesized following Equation 2.16,

$$NaN_3 + StearicAcid(C_{17}H_{35}CO_2H) \rightarrow HN_3 + Sodium\ Stearate(NaC_{17}H_{35}CO_2) \tag{2.16}$$

where the stearic acid is in excess. Practically sodium azide is added a vacuum Erlenmeyer flask at a 1:7.5 ratio to the stearic acid by mass. The mixture is heated to a temperature of ~95°C where the stearic acid melts into a viscous solution. The flask is under vacuum during the heating process removing any ambient air from the head space of the flask. After several minutes small bubbles will begin to appear in the solution and the vacuum is removed and the HN_3 gas is collected in a glass bulb. The pressure of the system is measured by a baratron and once the pressure of the glass bulb reaches ~50 torr the reaction is halted. The bulb is then filled to ~500 torr with pure helium resulting in a ~10% mixture of HN_3 helium gas. UV-vis spectroscopy is used to confirm the formation of the HN_3 in the reaction vessel. A picture of the reaction setup can be seen in Figure 2.14.

Figure 2.14: A picture of the HN_3 synthesis setup.

In Figure 2.15 the absorption cross section as a function of wavelength is shown where the filled red triangles at 256 nm, 271 nm, and 285 nm mark the three dissociation wavelengths used in the HN_3 experiments. The dye and dye concentrations used at 256 nm, 271 nm and 285 nm were Coumarin 500 (1.6×10^{-3} M), Rhodamine 6G (1×10^{-4} M), and Coumarin 540a (1×10^{-3} M) which resulted in average powers of 2 mJ/pulse, 1 mJ/pulse, and 1.8 mJ/pulse respectively. In the case of the Rhodamine 590, a different laser system was used. A Lab 150-10 Spectra-Physics Nd:YAG coupled with an LAS dye laser was used to do both the scanning and image collection. Here it is important to note the importance of manipulating the dye concentration in order to achieve the best possible efficiency from the dye laser. When reference the recommended dye concentration from both Sirah and Exciton for Rhodamine 6G, the recommended dye concentrations were ~3-4 times more concentrated than the concentration used for the experiments. The difference in the doubled

output power was staggering increasing from ~0.1 mJ/pulse to ~1 mJ/pulse of average power. The minimum power to see signal at all three wavelengths was ~0.5 mJ/pulse.

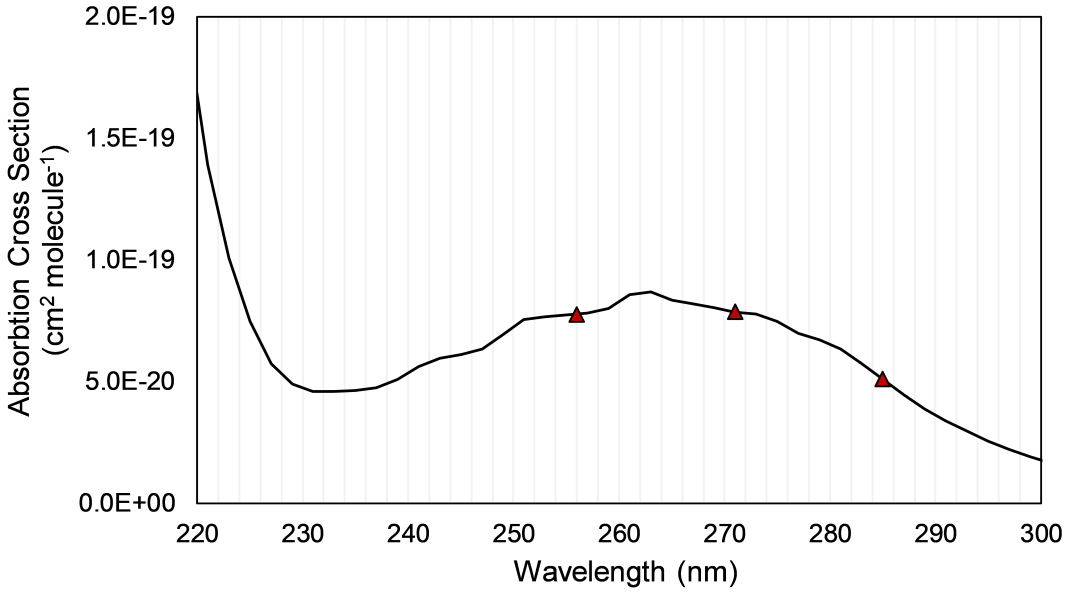

Figure 2.15: The absorption cross section of HN_3 at 298 K, as a function of wavelength. Each of the red triangles, at 256 nm, 271 nm and 285 nm, refers to a wavelength that used to dissociate HN_3.

Each of the dissociated wavelengths used in the HN_3 experiments were also the REMPI wavelengths as each experiment was 1-color. A 2+1 REMPI scheme was for the HN fragment was used for each of the three wavelengths where a ($g^1\Delta \leftarrow a^1\Delta$) transition, a ($f^1\Pi \leftarrow a^1\Delta$) transition, and a ($d^1\Sigma^+ \leftarrow a^1\Delta$) transition were used at 256 nm, 271 nm, and 285 nm respectively. These REMPI transitions can be seen in Figure 2.16. The corresponding constants used to calculate the Morse potentials can also be seen below in Table 1.5.[17, 18, 19]

The three excited electronic states of HN_3 that were used in the HN_3 experiments are shown in Figure 2.16 below.[17, 18, 19, 20]

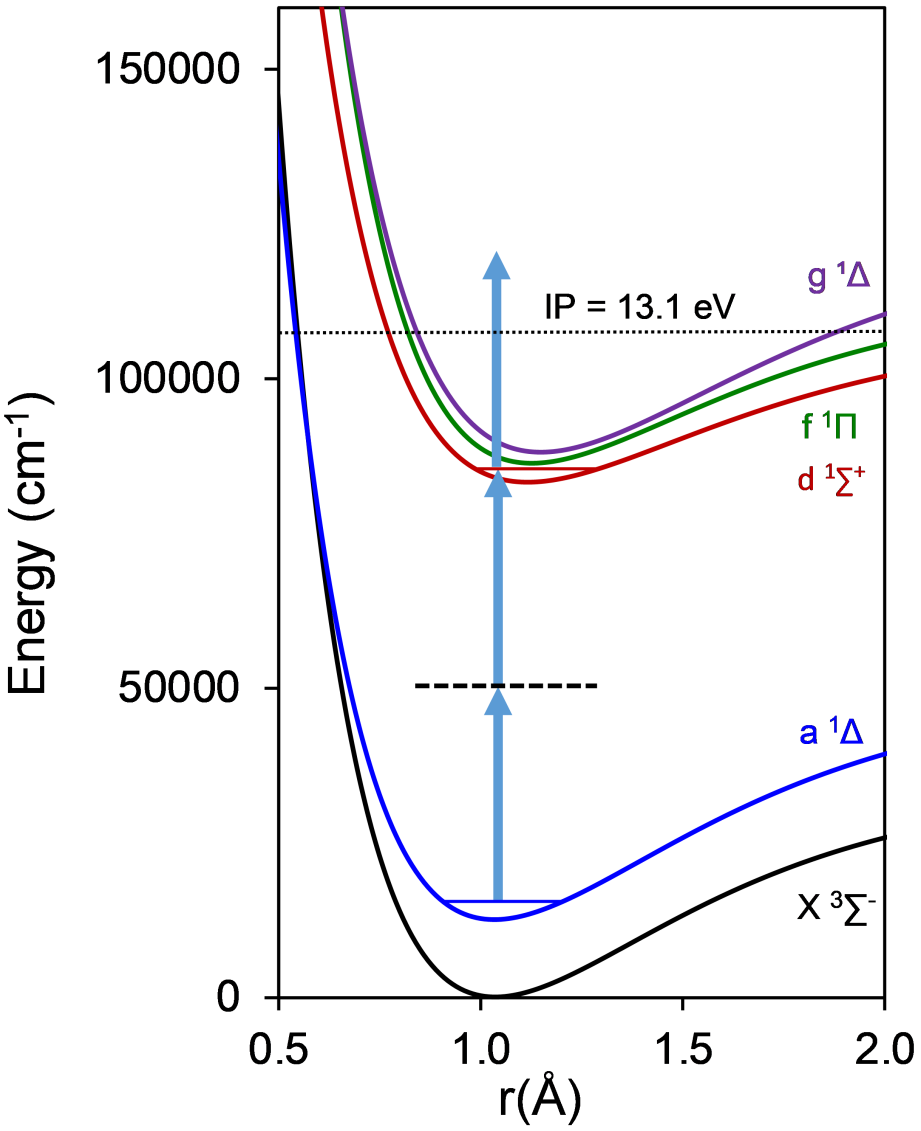

Figure 2.16: The 2+1 REMPI of HN ($d \leftarrow a$) transition where the $d(^1\Sigma^+)$ state of HN is shown in red. The blue Morse potential represents the HN($a^1\Delta$) state of HN where all of the HN is probed from. The green Morse potential represents the HN($f^1\Pi$) excited state. The purple Morse potential represents the HN($g^1\Delta$) state. Each blue arrow represents a ~285 nm photon and the horizontal dotted line represents the virtual state that the molecule transitions through as it absorbs each photon. The above potentials were calculated using the Morse potential energy equation.[17, 18, 19, 20]

Each of the HN potentials were calculated using the Morse potential energy equation using the spectral constants listed in Table 1.6.

	HN				
	$X^3\Sigma^-$	$a^1\Delta$	$d^1\Sigma^+$	$f^1\Pi$	$g^1\Pi$
T_e (cm^{-1})	0	12566	83160	86378	88140
D_e (cm^{-1})	34379.525	37365	25974.9	27650	36550
ω_e (cm^{-1})	3282.2	3188	2672.6	2903	2903
r_e (Å)	1.04	1.03	1.12	1.13	1.15

Table 2.5: Constants used to generate Morse potentials shown in Figure 2.16. In this instance the well depths, D_e, were taken from Ref. [31].[17, 18, 19, 31, 20]

Some attempts were made to perform 2-color experiments using 266 nm output from a Nd:YAG laser and the 256 nm ($g^1\Delta \leftarrow a^1\Delta$) REMPI transition, but due to the intensity of the 1-color signal and similar image shapes, the two color signal was too difficult to distinguish from the 1-color signal. The HN ions resulting from the 2+1 REMPI process are then velocity focused downfield by the ion optics and are detected by the MCP/phosphor screen assembly where the resulting phosphorescence is collect by the u-EYE CCD camera and recorded using Labview for analysis. The constants used to fit the HN REMPI spectra are shown below in Table 1.6.

	HN			
	$a^1\Delta$	$d^1\Sigma^+$	$f^1\Pi$	$g^1\Delta$
T_e (cm^{-1})	12566	83160	86378	88140
ω_e (cm^{-1})	3188	2672.6	N/A	2462.0*
$\omega_e\chi_e$ (cm^{-1})	68	71.2	N/A	N/A
B_e (cm^{-1})	16.44	14.39	14.23	14.09
D_e (10^{-3} cm^{-1})	1.62	1.6	1.63	1.68

Table 2.6: Shown above are the spectral constants used to fit the various HN REMPI spectra.[20] An asterisk represents the vibrational term value $G(v)$.

3. EMPIRICAL ASSIGNMENT OF ABSORBING ELECTRONIC STATE CONTRIBUTIONS TO OCS PHOTODISSOCIATION PRODUCT STATE POPULATIONS FROM 214 TO 248 NM.[1,2]

In this section the photodissociation dynamics of OCS near 214 nm for the S($^1D_2$) channel using VELMI are presented. The initial experimental and theoretical work, lead by Dr. Wei (Ref. [22]), has been extended at this wavelength. The work present here focuses on the vector and scalar correlations in the CO($v = 1$) products. The initial CO($v = 0$) results are reanalyzed and extended to determine the roles of each electronic state in the dissociation dynamics at this wavelength. Experimentally determined spatial anisotropy and alignment parameters, extracted from a series of sliced CO($v = 1$) ion images, were employed to identify the electronic state origins of each rotational state in the CO($v = 1$) channel. Following this analysis, the rotational distribution was decomposed into CO products originating from two states, the 2^1A′(A) state and 1^1A″(B) state of OCS. The fractional contribution from the 1^1A″(B) state, f_B, was experimentally determined to be $\sim$ 2.5 times smaller ($f_B = 0.14 \pm 0.04$) than previous theoretical estimates. This analysis method was also extended to the CO($v = 0$) channel. The spatial anisotropy and alignment parameters for the CO($v = 0$) channel were determined from a series of sliced CO($v = 0$) ion images across the reanalyzed CO($v = 0$) rotational distribution. The 1^1A″(B) state contribution was determined to be $\sim$ 1.7 times smaller ($f_B = 0.20 \pm 0.04$) than previously reported. In an effort to better understand the first absorption band of OCS this analysis was method was applied to the experimental rotational distributions at photolysis wavelengths of 223 nm, 230 nm, and 248 nm presented in the literature. The fractional contribution of the B state of OCS (f_B) at each wavelength was then compared to the theoretical f_B across the first absorption band of OCS.

[1]Reprinted with permission from Empirical assignment of absorbing electronic state contributions to OCS photodissociation product state populations from 214 nm to 248 nm by C.J. Wallace; G.E. Gunthardt; G.C. McBane; S. W. North, 2019. Chemical Physics, 520, 1, Copyright [2019] by Elsevier

[2]Reprinted with permission from Anomalous Intensities in the 2+1 REMPI Spectrum of the $E^1\Pi - X^1\Sigma$ Transition of CO by C.E. Gunthardt; C.J. Wallace; G.E. Hall; R.W. Field; S.W. North 2019. Journal of Physical Chemistry A, 123 , 2780, Copyright [2019] by American Chemical Society

3.1 Experiment

3.1.1 Experimental Methods

The velocity-map ion imaging experiment has been previously described in detail in Section 2.4.1, but a short summary will be provided here. Helium at 1 atm is flowed over OCS maintained at 196 K in a bubbler resulting in ~25% seeded OCS. The OCS/helium mixture undergoes a free jet expansion through a pulsed valve into the source region, rapidly cooling the OCS to $\sim$ 10 K. The molecular beam is then collimated by a skimmer and crossed at 90 degrees by a linearly polarized 214 nm laser beam ($\sim$ 1.5 mJ/pulse). The 214 nm light is used to both photodissociate the OCS and resonantly ionize the CO products via a 2+1 REMPI scheme through the E state of CO.[72] The resulting ions are then accelerated and velocity mapped onto a position-sensitive microchannel plate detector (MCP) with a P51 phosphor screen. The MCP timing was gated for a 40 ns slice which accounted for approximately $\sim$ 20% of the final image width. A Hamamatsu R928 photomultiplier tube or IDS uEye gated CCD camera was used to record the signal from the phosphor screen. The angular distributions from the sliced images were analyzed using the forward convolution method described in detail in Wei *et al.* [82]

3.1.2 Calculations

Some classical trajectory and surface hopping results obtained as part of the work described in reference [22] are reported here for the first time. In these calculations, trajectories were started on the empirically modified A and B state surfaces of reference [2] with total angular momentum zero and distributions of positions and momenta selected to model the ground vibrational state of OCS. The total energy was the sum of the photon energy and the zero point vibrational energy of OCS (0.245 eV), reduced by 0.1 eV to alleviate unphysical leaking of CO zero-point vibrational energy into product rotation. Nonadiabatic coupling from the A to the X surface was modeled using the method of Tully [85], using only the γ component of the nonadiabatic coupling. Final state distributions and angular distributions were constructed from the trajectories using weights proportional to the squares of the OCS ground state vibrational wavefunction and the transition

dipole moment at the starting geometry. The "calculated" fractional contributions of the B state to the absorption at each wavelength come from Figure 2b of McBane *et al.* [2], with values at a few specific wavelengths computed separately from the corresponding wavepacket calculations. [86]

3.2 Results and Discussion

3.2.1 CO(v = 1) product internal state distributions and vector correlations

The experimental CO(v = 1) rotational distribution arising from a 2+1 E-X REMPI scan from the photodissociation of OCS near 214 nm is shown in the two panels of Figure 3.3. The corresponding REMPI spetrum is show in Figure 3.1.

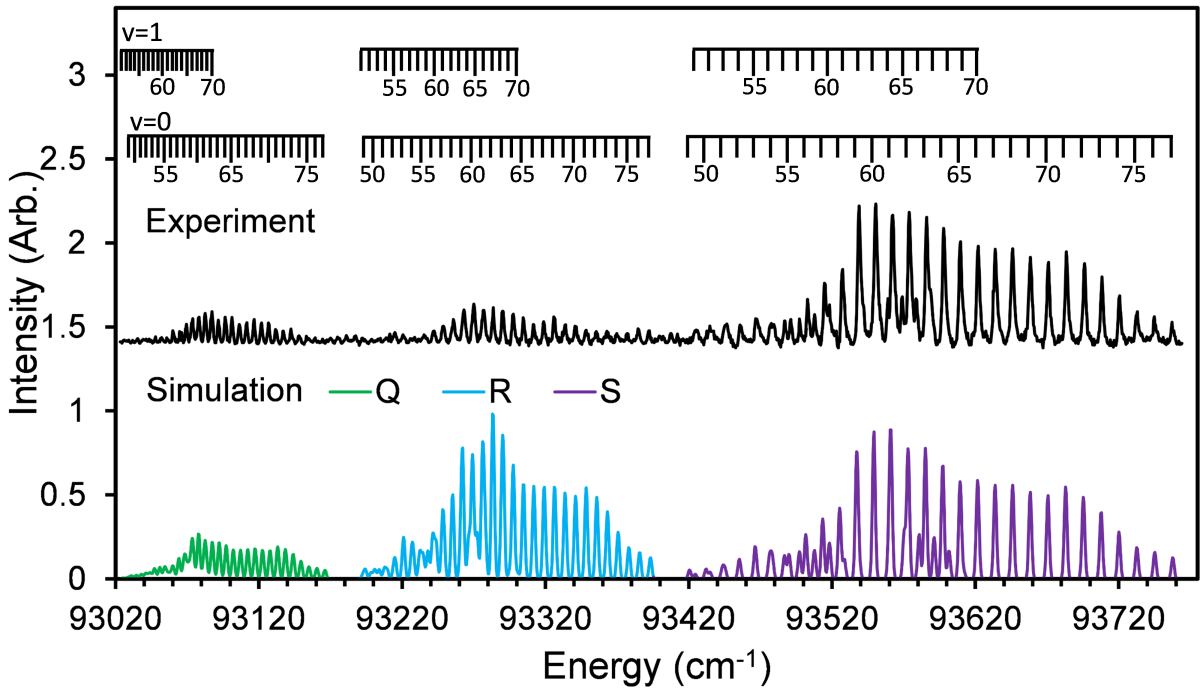

Figure 3.1: 2+1 REMPI spectrum adapted from reference [21].[2]

In a one-color experiment the photodissociation wavelength necessarily changes across the region of the 2+1 REMPI spectrum. However, previous experiments have demonstrated that

there are minimal changes to the rotational distribution due to changes in the photodissociation wavelength.[22] One-color measurements can therefore be used to measure CO rotational populations over the scanned region. Wei *et al.* [22] presented $v = 1$ rotational distributions constructed from 2+1 REMPI S branch data. Here, we add data from R and Q branches to the analysis, and present the resulting distribution in Figure 3.3, where the error bars indicate the standard deviations of population obtained from the three branches. The individual populations used to determine the average CO($v = 1$) in Figure 3.3 can be seen below in Figure 3.2.

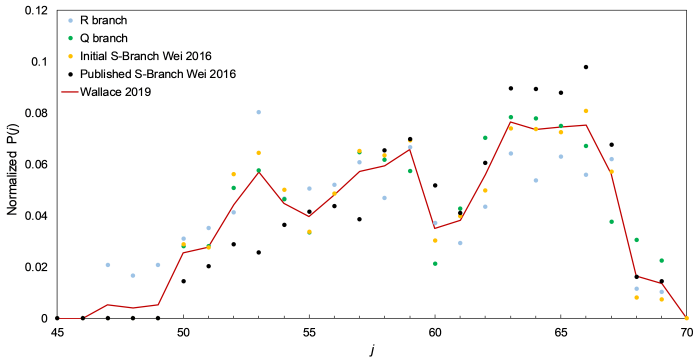

Figure 3.2: CO($v = 1$) rotational distribution for the S, R, and Q branches are shown above where the average of the four different distributions, used in Figure 3.3, is shown as the red line.[22, 3]

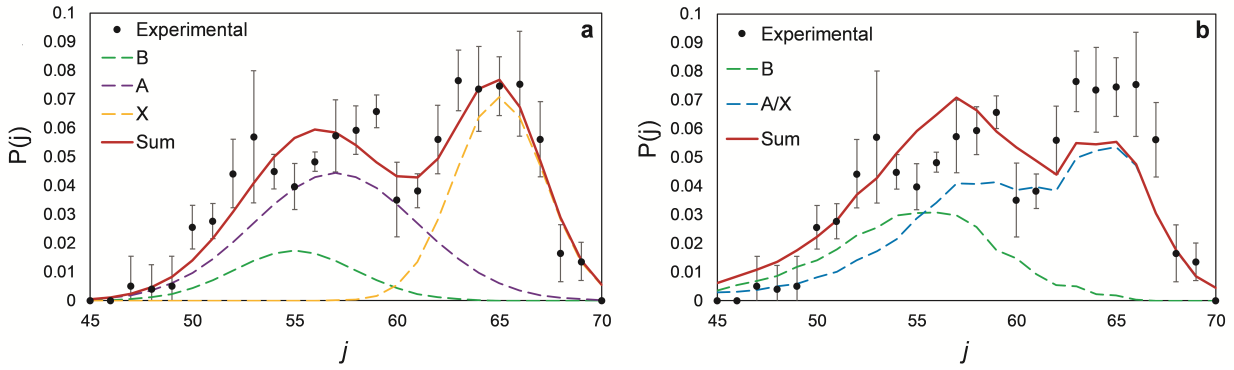

Figure 3.3: CO(v = 1) rotational distribution shown as filled circles. The contribution from the A state is shown as the purple dashed line, the contribution from the B state is shown in green dashed line, and the contribution from the X state is shown as the yellow dashed line. The contribution from the A/X trajectories is shown in blue. The sum is shown as the solid red line. (a) Fits to the experimental data employing three adjustable Gaussians. (b) Results from classical trajectory calculations previously published by Wei *et al.* .[22]

To first order, the presence of a Q branch is unexpected, as the two photon Q branch line strengths for a Π-Σ transition are negligible in the high j regime.[87] The assignment of the Q branch is unambiguous as the observed peak positions agree with calculated Q branch transitions and the j_{CO} assignments have been confirmed using fragment translational energy distributions obtained from a series of Q branch images.

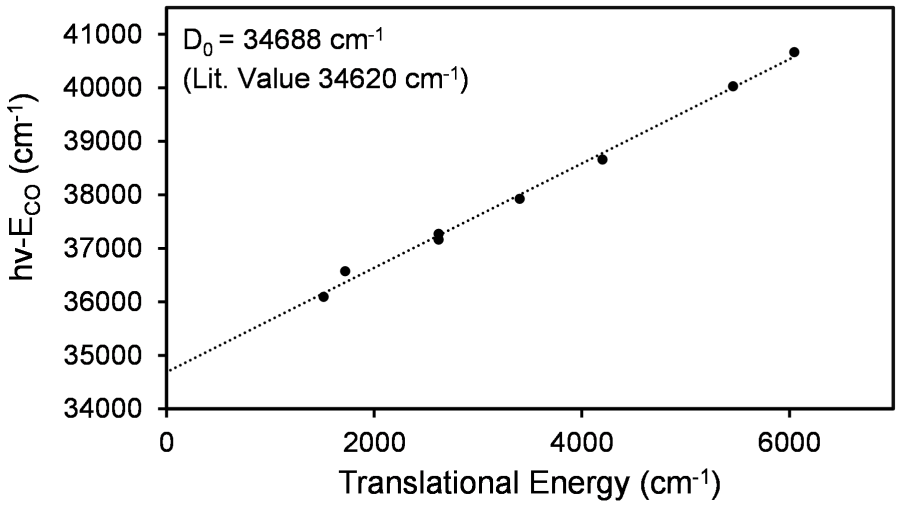

Figure 3.4: The translational energy analysis of a series of Q-branch peaks at CO(v = 0): j = 55, 58, 64, 67, 70, 74 and CO(v = 1) j = 61 and 64. The experimentally determined dissociation energy is in good agreement with reported literature values.[21, 23, 7] This figure is adapted from Ref. [21].[2]

The unexpected appearance of the Q branch can be explained by intensity borrowing from the nearby C($^1\Sigma^+$) state. The j-dependent mixing of the E and C states of CO has been well documented at low j_{CO}.[88] As expected for a Q branch Σ-Σ transition, the Q branch images are dependent only on $\beta_{\mu v}$, further suggesting that the Q branch intensity originates primarily from the C state. For a given rotational state, the $\beta_{\mu v}$ value extracted from the Q branch image agrees with the $\beta_{\mu v}$ value extracted from the S and R branch images. Additionally, the observed structure of both the Q and R branches can be simulated utilizing the reported CO(v = 1) and CO(v = 0) populations originating from the S branch of the E-X transition.[21]

$\beta_{\mu v}$ and $\beta_{\mu j}$ were extracted from several ion images across the CO(v = 1) rotational distribution. A representative set of sliced images resulting from the photodissociation of OCS near 214 nm is shown in Figure 3.5. The angular distributions shown to the left of each image were extracted from the inner ring. (The signal close to the center of the image is a non-resonant signal whose origin has not been identified.) The angular distributions of image intensities can be described by weighted sums of Legendre polynomials. For a one-photon dissociation and two-photon probe process, the

use of up to 6th order polynomials is required and orders greater than six may be neglected in the semiclassical limit. Additionally, in the high-j semiclassical limit contributions from coherence effects to the angular momentum polarization of CO are $1/j$ dependent and are thus negligible for the rotational states presented here.[30]

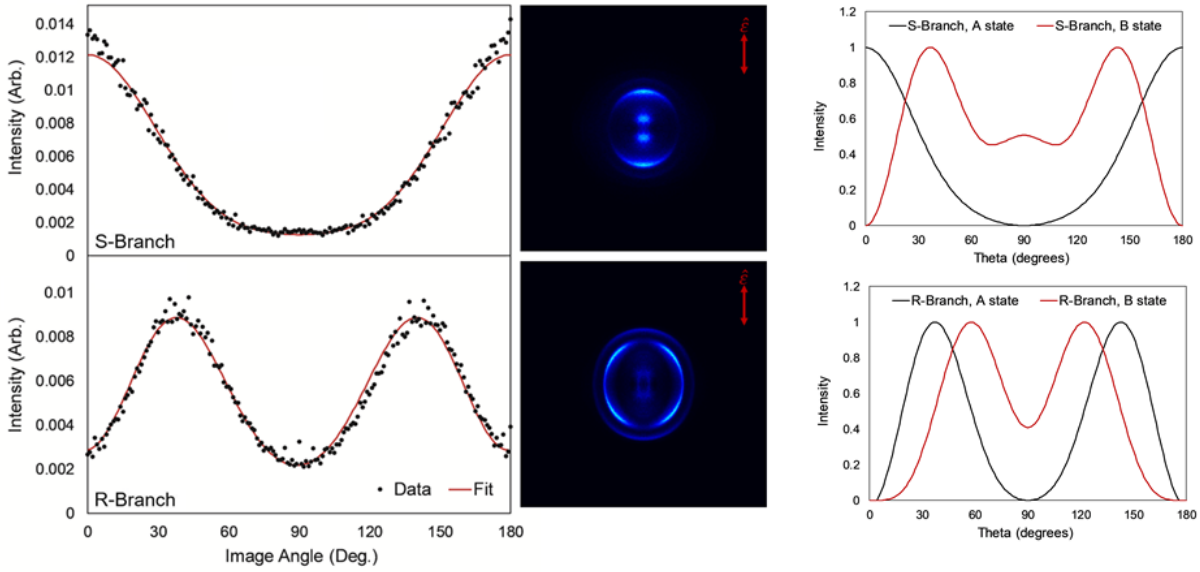

Figure 3.5: CO($v = 1$) images at $j = 58$ with the corresponding angular distributions. The top panels show a representative sliced S branch image with the corresponding angular distribution. The bottom panels show a representative R branch image with the corresponding angular distribution. Both angular distributions shown are of the inner ring which corresponds to CO($v = 1, j = 58$), while the outer ring corresponds to CO($v = 0, j = 57$). The experimental data are shown as black dots and the forward convolution fit is shown as a red curve. Angular distributions originating from case B and C, the main limiting cases used to describe the A and B state of OCS, are shown on the right.

Our forward convolution fit to the observed image anisotropy parameters uses Dixon's five limiting cases [14] as a basis set and allows $\beta_0^0(44)$ to float as an additional fitting parameter, as described in Wei *et al.* [82]. $\beta_{\mu v}$ and $\beta_{\mu j}$ can then be computed from the fitted parameters. In the absence of parent rotation all of the interatomic forces all lie in the molecular plane. Thus only the three limiting cases with $v \perp$ j provide significant contributions to the bipolar moments. For our

experimental geometry, the forward convolution fit to the angular distributions is less sensitive to the value of $\beta_{\mu j}$ than to either $\beta_{\mu v}$ or $\beta_{v j}$ (Dixon's $\beta_0^0(22)$). In the case of 2+1 REMPI there are a total of nine bipolar moments, of which five make some contribution to the rotational alignment. The sensitivity to $\beta_{\mu j}$ is reduced due to four additional bipolar moments that contribute to the rotational alignment.

In order to quantify the error of both $\beta_{\mu v}$ and $\beta_{\mu j}$ for each rotational state we used a Monte Carlo method. Each of the 5 limiting case weights and $\beta_0^0(44)$ were calculated from a random number generator whose output values spanned the range of its weight or moment. These randomly generated values were then used to calculate angular distributions using the forward convolution method mentioned earlier. For each image pair a total of one million random sets of values were generated. A χ^2 criterion was set to return approximately one hundred valid fits for every one million random iterations. The optimized values of of $\beta_{\mu v}$ and $\beta_{\mu j}$ appear in Figures 3.6 and 3.9, along with error bars representing the standard deviations of these accepted fits.

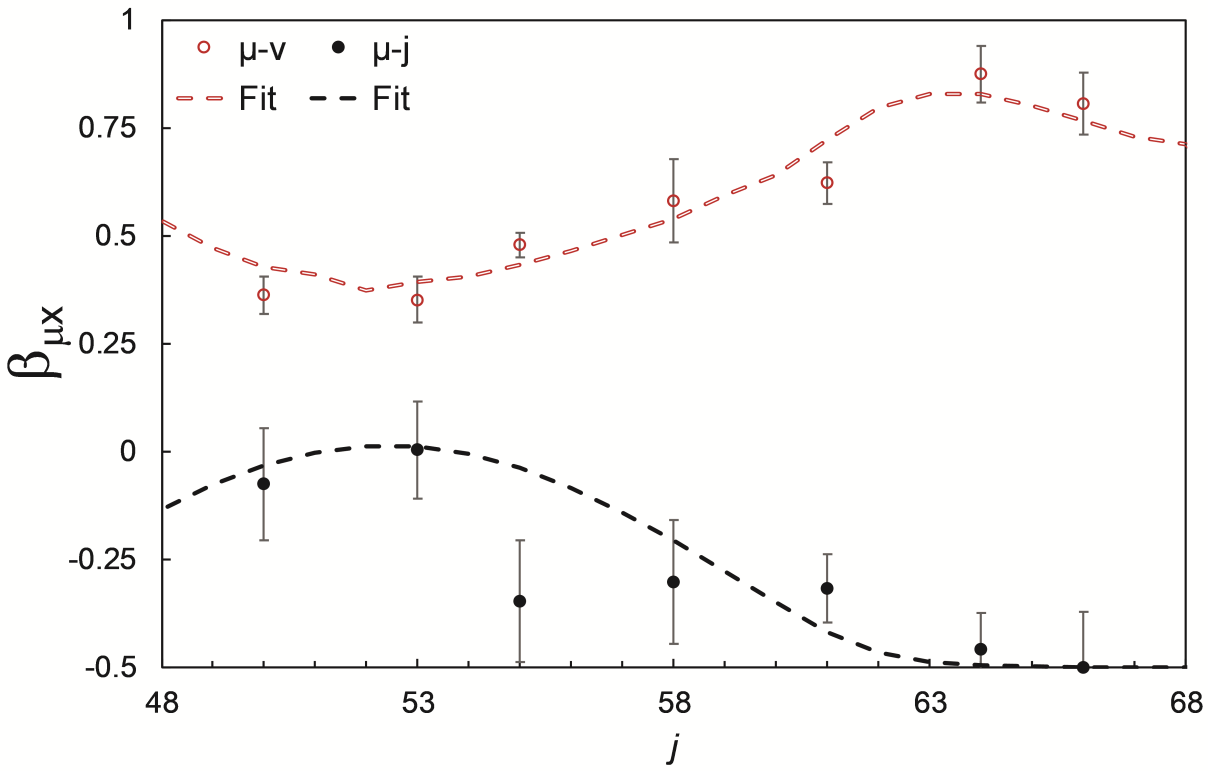

Figure 3.6: CO(v = 1) resulting from the photodissociation of OCS at 214 nm. The $\beta_{\mu v}$ and $\beta_{\mu j}$ values, determined using the forward convolution fitting method, are shown as open red and closed black circles respectively. The dashed lines correspond to the corresponding bipolar moments from the three-Gaussian model calculated using 3.1 and 3.3.

The CO(v = 1) rotational distribution can be decomposed into the relative contributions of the A and B states by simultaneously fitting the rotational populations, $\beta_{\mu v}$, and $\beta_{\mu j}$ as functions of j_{CO}. OCS excited to the A state can dissociate on two different pathways. In the quasiclassical model, trajectories can remain via the A state surface, producing final rotational states similar to the B state dissociation, or can make transitions from the A state surface to the ground X state surface.[5, 2] Trajectories that change surfaces before experiencing the strong restoring force from the residual bending potential on the A state surface produce higher final j_{CO} than those that do not. Given the Gaussian shapes of the rotational distribution components in both the experimental data and trajectory calculations throughout the absorption band, we have chosen to use three adjustable Gaussians to describe the pure A, pure B, and nonadiabatic transition ("X") components of the

CO rotational distribution.[2] The position, width, and height of each of the three Gaussians were adjusted manually in order to obtain the best fit to the CO($v = 1$) rotational distribution and the available $\beta_{\mu v}$ and $\beta_{\mu j}$ values simultaneously. During the fit, the $\beta_{\mu v}$ values were calculated for each j_{CO} using

$$\beta_{\mu v} = \frac{1}{2}\left(\frac{-f_B(j) + \beta_A(j)\,(f_A(j) + f_X(j))}{f_B(j) + f_A(j) + f_X(j)}\right). \tag{3.1}$$

The fractional contribution $f_B(j)$ of the B state at a specific j_{CO} is multiplied by $-1/2$, the limiting B state value for the $\beta_{\mu v}$ bipolar moment. The contribution from the A and X states to the $\beta_{\mu v}$ bipolar moment is proportional to one half of the A state anisotropy parameter, $\beta_A(j)$, determined by the surface hopping calculations on the A and X states. $\beta_A(j)$, computed as part of the work described in Ref. [22], is shown in figure 3.7 for both $v = 0$ and $v = 1$. Shown below is the general form of the Gaussian equation and the corresponding paramters used in the CO($v = 1$) fits in Figure 3.3 and Table 2.1 respectively where σ corresponds to the width of the Gaussian, μ determines the maximum of the Gaussian, and A is used as a scaling factor for the intensity of the Gaussian.

$$f_i = A\frac{1}{\sigma\sqrt{2\pi}}\exp\left(\frac{-(x-\mu)^2}{2\sigma^2}\right) \tag{3.2}$$

Table 3.1: Parameters used in the three Gaussian fitting for the CO(v=0) data at 214 nm.

	B	A	X
σ	2.9	4.3	2.3
μ	58	62	71
A	0.141	0.535	0.15

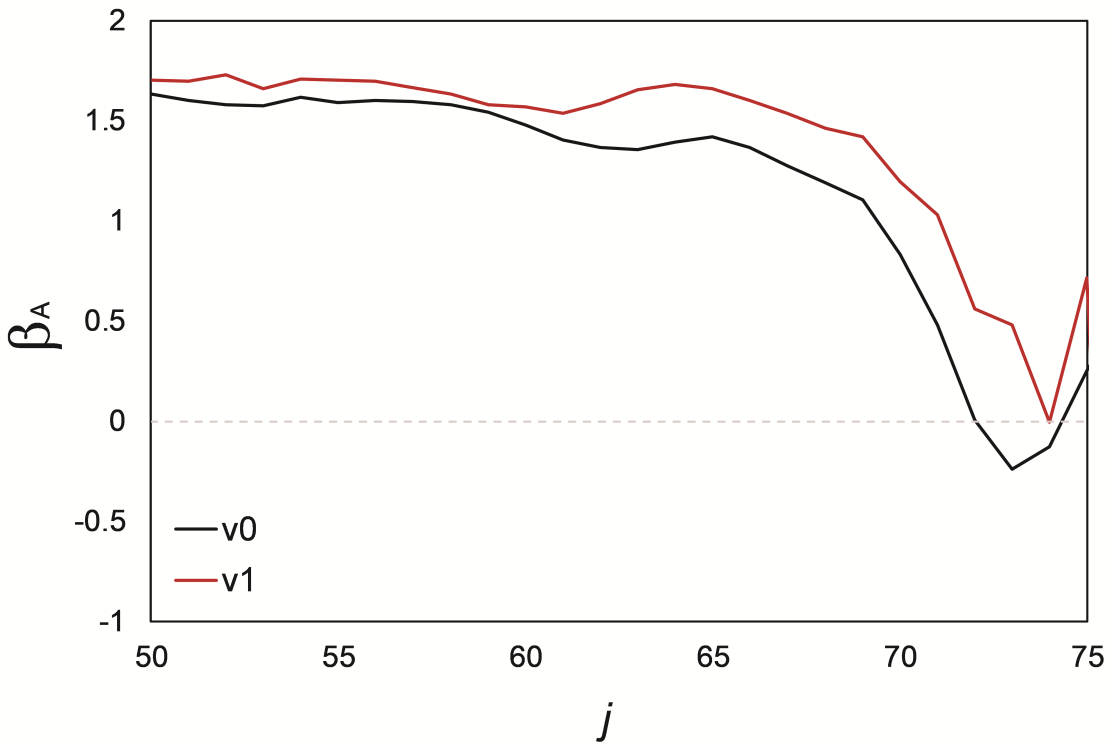

Figure 3.7: The calculated β_A value for 214 nm photodissociation is shown as the solid red line. This β_A value is used in equation 3.1. This value accounts for the j-dependent changes in non-axial recoil and the changes in the transition dipole moment during dissociation.

We use this approach to the A and X state contributions in order to account for the j_{CO}-dependent extent of nonaxial recoil and orientation of the OCS transition dipole moment. The $\beta_{\mu j}$ values were calculated for each j_{CO} using

$$\beta_{\mu j} = \frac{f_B(j) - \frac{1}{2}(f_A(j) + f_X(j))}{f_B(j) + f_A(j) + f_X(j)}. \tag{3.3}$$

Here, unlike equation 3.1, the limiting values of +1 for excitation to the B state and $-\frac{1}{2}$ for excitation to A (with or without later transition to X) are used, as appropriate for $J = 0$ parent OCS. Unlike in equation 3.1, it is not necessary to weight the result by β_A since the rotational angular momentum vector remains perpendicular to the molecular plane, and is thus unaffected by the bending motion during dissociation. Equations 3.1 and 3.3 are written for unnormalized f_A, f_B,

and f_X, each proportional to the height of the corresponding Gaussian for a specific j_{CO}; in the text below, the values are normalized by division by the total height (for j-specific fractions) or area (for overall contributions) so they sum to 1.

The results of this fit for $v = 1$ are shown in Figures 3.3a and 3.6. While the X component can be determined confidently simply from the rotational distribution, the vector correlation moments are important to set the relative intensities of the Gaussians corresponding to rotational distributions from pure A and B state dissociations. The modeled $\beta_{\mu v}(j)$ curve, which uses the trajectory-determined $\beta_A(j)$ to relate the Gaussian parameters to the predicted $\beta_{\mu v}$, yields a remarkably good match to the experimental data for $\beta_{\mu v}$. The $\beta_{\mu j}$ also fit the experimental data reasonably well, with the exception of $j_{CO} = 55$. This value was consistently low over several sets of images. There is currently no explanation for this difference at this time.

In Figure 3.3b the weighted trajectory calculations previously published in Wei *et al.* are shown.[22] The trajectory calculations were carried out on the A/X and B surfaces independently, then weighted by a ratio of 2:1 A state to B state. This weighting is the result of an extrapolation of fractional B state contributions from wavepacket calculations done at wavelengths ranging from 288 nm down to 223 nm, and is close to the value 0.31 obtained directly from Fig. 2b of McBane *et al.* [2].

The CO($v = 1$) rotational distribution extends from $j_{CO} = 48$ to $j_{CO} = 69$. The two distinct peaks in the model are at $j_{CO} = 56$ and near $j_{CO} = 65$. These peak positions are nearly identical to the maxima in the weighted trajectory calculations; the lower j_{CO} peak is shifted by one j_{CO}. The B state rotational distribution from the trajectory calculations is slightly wider than the experimental model. However, the fitted A state rotational distributions agree reasonably well. The most noticeable differences between the fits and the weighted trajectory calculations are the change in the relative contribution from the B state and the larger high-j_{CO} peak in the data and empirical fit. The j-dependent f_B contribution can be calculated from

$$f_B(j) = \frac{2\beta_{\mu j}(j) + 1}{3}. \tag{3.4}$$

The fitted $\beta_{\mu j}$ curve has its maximum at $\beta_{\mu j} = 0.013$ at $j_{CO} = 52$, corresponding to $f_B = 0.342$ there, while the calculated $\beta_{\mu j}$ curve peaks at roughly $\beta_{\mu j} = 0.5$ at $j_{CO} = 49$ corresponding to $f_B = 0.67$. f_B for both the fitted and trajectory surface hopping results are shown in figure 3.8.

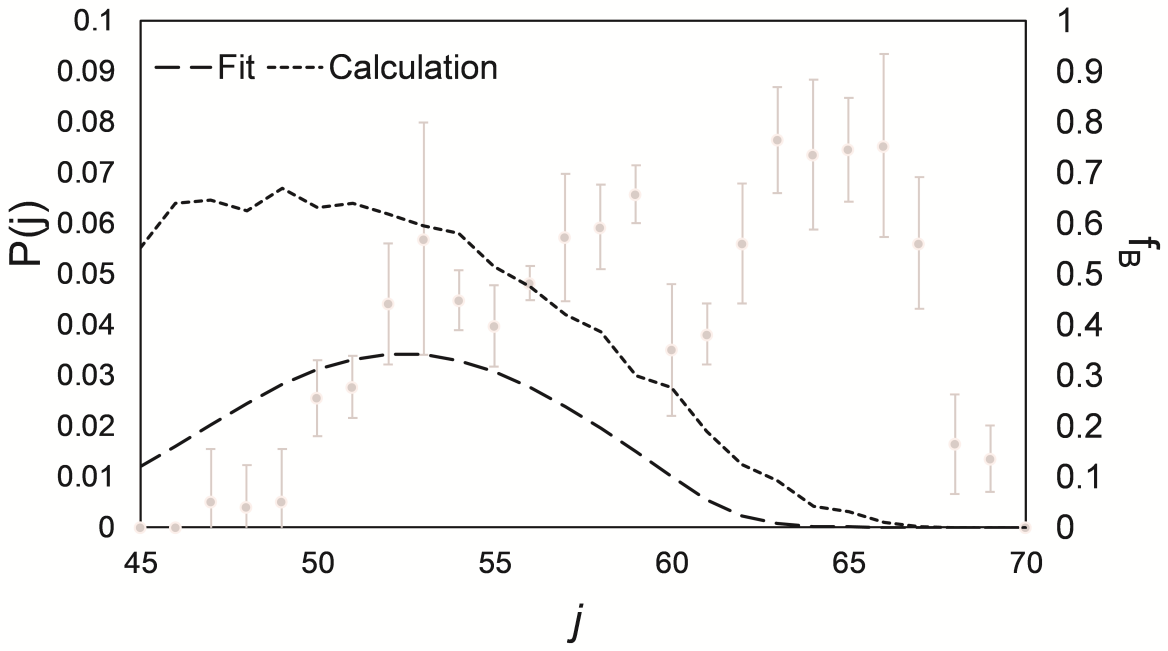

Figure 3.8: The f_B contribution for $v = 1$as a function of j is shown. The f_B from the experimental fit is shown as a dashed black line while f_B originating from the classical trajectory calculation is shown as a dotted black line. The corresponding rotational distribution is shown in grey.

These results indicate a stark difference between the experimental fit and the weighted trajectory calculation result particularly at $j_{CO} < 55$ where the contributions from the B state are most prominent. The overall B state contribution determined from the experimental model, $\sim$ 14%, is $\sim$ 2.4 times smaller than the 33% B state contribution used for weighting the trajectory calculations.

In the three-Gaussian model the contribution of the surface hopping component can be adjusted independently. The X-state component accounts for $\sim$ 40% of the rotational distribution in the fitted model, while it accounts for only 25% in the trajectory surface hopping calculations. The

notable underestimation of the high-j_{CO} peak in the trajectory surface hopping calculation appears to imply an underestimation of the hopping probability for trajectories leading to CO(v = 1). The nonadiabatic coupling matrix element function used to determine the hopping probability in the work of McBane *et al.* did not include any dependence on the CO bond length. This approximation was reasonable for a reaction that produced very little vibrational excitation. However, the trajectories leading to v = 1 necessarily involve stretching or compression of the CO bond during the dissociation. If the coupling strength does depend on the CO bond length (as it does, for example, in ozone photodissociation [89, 90]), the surface hopping calculations can be expected to incorrectly estimate the size of the high-j_{CO} peak.

The differences in the overall contributions of the A and B states between the model and the electronic structure predictions can likely be attributed to several different effects. Remaining errors in the transition dipole functions for the two electronic states and possibly the calculated vertical excitation energies of the surfaces are certainly possible. The transition dipole moments are difficult to compute accurately, and a change in the B state TDM of more than a factor of two was reported in McBane *et al.* [2] compared to the initial work from reference [4]. Changes in the relative vertical excitation energies of the A and B states can also cause shifts in the relative contributions from each state.[2, 91] A relative change in the vertical excitation energies alone of approximately 1000 cm^{-1} would be necessary to account for the changes in the relative excitation probability between the two states. This effect was investigated for CO(v = 0) where more experimental data exist and is discussed below.

3.2.2 CO(v = 0) product internal state distributions

In an effort to determine whether the reduced contribution of the B state to the absorption was isolated to CO(v = 1) or also affected CO(v = 0), we have reexamined the CO(v = 0) data from Wei *et al.* [22] using the three-Gaussian model. To determine $\beta_{\mu v}$ and $\beta_{\mu j}$ we collected additional sets of sliced images across the CO(v = 0) rotational state distribution, at $j = 51, 53, 55, 67$, and 69, to be used in conjunction with the previously published data.

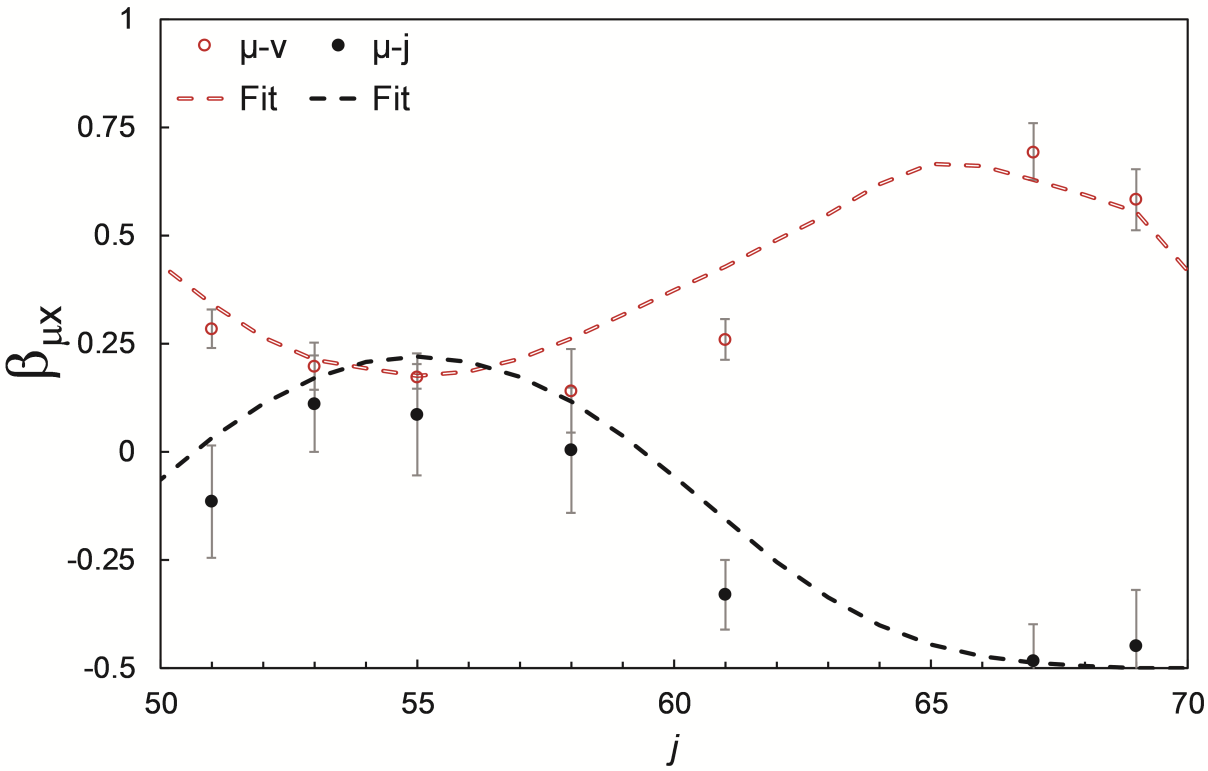

Figure 3.9: Experimental CO(v = 0) $\beta_{\mu v}$ and $\beta_{\mu j}$ are shown in open red and closed black circles respectively. The dashed lines correspond to the resulting bipolar moments from the ratio between the A and B state contributions in the experimental model which were calculated using equation 3.1 and 3.3. The bipolar moments at j_{CO} = 58, 61, and 72 are taken from Wei *et al.* [22]

The angular distributions from these sets of images were analyzed using the forward convolution method described earlier. The j-dependent bipolar moments are shown in Figure 3.9 with $\beta_{\mu v}$ in red and $\beta_{\mu j}$ in black. The dashed curves correspond to the bipolar moments derived from the ratio between the A/X and the B state from the three-Gaussian model. As with the CO(v = 1) the $\beta_{\mu v}$ and $\beta_{\mu j}$ bipolar moments were calculated using equations 3.1 and 3.3. The model fits the entire rotational distribution well, even at the highest j_{CO}. The two highest experimental data points, j_{CO} = 69 and 72, have minimal contribution from the B state of OCS so the $\beta_{\mu v}$ bipolar moment for these two j_{CO} states should be equal to the $\beta_{\mu v}$ value from the A state absorption. The large deviation from the limiting value of $\beta_{\mu v}$ = 1 illustrates the increasing effect of nonaxial recoil as a function of j_{CO} captured in the empirical model of Demyanenko *et al.* [92]. The $\beta_{\mu j}$ bipolar

moment reaches a maximum near 0.22 $j_{CO} = 55$, indicating $f_B = 0.47$ at $j_{CO} = 55$, while the calculation predicts a maximum value $f_B = 0.72$ for $j_{CO} = 52$. The f_B for $v = 0$ as a function of j is shown in figure 3.10.

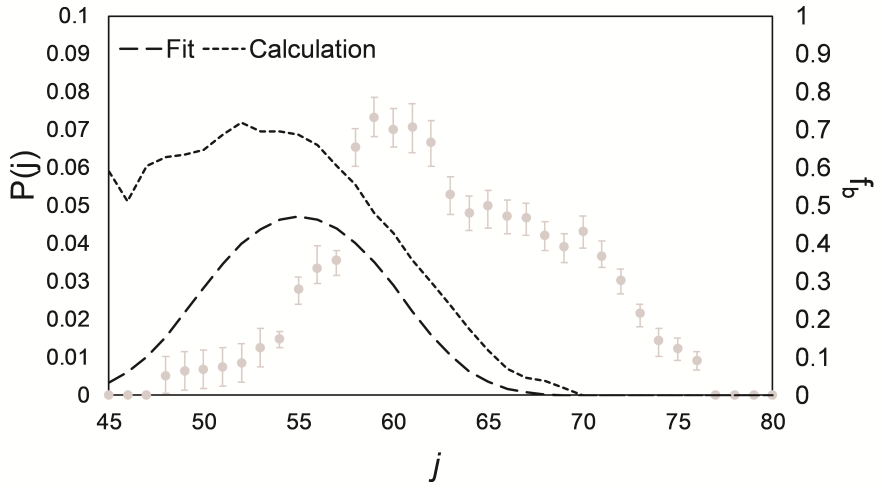

Figure 3.10: The f_B contribution for CO($v = 0$) as a function of j is shown. The f_B from the experimental fit is shown as a dashed black line while f_B originating from the classical trajectory calculation is shown as a dotted black line. The corresponding rotational distribution is shown in grey.

Sivakumar et al. presented a similar analysis for CO($v = 0$) at a photodissociation wavelength of 222 nm.[6] In contrast to our 214 nm results, their j-dependent f_B closely resembles the weighted trajectory calculations at 222 nm, peaking at $f_B = 0.7$ at $j_{CO} = 50$.

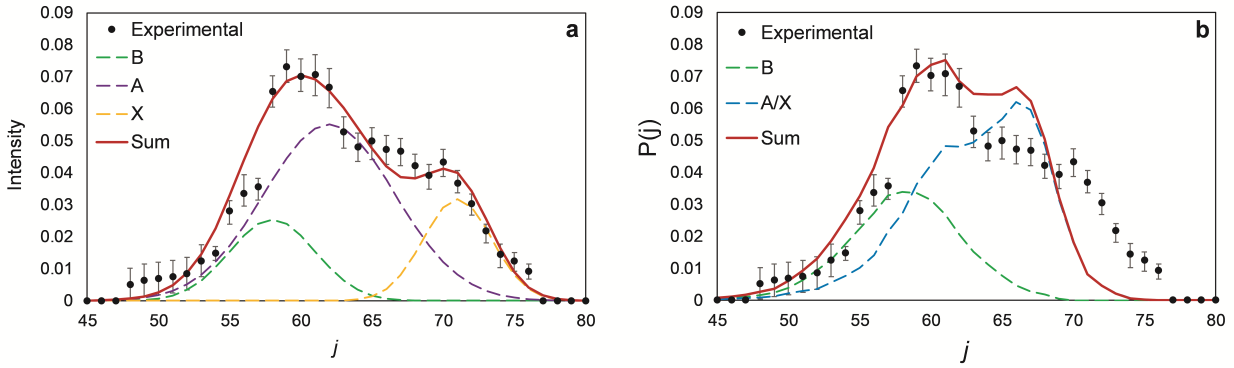

Figure 3.11: CO(v = 0) rotational distribution from Wei *et al.* is shown as filled circles. The contribution from the A state is shown as the purple dashed line, the contribution from the B state is shown in green dashed line, and the contribution from the X state is shown as the yellow dashed line. The contribution from the A/X trajectories is shown in blue. The sum is shown as the solid red line. (a) The fit using the Gaussian model is shown on the left. (b) Results from weighted trajectory calculations are shown on the right.[22]

In Figure 3.11a the experimental rotational distribution has been decomposed into contributions from the A and B states of OCS following the same procedure used for the CO(v = 1) rotational distribution. In Figure 3.11b the previously published trajectory calculations are shown for the OCS originating on the A and B state surfaces. There are two major differences between Figure 3.11a and Figure 3.11b. First the B state contribution in the experimental model is $\sim$ 1.7 times smaller than the B state contribution in the weighted trajectory calculations. The contribution of the B state to the overall rotational distribution is $\sim$ 20%, while that for CO(v = 1) was 14%. The second major difference between the experimental model and the trajectory calculations is in the highest rotational states. The trajectory calculations do not result in enough population for $j_{CO} > 70$. These high j_{CO} states originate from trajectories that surface hop early from the excited A state to the ground X state during dissociation.

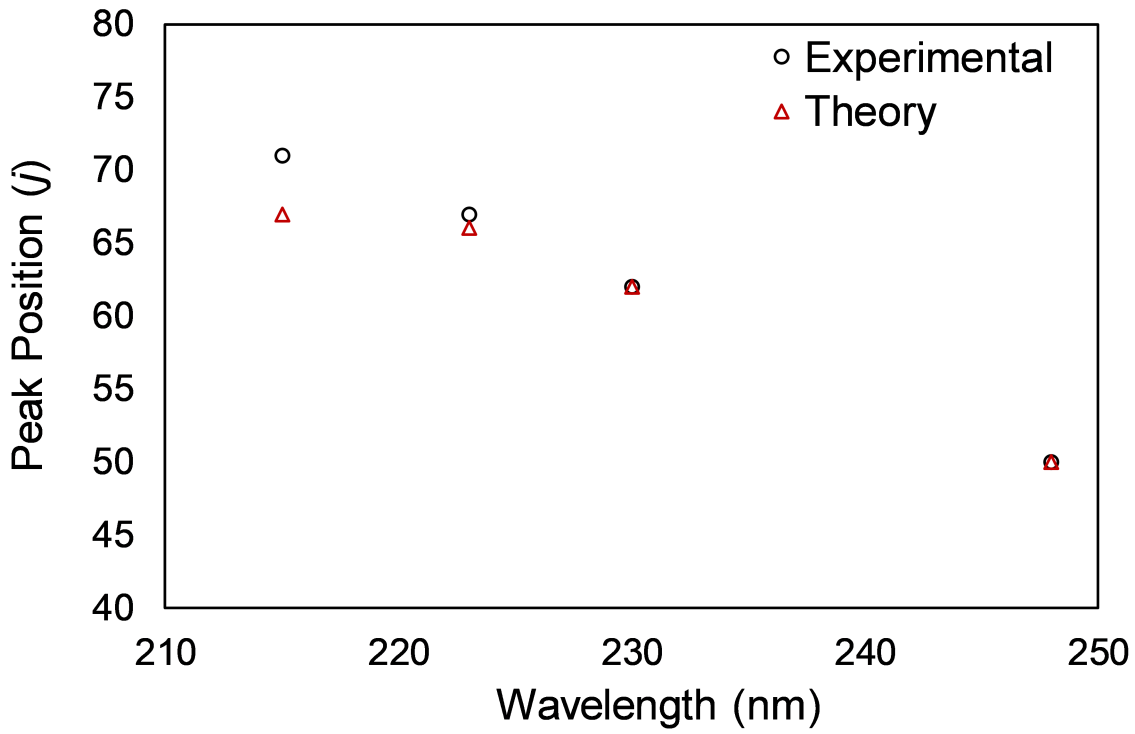

Figure 3.12: The peak position of the surface hopping component, X, comparing the differences between the experimental data and the theoretical position as a function of dissociation energy. As the excitation energy increases, there is a clear divergence between the experimental fits and the theoretical predictions at 214 nm. [4, 5, 6, 7, 8]

Trajectories that surface hop early do not experience the strong restoring force on the A state surface, allowing these trajectories to reach the highest experimental j_{CO} states. In the trajectory calculations, the peak position of the surface hopping component is centered around j_{CO} ~66-67 while the peak position in the model is several rotational states higher at $j_{CO} = 71$. In figure 6 from Wei *et al.* the maximum accessible rotational state for the trajectory calculations is shown to be $j_{CO} \sim 75$.[22] The highest j_{CO} states cannot be accessed by the trajectory calculations, indicating a possible shortcoming in the balance between the initial angular momentum generated from the bending potential and the restoring force of the excited A state.

Since the trajectory calculations do not include vibrationally excited parent OCS it is possible that the highest rotational states originate from vibrationally excited parent. In order to determine the contribution from vibrationally excited OCS, images were collected at j_{CO} = 69, 72,

and 75. Their corresponding speed distributions were used to compare the intensity between the OCS($v_2 = 0$) and OCS($v_2 = 1$). For each of these images, the peaks were well resolved, allowing for accurate determinations of the contribution of each channel. Only in $j_{CO} = 75$ was there significant OCS($v_2 = 1$), equal to 18.7% of the overall intensity, while in $j_{CO} = 69$ and 72, there were only 4.9% and 3.5% OCS($v_2 = 1$) respectively. These low values rule out OCS($v_2 = 1$) as a major contributor to the high j_{CO} side of the rotational distribution.

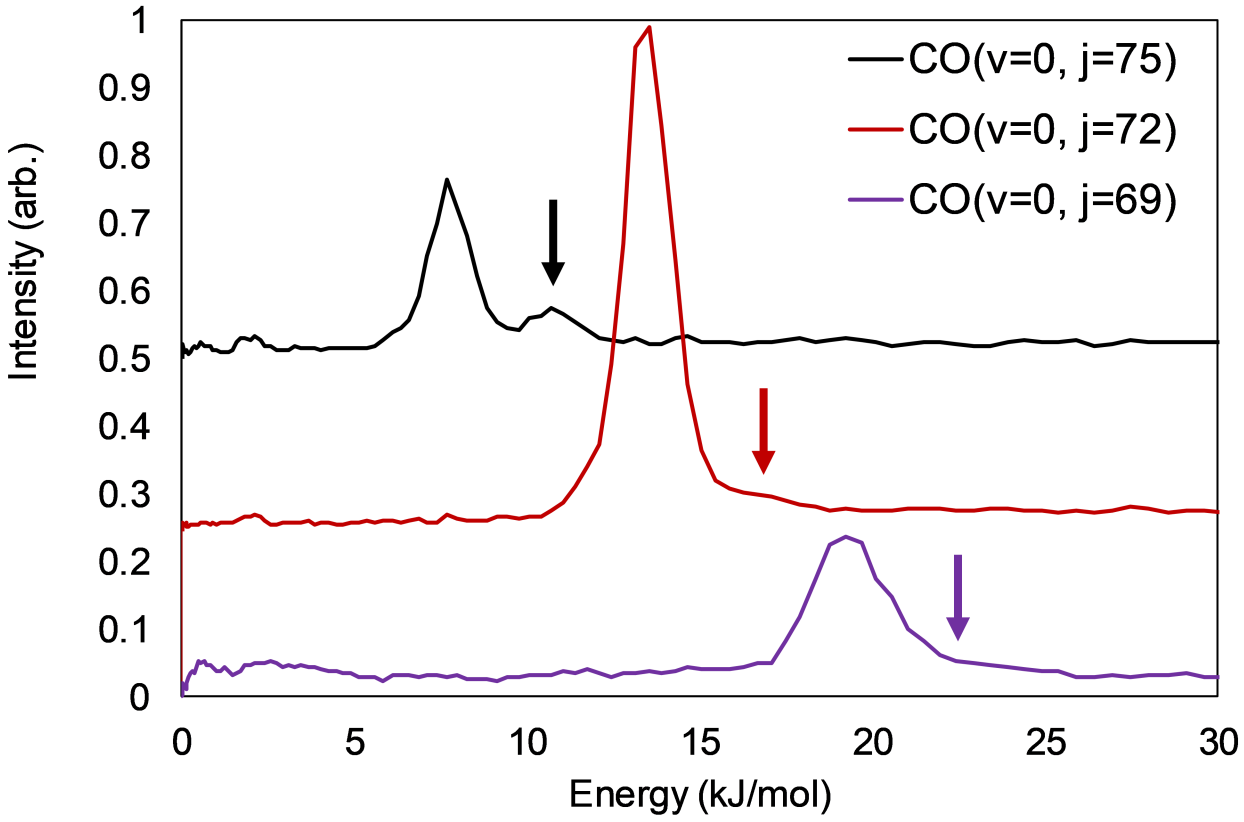

Figure 3.13: Total energy distributions of CO images collected at $j = 69$, 72, and 75. The main peaks at each of the CO rotational states presented are the OCS($v_2 = 0$) CO fragments. Visually, the only the CO(j=75) has clear parent contribution from the OCS($v_2 = 1$) bending motion. The expected positions for OCS($v = 1$) at each rotational state is represented by an arrow.

3.2.3 OCS Absorption Cross Section

In order to determine the contribution of each electronic state to the overall OCS absorption cross section we have employed the three-Gaussian model to perform a similar analysis on previously reported data at three additional photolysis wavelengths: 223 nm, 230 nm, and 248 nm.[5, 6, 7, 8] For the photolysis wavelengths of 230 nm and 248 nm there were no $\beta_{\mu j}$ data available for the analysis, so only $\beta_{\mu v}$ was used in the analysis. The fractional contributions of the B state to the total rotational distribution for each photolysis wavelength were determined to be 0.47±0.05, 0.44±0.02, and 0.62±0.06 at 223, 230, and 248 nm respectively, while the fractional contribution at 214 nm was 0.20±0.04.

Attempts were made to determine the overall contribution of each electronic state to the overall UV absorption spectrum using the wavelength dependent excited state contributions and Gaussians to model the separate A and B state absorption spectra. While the electronic potentials generally result in a Gaussian shape on the blue side of the absorption cross section, the red sides show long non-Gaussian tails. This non-Gaussian feature has a pronounced effect on the results particularly at 248 nm. Due to the non-Gaussian shape of the A and B state absorption spectra caused by the curvature of the dissociative potentials and an insufficient amount of experimental data across the first absorption band of OCS, we determined that such a quantitative analysis was not possible.

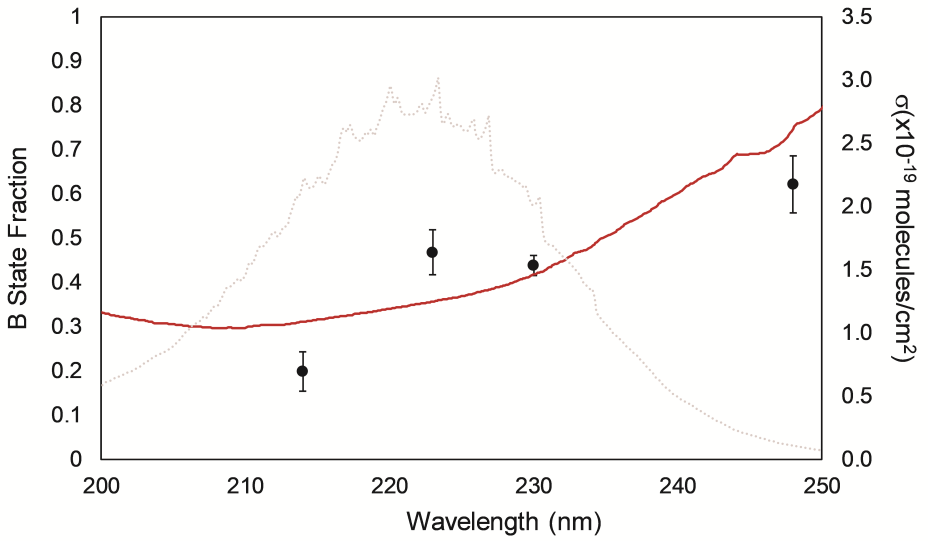

Figure 3.14: The empirically determined B state fractions at 214, 223, 230, and 248 nm, shown as black circles. The error bars describe the error associated with the rotational distribution and $\beta_{\mu\nu}$. The calculated B state fraction, shown as a red line, is determined from the calculated absorption cross section for the A and B states of OCS shown in figure 2b from McBane *et al.* .[2] Attempts to fit the experimental absorption spectrum from reference [16], shown in grey, are described in the main text. [4, 5, 6, 7, 8]

Figure 3.14 shows a comparison between the fractional B state contribution at the four different experimental wavelengths mentioned above and the fractional B state contribution determined from the calculated absorption cross section, shown in Figure 2b from McBane *et al.* , by taking the B state absorption cross section divided by the sum of the A and B state absorption cross sections.[4, 5, 6, 7, 8]. The error bars are representative of the uncertainties associated with the rotational distributions and $\beta_{\mu\nu}$ values. In Figure 3.14 the general upward trend of the calculated f_B is reasonably captured by the experimental data. However, near 214 nm the calculated fractions have plateaued near $f_B \sim 0.3$ while the experimental result at 214 nm is about 40% smaller. In both the CO($v = 1$) and CO($v = 0$) distributions the contribution from the B state is overestimated in comparison to to the experimental f_B.

In an attempt to gain some insight into the cause of these discrepancies, the vertical excitation energy of the calculated absorption cross sections for each electronic state were shifted by changing

the peak position of the A and B states.

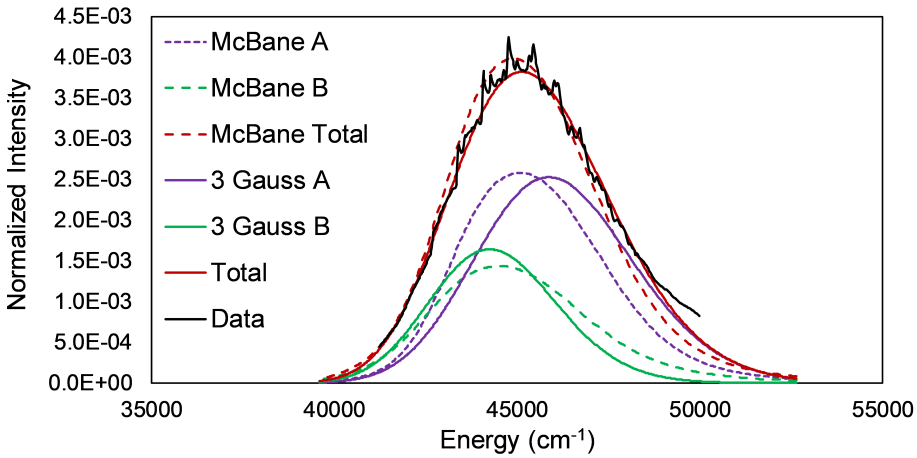

Figure 3.15: The experimental absorption cross section of OCS shown in black. The fitted A and B states of OCS are represented by solid purple and green respectively, while A and B states from the calculated A and B state absorption cross sections are represented by dashed purple and green lines respectively. The sum of the experimental model is shown as a solid red line while the sum of the calculated is shown as a dashed red line. [2, 16]

In Figure 3.15 the experimental absorption cross section collect at 170 K is shown in black.[16] The theoretical absorption cross section and its components are shown as dashed lines while the experimental model is shown as solid lines. The A state is shown in purple, the B state is shown in green, and the overall absorption cross section is shown in red. In general, the shape of each component is very similar when comparing the cross sections derived from the experimental model to the calculated absorption cross section. The most apparent difference is the position of the A state which is shifted by 684 cm^{-1} when comparing the experimental model to the theoretical absorption cross section. The position of the B state also shifts a more modest -256 cm^{-1} when comparing the experimental model to the calculated absorption cross section. The vertical excitation energy is difficult to accurately calculate. These shifts of 684 cm^{-1} and -256 cm^{-1} are account for approximately 2% and 0.5% of the vertical excitation energy for each state. In 2013 McBane *et. al.* adjusted the vertical excitation energy between the X and A state by $\sim$ 200 cm^{-1}

to better fit the experimental absorption cross section citing the difficulties in calculating accurate vertical excitation energies.[2] It is also possible the calculated transition dipole moments (TDMs) are the cause of the discrepancies between the calculated B state fractional contributions and the experimentally determined ones. Previous work has demonstrated the difficulty of computing these TDMs accurately.[4, 2] Errors in the accuracy of the TDMs of either one of the electronic states would result in a change to the fractional B state contribution and could account for the differences between the theoretical and experimental data. Without additional experimental data, the cause of the discrepancies between the experimental and calculated contributions of the A and B state could not be definitively determined.

3.3 Conclusion

We have reported the $\beta_{\mu v}$ and $\beta_{\mu j}$ bipolar moments resulting from the photodissociation of OCS at 214 nm for the CO($v = 1$) + $S^1(D_2)$ channel. An experimental model using three Gaussians to describe the rotational distributions originating from different electronics states was used to determine the contributions from the $2^1A'$(A) and $1^1A''$(B) states of OCS to the overall CO($v = 1$) rotational distributions. This experimental model was also extended to previously published measurements of the CO($v = 0$) rotational distribution at 214 nm. The experimental contributions from the B state of OCS for the CO($v = 1$) and CO($v = 0$) channels were $\sim$ 2.5 times smaller ($f_B = 0.14 \pm 0.04$) and $\sim$ 1.7 times smaller ($f_B = 0.20 \pm 0.04$) than predicted by previously reported trajectory surface hopping calculations from Wei *et al.* .[22] The empirical model was applied to three additional dissociation wavelengths: 223 nm, 230 nm, and 248 nm. The fractional B state contribution at each wavelength was compared to the calculated fractional B state contribution. Further studies are needed to determine the origin of the discrepancies between the calculated and experimental fractional B state contributions. Additionally discrepancies between the calculated surface hopping component at 214 nm has indicated a shortcoming in either the initial impulse along the bending coordinate or the coupling between the X and A states of OCS

4. PHOTODISSOCIATION DYANMICS OF HN_3 AT 256 NM, 271 NM, and 285 NM

The photodissociation dynamics of HN_3 are investigated at three different photodissociation wavelengths: 256 nm, 271 nm, and 285 nm. At each of these wavelengths, the speed dependent vector correlations are of the HN photofragments were measured. These speed dependent vector correlations provide insight in the correlated dynamics between the HN photofragment and the N_2 cofragment. By analyzing the HN images as a function of speed a small range of j_{N_2} states can be associated with each individual j_{HN} measurement providing information about the relationship between the two fragments. The three lower order bipolar moments $\beta_{\mu v}$, $\beta_{\mu j}$, and β_{vj} for the HN_3 photofragment have been previously reported in the literature at two dissociation wavelengths: 266 nm and 308 nm. Both of these wavelengths have shown the same general trend where $\beta_{\mu v}$ and β_{vj} have shown a gradual increase from slightly negative values at low j_{HN} to slightly positive values at high j_{HN}, while $\beta_{\mu j}$ remains relatively flat and near zero across the entire j_{HN} distribution.[24, 26, 65] As HN_3 begins to dissociate, the HN_3 molecule bends along the NNN bond. There are two vibrational modes that result in the NNN bend, the in-plane NNN bend (ν_5) and the NN-NH torsion (ν_6) on the ground state potential energy surface.[65] Since the HN_3 is excited via perpendicular transition, where the transition dipole moment is out of the molecular plane, the expected a result is a positive $\beta_{\mu j}$ parameter and preferential excitation of the A″Λ-doublet. Previous experimental measurements have shown the $\beta_{\mu j}$ parameter is near zero across the HN rotational distribution and no preferential excitation of either the Λ-doublet. Both of these observations can be explained by dissociation of HN_3 through both vibrational modes result in HN fragments that are rotating at ~ 45 deg to the molecular plan. The slow increase in the $\beta_{\mu v}$ and β_{vj} across the j_{HN} distribution can be explained by the increasing importance of the ν_6 torsional mode. As the HN fragment twists out of the molecular plane the HN_3 molecule dissociates along the central NN bond. The out of plane HN motion induced by the ν_6 torsional mode relaxes the expected values for the bipolar moments, thus as j_{HN} increases so do the $\beta_{\mu v}$ and β_{vj} bipolar moments.[65] Additionally, there has been one direct measurement of the N_2 photofragment at 285 nm, but due to significant noise associated with

m/z = 28 only the $\beta_{\mu j}$ value was reported to have positive alignment across the entire rotational distribution indicative of a perpendicular transition.[25]

In this section the rotational distributions measured at 256 nm, 271 nm, and 285 nm are compared to previous measurements reported in the literature at 248 nm, 266 nm, 285 nm, and 308 nm.[11, 24, 25, 26] In general the HN rotational distribution has been shown to be wavelength independent. The HN bipolar moments are present at all three dissociation wavelengths and are compared to previous measurements are 266 nm ad 308 nm. Additionally the first speed dependent vector correlations of the HN_3 photofragment are reported which provide some insight into the dynamics of the N_2 cofragment. The speed dependent $\beta_{\mu j}$ measured at 285 nm is compared with the $\beta_{\mu j}$ measured directly from the N_2 cofragment in Ref. [25].

4.1 Experiment

The experimental details have been previously described in detail in Section 2.4.2, but a short summary will be provided here. HN_3 is first synthesized by the reaction of stearic acid and sodium azide following Equation 2.16. The newly generated HN_3 is trapped in a glass bulb at a concentration of ~10% HN_3 in helium. The HN_3 helium mixture undergoes a free jet expansion through a pulsed valve into the source region, rapidly cooling the HN_3 and is subsequently collimated by a skimmer and crossed at 90° by linearly polarized light at 256 nm, 271 nm, and 285 nm with averages powers of ~ 2 mJ/pulse, ~ 1 mJ/pulse, and ~ 1.8 mJ/pulse respectively. Each of the three different wavelengths were used to both photodissociate the HN_3 and resonantly ionize the HN products via a 2+1 REMPI scheme. The resulting ions are then accelerated and velocity mapped onto a position-sensitive microchannel plate detector (MCP) with a P51 phosphor screen. The MCP timing was gated for a 100 ns to capture the whole crushed image. A Hamamatsu R928 photomultiplier tube or IDS uEye gated CCD camera was used to record the signal from the phosphor screen. The angular distributions from the crushed images were analyzed using the forward convolution method described in detail in Wei *et al.* [82]

4.2 Results and Discussion

The experimental and simulated REMPI spectra the photodissociation of HN_3 at 256 nm, 271 nm, and 285 nm are shown below in black and red respectively. In the case of the 271 nm and 285 nm spectra there were some difficulties fitting the intensity of all of the rotational branches simultaneously. In these two REMPI spectra, the Q and P branches were fit individually and the average fit is shown. While the intensities of each of the branches were different, the rotational distributions collected from each of the fits were very similar. The rotational distributions shown in Figure 4.2 consist of the averaged values between the two fits.

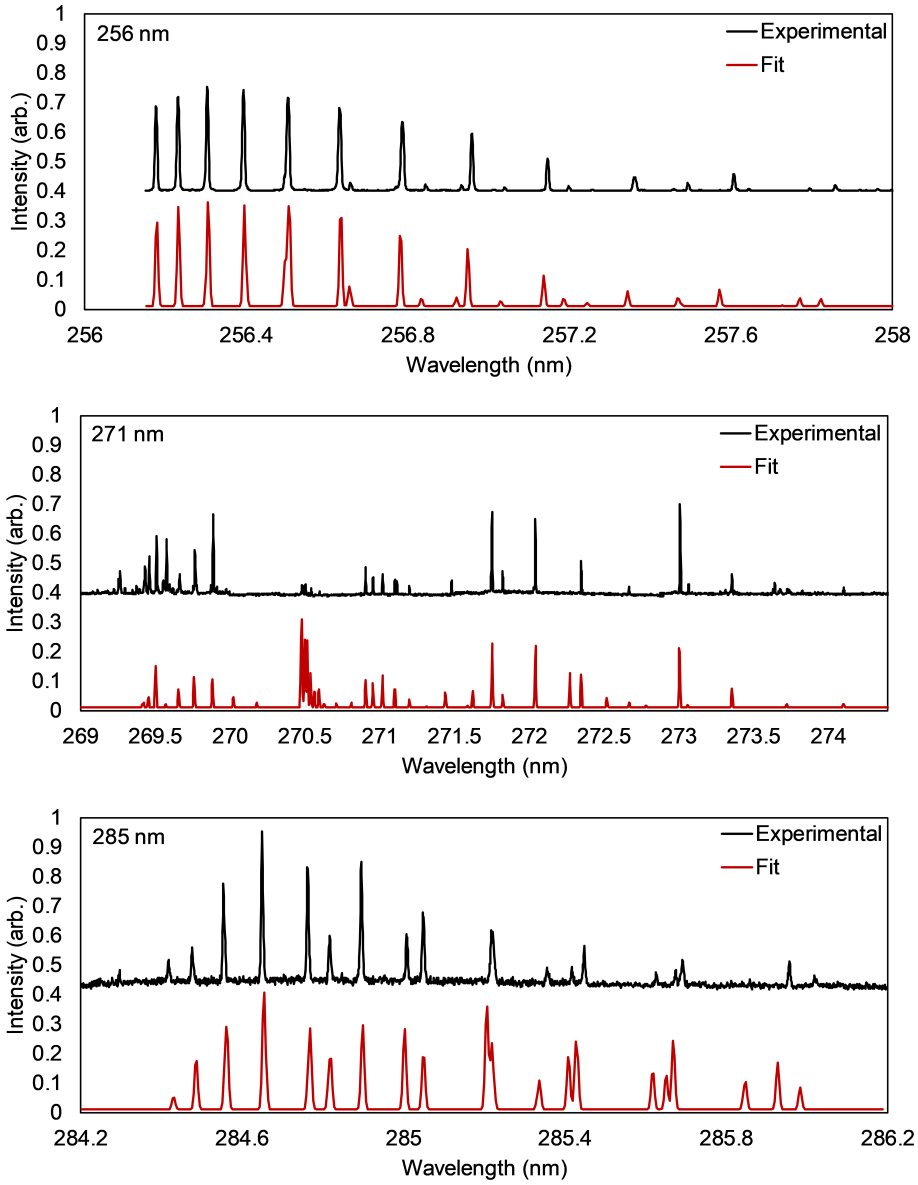

Figure 4.1: Experimental REMPI data resulting from the photodissociation of HN_3 near 256 nm, 271 nm, and 285 nm are shown above in black. The corresponding fits are shown in red. The constants used to fit the REMPI spectrum are shown in Table 1.6.

The experimental HN rotational distributions resulting from the photodissociation of HN_3 at 256 nm, 271 nm, and 285 nm are compared to four HN rotational distributions resulting from the photodissociation of HN_3 at 248 nm, 266 nm, 285 nm, and 308 nm found in the literature in Figure 4.2.[11, 24, 25, 26].

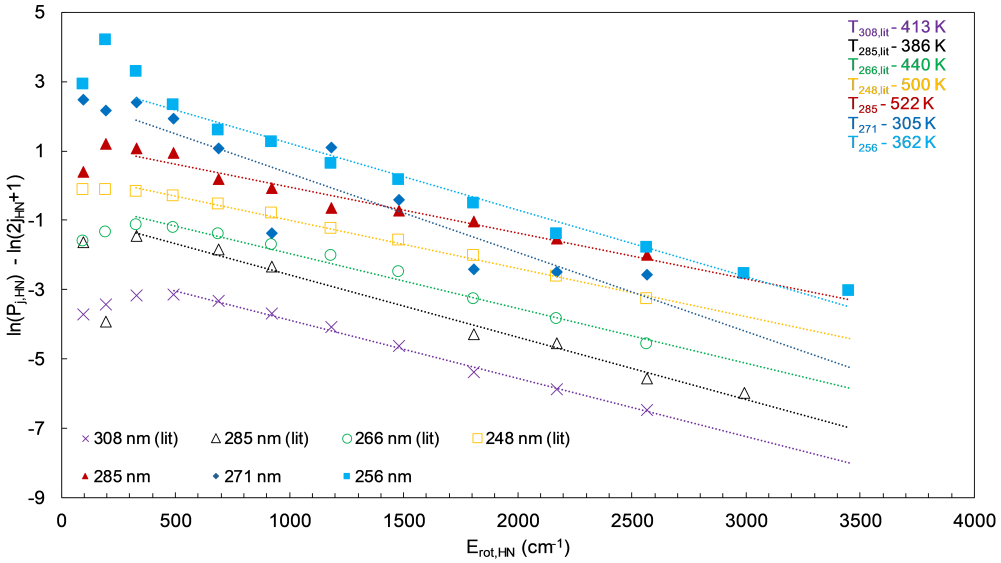

Figure 4.2: Rotational distributions resulting from the photodissociation of HN_3 at six different wavelengths: 248 nm, 256 nm, 266 nm, 271 nm, 285 nm, and 308 nm. Photodissociation wavelengths of 256 nm, 271 nm, and 285 nm were experimentally measured while the photodissociation wavelengths labeled as (lit) were adapted from the literature where 248 nm, 266 nm, 285 nm, and 308 nm were taken from Ref. [11], Ref. [24], Ref. [25], and Ref. [26]. Each data set is scaled by one along the y-axis for clarity.

The rotational distributions shown in Figure 4.2 are shown on a Boltzmann plot in order to describe each distribution by a single temperature value. It is important to note, there is no dynamical reason these distributions should be described by a Boltzmann distribution, but these distributions can be fit relatively well by a Boltzmann distribution which in turn provides a single value, temperature, for comparison. In the literature, the HN rotational distributions have been noted to be independent of dissociation wavelength. The measured 256 nm, 271 nm, and 285 nm HN rotational distributions are in reasonable agreement with previously reported measurements at the dissociation wavelengths of 248 nm, 266 nm, 285 nm, and 308 nm with the exception of 271 nm. At the 271 nm dissociation wavelength the rotational distribution is not well fit by a Boltzmann distribution. At $j_{HN} = 7$ the intensity is suppressed while at $j_{HN} = 8$ the intensity if particularly intense. These observations are likely not due to perturbations in the ($f^1\Pi \leftarrow a^1\Delta$) REMPI transition used at 271 nm since there is no evidence for this behavior in Ref. [17, 18]. The intensities in the ($f^1\Pi \leftarrow a^1\Delta$)

transition are shown to progress relatively smoothly with no perturbed intensities.[17, 18] These scans were not power corrected in data processing, but instead are typically collected while measuring the power every 0.1 nm across the scan. Since these experiments are multiphoton dependent, it is most likely these anomalous intensities are the result of poor control of the power across each scan. In order to confirm this hypothesis it would be necessary to rescan the 271 nm region to determine if these perturbations were in fact a real result of the dissociation of HN_3 at 271 nm.

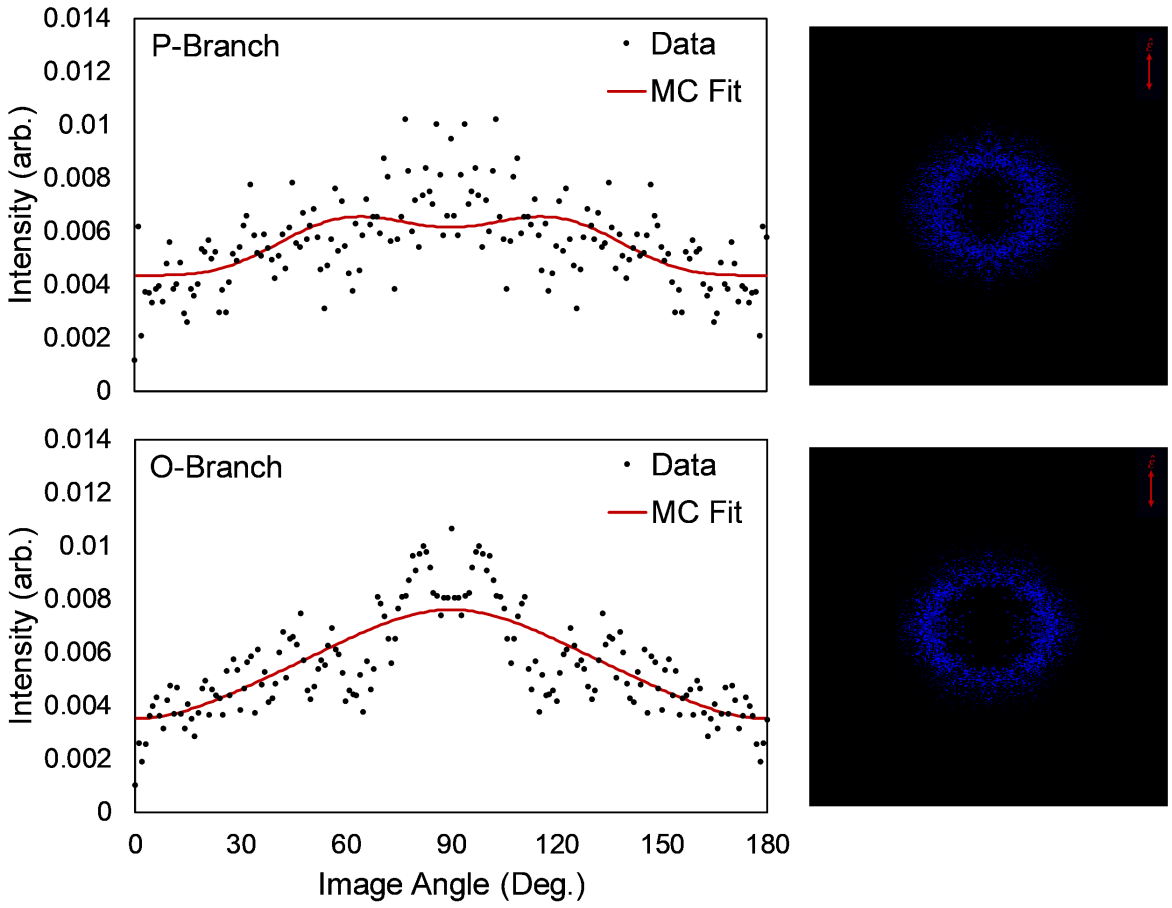

Figure 4.3: Reconstructed HN images at $j = 12$ resulting from the photodissociation of HN_3 at 256 nm. The top panels show the P branch the reconstructed angular distribution with the corresponding reconstructed image shown to the right. The lower panels show the O branch reconstructed angular distriution with the corresponding reconstructed image shown to the right.

The vector properties of the HN_3 dissociation were also measured at each dissociation wave-

length. A series of HN images were collected at three different j_{HN} states were collected at each dissociation wavelengths. A representative set of a reconstructed image pair and their corresponding angular distributions are shown above in Figure 4.3. The top panel shows the j_{HN} = 11 P-branch data while the bottom panel shows the j_{HN} = 11 O-branch data. Since the HN cofragment N_2 is also a polyatomic molecule, the HN images will consist of the average internal energy of the N_2 cofragments. The HN ion images are quite diffuse as a result of the wide distribution of populated j_{N_2} states, ranging from j_{N_2} = 0 up to $j_{HN} \sim 80$ at 256 nm.

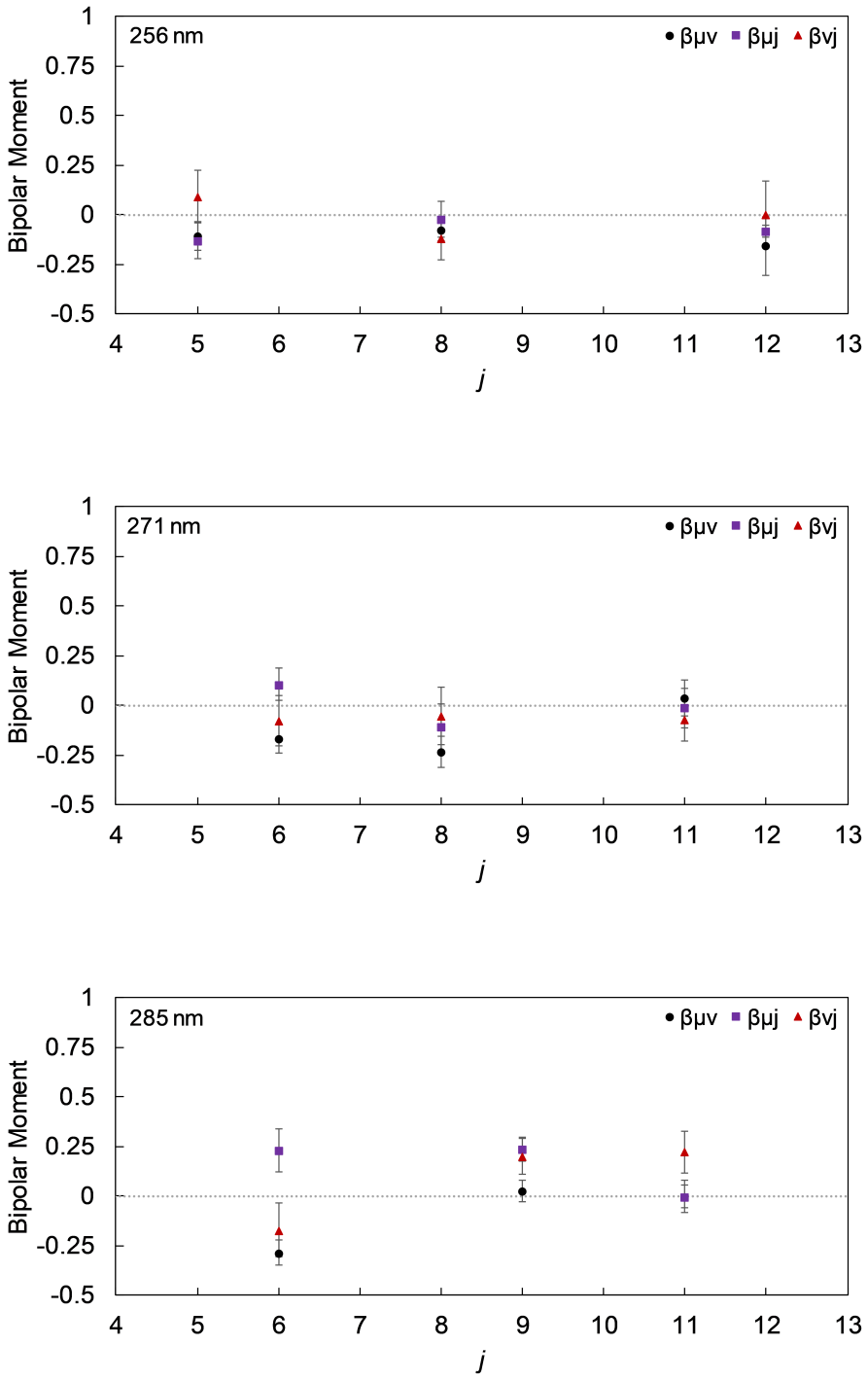

Figure 4.4: $\beta_{\mu v}$, $\beta_{\mu j}$, and β_{vj} shown as black circles, purple squares, and red triangles respectively. The three different photodissociation wavelengths are shown above.

The three lower order bipolar moments $\beta_{\mu v}$,$\beta_{\mu j}$, and β_{vj} at 256 nm, 271 nm, and 285 nm are shown below in Figure 4.4. The distribution at 285 nm indicates an increasing trend for $\beta_{\mu v}$ and β_{vj} , while $\beta_{\mu j}$ remains relatively flat or even slightly decreasing. The general trends at 285 nm compare well to the previously published data at 266 nm and 308 nm, which are shown in Figure 4.6. At the 256 nm and 271 nm, there is no clear trend. This result was unexpected and needs to be remeasured in order to confirm its validity. It is difficult to imagine that dissociation at 256 nm and 271 nm would dissociate via different dynamical pathways compared to 266 nm as the data present in Figure 4.4 suggests. One possibility the vector properties measured at the two dissociation wavelength were unable to be accurately determined possibly due to low S/N. Random noise in the angular distribution data would result in bipolar moments centered around zero similar to the 256 nm and 271 nm data in question. It is also possible the ion image was collected under poor focusing conditions. This could result in a horizontally distorted image rendering the images invalid. In general due to the lack of structure in the HN ion images, it is difficult to finely tune the ion optics. In order to mitigate this problem, the ion optics were regularly tuned both by taking sample ion images to inspect their shape and by refining the parent ion shape into a center dot. For these reasons it seems unlikely the ion optics were the main reason for the poor data quality. Finally it is also possible the imaging were collected under poor image collection setting. Since the dissociation of HN_3 is through a perpendicular transition one would expect the resulting ion images to have some intensity towards the center of the ion images. This is not apparent in several of the ion images. Several ion images with the pulse valve off, where only random noise is present, were collected to investigate this lack of center intensity. Images of random noise should result in isotropic images ion intensity where the majority of the intensity is towards the center of the image. In these tests, the ion images had very weak signal towards the center of these ion images. This could be the result of worn MCPs in the detector where the gain on the MCPs would be low. In order to compensate for this lack of gain, the ion threshold for the image collection setting in Labview was reduced and new test images were collected. By reducing the ion threshold limit, these dimmer ion spots in the center part of the random noise ion images were

also able to be counted. The new set of test images showed strong intensity towards the center of the ion images. It is unclear what effect this reduction in central ion intensity may have on these ion images presented here may have had on the image reconstruction process. It seems unlikely that the reconstruction would have been strongly effected, particularly because the center intensity would likely be dim compared to the peak intensity of the ion images. While the exact cause of the differences between our data and previously published work is unclear, it is possible to determine which images were reasonably fit by the Monte Carlo simulation. From reviewing the data at 256 nm, j_{HN} = 8 is particularly noisy, while j_{HN} = 5 and 12 appear to have good signal to noise. The data at 271 nm is follows a similar trend where the j_{HN} = 6 data is noisy and is not fit well by the Monte Carlo program. While j_{HN} = 9 and 11 have good signal to noise, the Monte Carlo fits to the j_{HN} = 11 P-branch data are not good.

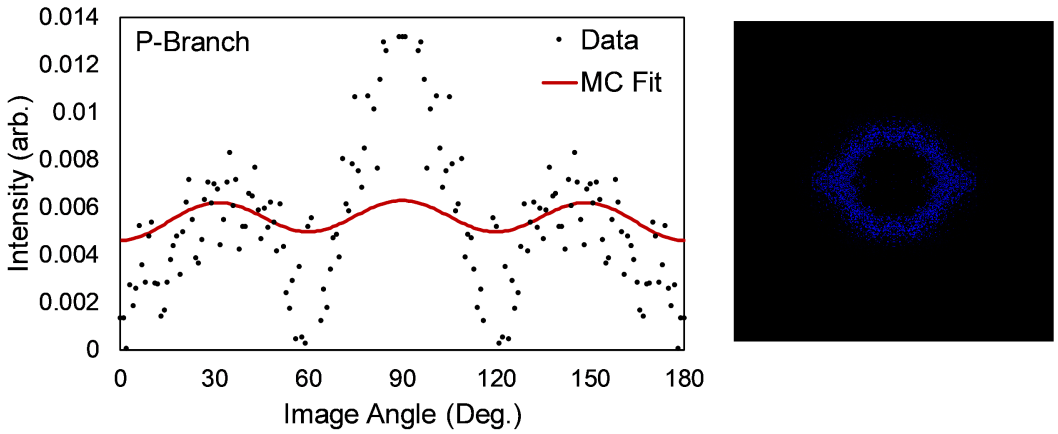

Figure 4.5: The P-branch j_{HN} = 11 reconstructed image is shown to the right. The corresponding reconstructed angular distribution and Monte Carlo fit are shown on the left as black circles and the red line respectively.

The data from the j_{HN} = 11 P branch has a rather unusual shape, shown above in Figure 4.5, that is not well described by the Monte Carlo fit. A new set of data at each of the problematic j_{HN} image pairs mentioned would be able to determine the validity of the currently determined vector properties.

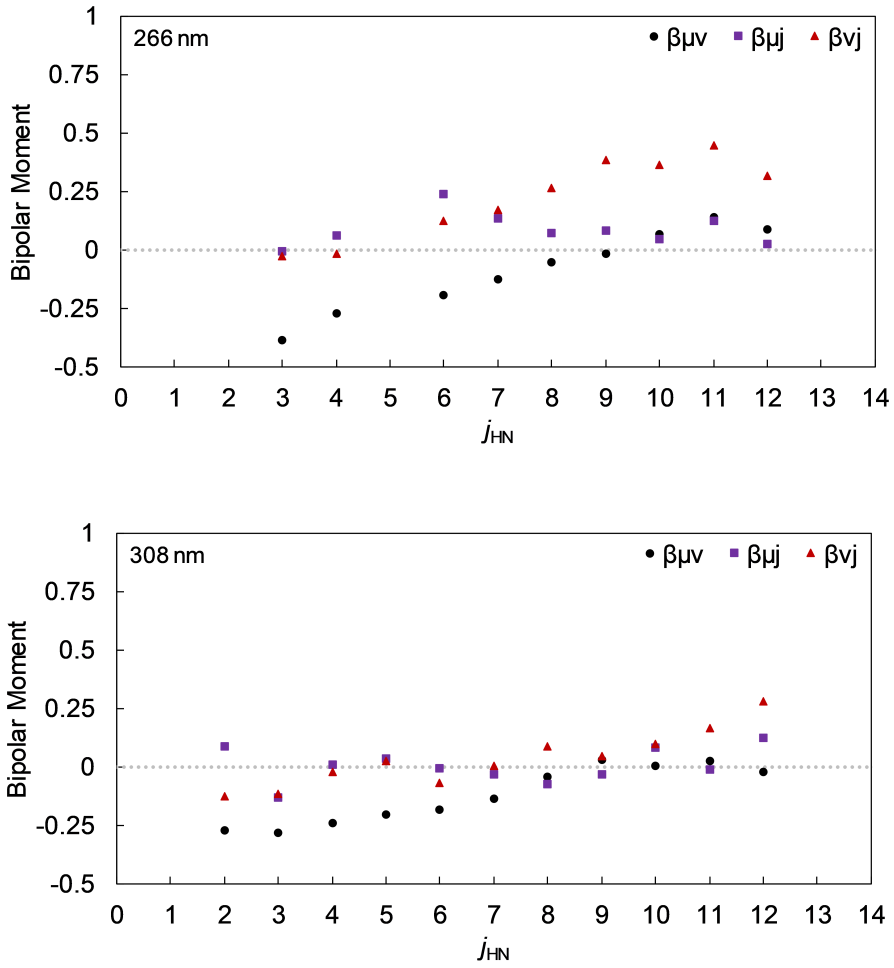

Figure 4.6: $\beta_{\mu v}$, $\beta_{\mu j}$, and β_{vj} shown as black, purple, and red respectively. The bipolar moments were measured at two different dissociation wavelengths 266 nm and 308 nm. Each data set was adapted from Ref. [24] and [26] respectively.

The speed dependent vector correlation at each of the three dissociation wavelengths were also measured, but do to the uncertain nature of the 256 nm and 271 nm data, only the 285 nm data will be analyzed here. Additionally, the 283 nm 2+2 REMPI data from Chu *et al.* can be compared to these speed dependent results to obtain a correlated picture of the dissociation of HN_3 near 285 nm. This correlated picture allows us to understand how the dynamics of each j_{HN} relates to the dynamics of a small range of j_{N_2} states, where the range of $\langle j_{N_2} \rangle$ states is > 2, shown below in Figure 4.7).

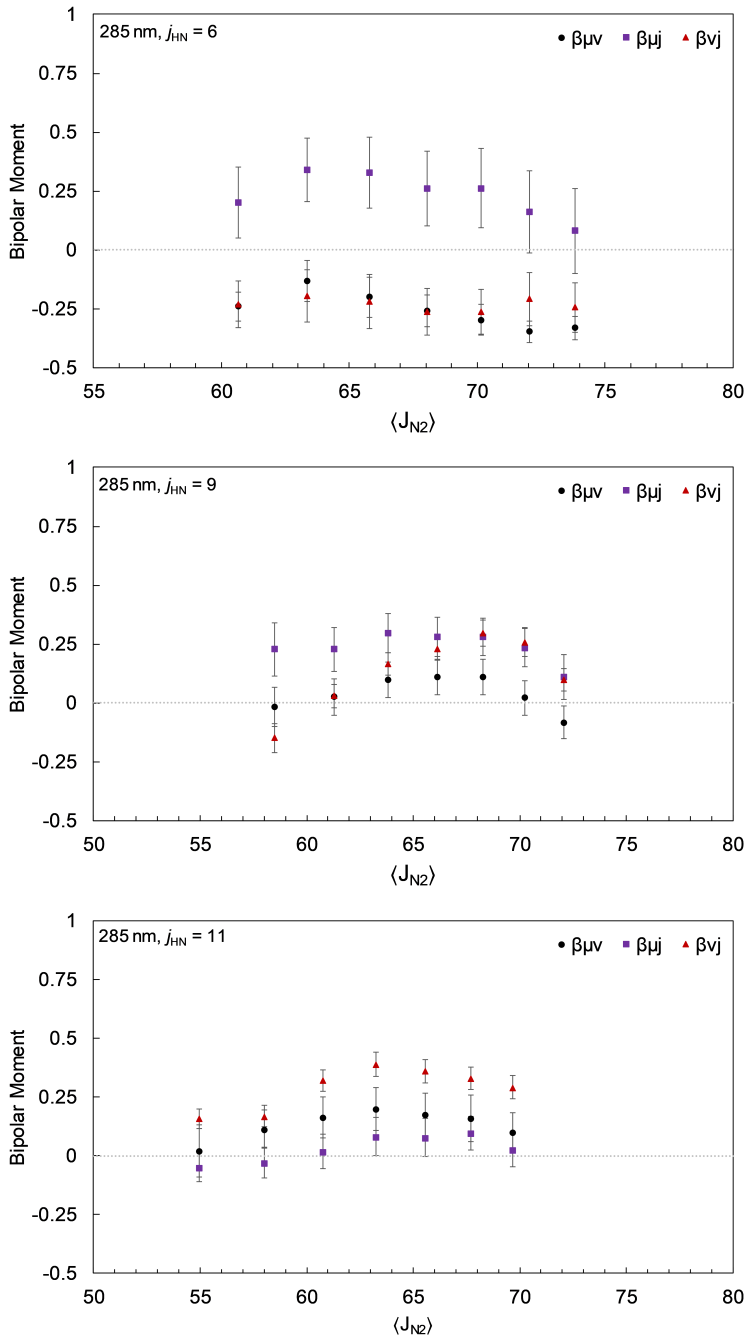

Figure 4.7: Speed dependent $\beta_{\mu v}$, $\beta_{\mu j}$, and β_{vj} shown in black circles, purple squares, and red triangles were calculated from HN ion image resulting from the photodissociation of HN_3 at 285 nm vs the average j_{N_2} rotational state. Each speed dependent bipolar moment is calculated from a 9-pixel wide slice of the total ion image thus the x-axis corresponds to an average j_{N_2} ($\langle j_{N_2} \rangle$). The range of the $\langle j_{N_2} \rangle$ corresponds to approximately > 2 j_{N_2} .

These speed dependent vector correlations can provide some insight into the correlated dynamics of the HN_3 dissociation at 285 nm. There are two vibrational modes to consider when analyzing this data, the ν_5 in plane bending or the ν_6 out of plane torsion of HN_3 on the ground state potential energy surface. From the averaged bipolar moment data presented in Figure 4.4 the higher the final j_{HN} the more excited the ν_6 mode was during the dissociation process. From these speed dependent bipolar moments, the contribution of each vibrational mode to the j_{N_2} rotational distribution can also be determined. In the $j_{HN} = 6$ distribution $\beta_{\mu v}$ and β_{vj} remains relatively flat across each entire distribution where at the lowest $\langle j_{N_2} \rangle$ the $\mu \cdot v$ and $v \cdot j$ are at ~ 65.4 deg and $\sim 64.9°$ while at the highest $\langle j_{N_2} \rangle$ the $\mu \cdot v$ and $v \cdot j$ are at $\sim 70.3°$ and $\sim 65.6°$ respectively. The flatness of $\beta_{\mu v}$ and β_{vj} indicates each j_{N_2} as a function of coincident N_2 state, correlated to $j_{HN} = 6$, are primarily bending in the molecular plane on the ground state of HN_3 via the ν_5 vibrational mode. At $j_{HN} = 6$ there is less contribution from the ν_6 vibrational mode than $j_{HN} = 9$ and 11. This is reflected in the smaller angles between $\mu \cdot v$ and $v \cdot j$. For $j_{HN} = 11$ at the lowest $\langle j_{N_2} \rangle$ the angles between $\mu \cdot v$ and $v \cdot j$ are $\sim 55.4°$ and $\sim 61.1°$ decreasing to $\sim 50.4°$ and $\sim 43.3°$ near the middle of the distribution at $\langle j_{N_2} \rangle$ = 63. In both $j_{HN} = 9$ and 11 the $\beta_{\mu v}$ and β_{vj} values are not only positive, but they also increase with increasing $\langle N_2 \rangle$ eventually falling off over at the highest j_{N_2} states. As the angles between $\mu \dot{v}$ and $v \dot{j}$ decrease, more of the j_{N_2} products are dissociating while bending through the ν_6 torsional motion in the HN_3 ground state.

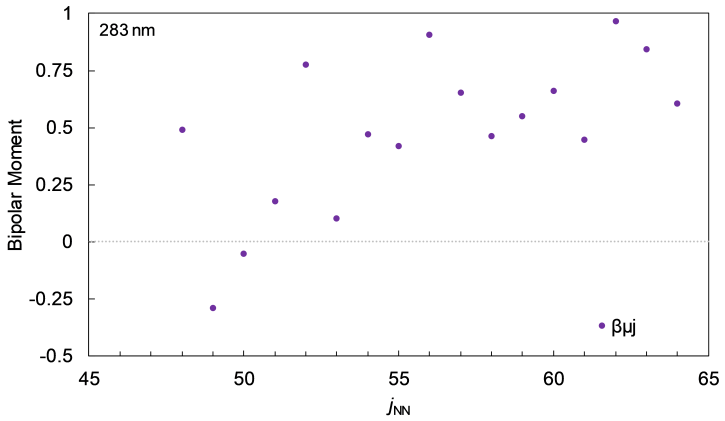

Figure 4.8: The $\beta_{\mu j}$ of the N_2 photofragment resulting from the photodissociation of HN_3 at 283 nm from Chu *et al.* [25].

The directly measured $\beta_{\mu j}$ values originating from the photodissociation of HN_3 at 283 nm are shown above in Figure 4.8. The measured $\beta_{\mu j}$ are very noisy between each j_{N_2} state, but in general the $\beta_{\mu j}$ parameter is increasing with increasing j_{HN} and reaching a plateau between $j_{N_2} = 55$ to $j_{HN} = 60$. This flatter region corresponds to the lowest j_{N_2} values presented in Figure 4.7. The N_2 vector correlations presented here are an average value of all of the coincident NH rotational states. Similar to the average NH vector correlations presented earlier, each j_{N_2} will consist of a unique distribution of NH rotational states. Each data point in Figure 4.8 correlates to a vertical slice in the 285 nm data presented in Figure 4.7. These two regions compare well as they both have the same general shape.

The decreasing trend for all three bipolar moments, in Figure 4.7, at the highest j_{N_2} is currently under investigation. This trend could be explained by noisy data, as mentioned earlier, random noise will result in each of the three bipolar moments trending towards zero. Each data set was visual inspected to ensure the data had a reasonable level of S/N making this explanation unlikely. Both the $\beta_{\mu\nu}$ and $\beta_{\nu j}$ correlations could begin trending towards zero due to the increasing amount of non-axial recoil at at the highest j_{N_2} values, similar to figure 3.7. This however is not the case in since the recoil velocity of the HN fragments is still more than a thousand m/s at these high j_{N_2} values. Perhaps the simplest explanation is that the highest j_{N_2} states are increasingly dissociated via

the ν_5 in plane bend. Dynamically it is possible that the ν_6 bending motion plateaus where it has an upper limiting on how much torsional motion the molecule can undergo before the HN_3 molecule experiences a restoring force and bends back into the plane. This could indicate a ν_6 bending potential that is rather wide at the minimum which rapidly increases at larger angles, however the *ab initio* calculations by Meier *et al.* indicate the in-plane and out-of-plane NNN bending potential are nearly identical.[93] Additional the calculated potentials for the NNH bend show similar well depths and restoring forces to the two NNN bending potentials. These surfaces were calculated at a single interior NN bond length which will be changing during the dissociation process. It is possible the lengthening of this bond will effect each of the bending potentials differently. Two different types of averaging techniques are being applied to the data to help confirm these trends. First wider slices of the ion image are being considered using 15 and 20 pixel slices as opposed to the original 9 pixel slice. By taking wider slices the resulting angular distributions will be less noisy. Secondly a moving average is being applied to the current 9 pixel angular distributions to increase the S/N by a factor of 2. This additional increase in the S/N will help to valid these trends.

4.3 Conclusion

Ion images of HN resulting from the photodissociation of HN_3 at three different dissociation wavelengths were measured. The HN rotational distributions at 256 nm, 271 nm, and 285 nm were measured and compared to rotational distributions found in the literature. The HN rotational distribution has been reported to be invariant with dissociation wavelength. The rotational distributions at each dissociation wavelength measured here and from the literature were fit with Boltzmann distributions and were shown to have similar temperatures confirming the HN rotational distributions are invariant with dissociation wavelength. The average HN bipolar moments at each dissociation wavelength are also reported. The data resulting from 256 nm and 271 nm did not agree well with previously reported bipolar moments at similar dissociation wavelengths. Several possible reasons including poor ion focusing conditions, low intensity ion center signal, or simply due to low quality images. The 285 nm data did agree well with previously reported bipolar moments which show increasing $\beta_{\mu v}$ and β_{vj} across the j_{HN} distribution with little change in $\beta_{\mu j}$ across the j_{HN} distribu-

tion. The first reported speed dependent vector correlations for the photodissociation of HN_3 were corresponding to the dissociation of HN_3 at 285 nm were presented. Low j_{N_2} associated with low j_{HN} corresponds to dissociation primarily by the ν_5 in plane bend of the HN_3 molecule, where j_{N_2} associated with high j_{HN} has been shown to have an increasing dependence on the ν_6 out of plane bend. The highest j_{N_2} associated with the highest j_{HN} have shown an interesting decrease in the speed dependent bipolar moments. This phenomena has not yet been satisfactorily explained, but it is possible that there is an increased dependence on the ν_6 bending mode. This data is still under investigation.

5. SUMMARY AND CONCLUSIONS

In this dissertation the photodissociation of OCS was measured at 214 nm revealing previously undetected CO($v = 1$). The origin of the CO($v = 1$) has not been determined, but more recent studies by Bai *et al.* at shorter wavelengths have also measured a similar vibrational branching ratio.[49] The $\beta_{\mu v}$ and $\beta_{\mu j}$ parameters were used to confirm the two electronic state model. Using a three-Gaussian model the relative contributions from the A, B, and X states to the photodissociation of OCS were determined. The contribution from the B state at 214 nm for the CO($v = 1$) and CO($v = 0$) channels were $\sim$ 2.5 times smaller ($f_B = 0.14 \pm 0.04$) and $\sim$ 1.7 times smaller ($f_B = 0.20 \pm 0.04$) than predicted. This three-Gaussian model was extended to experimental measurements from the photodissociation of OCS at 223 nm, 230 nm, and 248 nm found in the literature. The contribution of the B state (f_B) did not agree well with theory over the first absorption band. Additionally, experimental measurements at 214 nm have indicated an underestimation in the surface hopping trajectories in the photodissociation of OCS, possibly originating from discrepancies in the calculated initial impulse along the bending coordinate or the coupling between the ground X($1^1A'$) and A($2^1A'$). The photodissociation of HN_3 has been measured in the first UV absorption band near 256 nm, 271 nm, and 285 nm were measured using VELMI. The rotational distributions at each dissociation wavelength were in good agreement with previous measurements in the literature. A series of images across the HN rotational distribution were collected at each wavelength. The experimental measurements at 285 nm are in good agreement with previous measurements in the literature, while the results at 256 nm and 271 nm were likely effected by random noise. Speed dependent vector correlations were successfully measured using the recently developed 2+1 equations. The speed dependent vector correlations measured from the HN fragment provided insight into the correlated dynamics of the N_2 cofragment. The speed dependent vector correlations at 285 nm indicated the low j_{N_2} originated primarily from the ν_5 in plane bend and with increasing dependence on the ν_6 torsion with increasing j_{N_2} . In the future, additional measurements of the N_2 fragment using a 2+2 REMPI scheme at 283 nm are possible. Ion images

of the N_2 fragment would allow for the direct determination of the N_2 vector properties providing a way to validate the speed dependent vector correlations measured using the 2+1 HN REMPI scheme at 285 nm. Additional measurements at 256 nm and 271 nm are necessary to determine the accuracy of the vector correlations presented here.

The photodissociation of acetaldehyde and ketene is discussed in the appendix of the dissertation. Both of these experiments were limited by a persistent nonresonant, pulse valve dependent signal at m/z = 28. The origin of this signal was attributed to the short wavelengths used in the CO(E-X) 2+1 REMPI transition near 214 nm. Any future attempts to detect CO from the photodissociation of acetaldehyde or ketene would require a different probing scheme that would avoid the 214 nm region. Possible schemes include using a 2+2 or 2+1′ REMPI process through the A state of CO. In order to use a 2+1′ REMPI scheme in the A state, it is necessary to excite to at least the CO(v=7) state in the A state. At these energies it would is theoretically possible to use a single 266 nm photon to ionize the excited CO fragment. Since the A state is a valence state, as opposed to the Rydberg states (B and E states) previously used, it is necessary to carefully consider the Franck-Condon factor between the ground X and excited A states of CO. The Franck-Condon factor between the CO(X,v=0) and CO(A,v=7) states has been roughly calculated to be ~0.03 using the diatomic constants in the NIST webbook.[20]

REFERENCES

[1] R. Schinke, Photodissociation Dynamics, Cambridge, 1994.

[2] G. C. McBane, J. A. Schmidt, M. S. Johnson, R. Schinke, Ultraviolet photodissociation of OCS: product energy and angular distributions, Journal of Chemical Physics 138 (9) (2013) 094314. doi:10.1063/1.4793275.

[3] C. J. Wallace, C. E. Gunthardt, G. C. McBane, S. W. North, Empirical assignment of absorbing electronic state contributions to OCS photodissociation product state populations from 214 to 248 nm, Chemical Physics 520 (2019) 1.

[4] J. A. Schmidt, M. S. Johnson, G. C. McBane, R. Schinke, The ultraviolet spectrum of OCS from first principles: electronic transitions, vibrational structure and temperature dependence, Journal of Chemical Physics 137 (5) (2012) 054313. doi:10.1063/1.4739756.

[5] T. Suzuki, H. Katayanagi, S. Nanbu, M. Aoyagi, Nonadiabatic bending dissociation in 16 valence electron system OCS, Journal of Chemical Physics 109 (14) (1998) 5778. doi:10.1063/1.477200.

[6] N. Sivakumar, G. E. Hall, P. L. Houston, J. W. Hepburn, I. Burak, Stateresolved photodissociation of OCS monomers and clusters, Journal of Chemical Physics 88 (6) (1988) 3692. doi:10.1063/1.453869.

[7] A. J. van den Brom, T. P. Rakitzis, J. van Heyst, T. N. Kitsopoulos, S. R. Jezowski, M. H. M. Janssen, State-to-state photodissociation of OCS($v_2 = 0, 1|JlM$). i. the angular recoil distribution of CO($x^1\Sigma^+;v = 0|J$), Journal of Chemical Physics 117 (9) (2002) 4255. doi:10.1063/1.1496464.

[8] M. Brouard, A. V. Green, F. Quadrini, C. Vallance, Photodissociation dynamics of OCS at 248 nm: The S($^1D_2$) atomic angular momentum polarization, Journal of Chemical Physics 127 (8) (2007) 084304. doi:10.1063/1.2757618.

[9] G. C. McBane, private communication.

[10] J. McDonald, J. Rabalais, S. McGlynn, Electronic spectra of the azide ion, hydrazoic acid, and azido molecules, The Journal of Chemical Physics 52 (3) (1970) 1332.

[11] F. Rohrer, F. Stuhl, The 193 (and 248) nm photolysis of HN_3: Formation and internal energy distributions of the NH($a^1\Delta, b^1\Sigma^+, A^3\Pi$, and $c^1\Pi$) states, The Journal of Chemical Physics 88 (8) (1988) 4788.

[12] J. J. Orlando, G. S. Tyndall, E. A. Betterton, J. Lowry, S. T. Stegall, Atmospheric chemistry of hydrazoic acid (HN_3): UV absorption spectrum, HO· reaction rate, and reactions of the $\cdot N_3$ radical, Environmental Science & Technology 39 (6) (2005) 1632. doi:10.1021/es048178z.

[13] M. Hawley, A. P. Baronavski, H. H. Nelson, Vibrational distributions of NH ($a^1\delta$) from the photolysis of HN_3 from 220290 nm, The Journal of Chemical Physics 99 (4) (1993) 2638. doi:10.1063/1.465226.

[14] R. N. Dixon, The determination of the vector correlation between photofragment rotational and translational motions from the analysis of Doppler-broadened spectral line profiles, Journal of Chemical Physics 85 (4) (1986) 1866. doi:10.1063/1.451131.

[15] J. Kemp, W. Giauque, Carbonyl sulfide. the heat capacity, vapor pressure, and heats of fusion and vaporization. the third law of thermodynamics and orientation equilibrium in the solid, Journal of the American Chemical Society 59 (1) (1937) 79.

[16] C. Y. Robert Wu, F. Z. Chen, D. L. Judge, Temperature-dependent photoabsorption cross sections of OCS in the 2000–2600 region, Journal of Quantitative Spectroscopy and Radiative Transfer 61 (2) (1999) 265. doi:https://doi.org/10.1016/S0022-4073(97)00220-3.

[17] R. D. Johnson III, J. W. Hudgens, New electronic states of NH and ND observed from 258 to 288 nm by resonance enhanced multiphoton ionization spectroscopy, The Journal of Chemical Physics 92 (11) (1990) 6420.

[18] R. D. Johnson III, J. W. Hudgens, New electronic states of NH and ND observed from 258 to 288 nm by resonance enhanced multiphoton ionization spectroscopy, supplementary material, The Journal of Chemical Physics 92 (11) (1990) 6420.

[19] E. de Beer, M. Born, C. A. de Lange, N. P. C. Westwood, A rotationally resolved REMPI-PES study of the NH radical, Chemical Physics Letters 186 (1) (1991) 40. doi:https://doi.org/10.1016/0009-2614(91)80189-5.

[20] K. P. Huber, G. H. Herzberg, Constants of Diatomic Molecules, NIST Chemistry WebBook, National Institute of Standards and Technology, 2019. doi:https://doi.org/10.18434/T4D303.

[21] C. E. Gunthardt, C. J. Wallace, G. E. Hall, R. W. Field, S. W. North, Anomalous intensities in the 2+1 REMPI spectrum of the $e^1\pi$-$x^1\sigma^+$ transition of CO, The Journal of Physical Chemistry A (2019) 2780.

[22] W. Wei, C. J. Wallace, G. C. McBane, S. W. North, Photodissociation dynamics of OCS near 214 nm, Journal of Chemical Physics 145 (2016) 024310.

[23] A. V. Komissarov, M. P. Minitti, A. G. Suits, G. E. Hall, Correlated product distributions from ketene dissociation measured by dc sliced ion imaging, The Journal of chemical physics 124 (1) (2006) 014303.

[24] K. H. Gericke, R. Theinl, F. J. Comes, Photofragment energy distribution and rotational anisotropy from excitation of HN_3 at 266 nm, Chemical Physics Letters 164 (6) (1989) 605. doi:https://doi.org/10.1016/0009-2614(89)85267-4.

[25] J. Chu, P. Marcus, P. J. Dagdigian, Onecolor photolysisionization study of HN_3: The N_2 fragment internal energy distribution and $\mu - v - j$ correlations, The Journal of Chemical Physics 93 (1) (1990) 257. doi:10.1063/1.459598.

[26] K. H. Gericke, R. Theinl, F. J. Comes, Vector correlations in the photofragmentation of HN_3, The Journal of Chemical Physics 92 (11) (1990) 6548. doi:10.1063/1.458290.

[27] K. L. K. Lee, M. S. Quinn, A. T. Maccarone, K. Nauta, P. L. Houston, S. A. Reid, M. J. Jordan, S. H. Kable, Two roaming pathways in the photolysis of CH_3CHO between 328 and 308 nm, Chemical Science 5 (12) (2014) 4633.

[28] H.-G. Libuda, Spektroskopische und kinetische untersuchungen an halogenierten carbonylverbindungen von atmosphärischem interesse, Ph.D. thesis, Verlag nicht ermittelbar (1992).

[29] A. H. Laufer, R. A. Keller, Lowest excited states of ketene, Journal of the American Chemical Society 93 (1) (1971) 61.

[30] M. P. Docker, Photofragment vector correlations measured by sub-doppler 2+1 laser-induced fluorescence spectroscopy, Chemical Physics 135 (3) (1989) 405. doi:https://doi.org/10.1016/0301-0104(89)80117-X.

[31] S. G. Clement, M. N. Ashfold, C. M. Western, Resonance-enhanced multiphoton ionisation spectroscopy of the NH (ND) radical. part 2. singlet members of the 3p rydberg complex, J. CHEM. SOC. FARADAY TRANS. 88 (21) (1992) 3121.

[32] W. Wei, Vector correlation and their applications in photodissociation dyanmics study, dissertation, Texas A&M (2017).

[33] P. J. Crutzen, The possible importance of CSO for the sulfate layer of the stratosphere, Geophysical Research Letters 3 (2) (1976) 73. doi:doi:10.1029/GL003i002p00073.

[34] M. Chin, D. D. Davis, A reanalysis of carbonyl sulfide as a source of stratospheric background sulfur aerosol, Journal of Geophysical Research: Atmospheres 100 (D5) (1995) 8993. doi:doi:10.1029/95JD00275.

[35] J. Notholt, Z. Kuang, C. P. Rinsland, G. C. Toon, M. Rex, N. Jones, T. Albrecht, H. Deckelmann, J. Krieg, C. Weinzierl, H. Bingemer, R. Weller, O. Schrems, Enhanced upper tropical tropospheric COS: Impact on the stratospheric aerosol layer, Science 300 (5617) (2003) 307. doi:10.1126/science.1080320.

[36] P. L. Hanst, L. L. Spiller, D. M. Watts, J. W. Spence, M. F. Miller, Infrared measurement of fluorocarbons, carbon tetrachloride, carbonyl sulfide, and other atmospheric trace gases, Journal of the Air Pollution Control Association 25 (12) (1975) 1220. doi:10.1080/00022470.1975.10470199.

[37] S. A. Montzka, P. Calvert, B. D. Hall, J. W. Elkins, T. J. Conway, P. P. Tans, C. Sweeney, On the global distribution, seasonality, and budget of atmospheric carbonyl sulfide (COS) and some similarities to co_2, Journal of Geophysical Research: Atmospheres 112 (D9) (2007). doi:10.1029/2006JD007665.

[38] C. Brühl, J. Lelieveld, P. J. Crutzen, H. Tost, The role of carbonyl sulphide as a source of stratospheric sulphate aerosol and its impact on climate, Atmospheric Chemistry and Physics 12 (2012) 1239. doi:https://doi.org/10.5194/acp-12-1239-2012.

[39] W. Lochte-Holtgreven, C. Bawn, The heat of formation and structure of the carbon-oxygen and carbon-sulphur linkages, Transactions of the Faraday Society 28 (2012) 698. doi:https://doi.org/10.5194/acp-12-1239-2012.

[40] G. Nan, I. Burak, P. L. Houston, Photodissociation of OCS at 222 nm. The triplet channel, Chemical Physics Letters 209 (4) (1993) 383. doi:https://doi.org/10.1016/0009-2614(93)80035-N.

[41] G. S. Forbes, J. E. Cline, The photolysis and extinction coefficients of gaseous carbonyl sulfide, Journal of the American Chemical Society 61 (1) (1939) 151.

[42] L. T. Molina, J. J. Lamb, M. J. Molina, Temperature dependent UV absorption cross sections for carbonyl sulfide, Geophysical Research Letters 8 (9) (1981) 1008. doi:doi:10.1029/GL008i009p01008.

[43] Y. Mo, H. Katayanagi, M. C. Heaven, T. Suzuki, Simultaneous measurement of recoil velocity and alignment of S($^1D_2$) atoms in photodissociation of OCS, Physical Review Letters 77 (5) (1996) 830.

[44] A. M. Rijs, E. H. G. Backus, C. A. de Lange, M. H. M. Janssen, N. P. C. Westwood, K. Wang, V. McKoy, Rotationally resolved photoionization dynamics of hot CO fragmented from OCS, Journal of Chemical Physics 116 (7) (2002) 2776. doi:doi:http://dx.doi.org/10.1063/1.1434993.

[45] M. H. Kim, W. Li, S. K. Lee, A. G. Suits, Probing of the hot-band excitations in the photodissociation of OCS at 288 nm by DC slice imaging, Canadian Journal of Chemistry 82 (6) (2004) 880. doi:10.1139/v04-072.

[46] S. K. Lee, R. Silva, S. Thamanna, O. S. Vasyutinskii, A. G. Suits, S($^1D_2$) atomic orbital polarization in the photodissociation of OCS at 193 nm: Construction of the complete density matrix, Journal of Chemical Physics 125 (14) (2006) 144318. doi:doi:http://dx.doi.org/10.1063/1.2357948.

[47] M. L. Lipciuc, T. P. Rakitzis, W. L. Meerts, G. C. Groenenboom, M. H. Janssen, Towards the complete experiment: measurement of (S^1D_2) polarization in correlation with single rotational states of CO(J) from the photodissociation of oriented $OCS(\nu_2 = 1|JlM = 111)$, Physical Chemistry Chemical Physics 13 (18) (2011) 8549. doi:10.1039/c0cp02671a.

[48] A. Sugita, M. Mashino, M. Kawasaki, Y. Matsumi, R. Bersohn, G. Trott-Kriegeskorte, K.-H. Gericke, Effect of molecular bending on the photodissociation of OCS, The Journal of Chemical Physics 112 (16) (2000) 7095. doi:10.1063/1.481324.

[49] X. Bai, H. Liang, Z. Zhou, Z. Hua, D. Zhao, Y. Chen, Photodissociation dynamics of OCS at 217 nm, Chinese Journal of Chemical Physics 30 (5) (2017) 499. doi:10.1063/1674-0068/30/cjcp1705092.

[50] Y. Sato, Y. Matsumi, M. Kawasaki, K. Tsukiyama, R. Bersohn, Ion imaging of the photodissociation of OCS near 217 and 230 nm, Journal of Physical Chemistry 99 (44) (1995) 16307. doi:10.1021/j100044a017.

[51] S. O. Danielache, S. Nanbu, C. Eskebjerg, M. S. Johnson, N. Yoshida, Carbonyl sulfide isotopologues: Ultraviolet absorption cross sections and stratospheric photolysis, Journal of

Chemical Physics 131 (2) (2009) 024307. doi:10.1063/1.3156314.

[52] J. A. Schmidt, M. S. Johnson, G. C. McBane, R. Schinke, Communication: Multi-state analysis of the OCS ultraviolet absorption including vibrational structure, Journal of Chemical Physics 136 (13) (2012) 131101. doi:10.1063/1.3701699.

[53] E. A. Betterton, Environmental fate of sodium azide derived from automobile airbags, Critical Reviews in Environmental Science and Technology 33 (4) (2003) 423. doi:10.1080/10643380390245002.

[54] H. Okabe, Photodissociation of hn_3 in the vacuumultraviolet production and reactivity of electronically excited NH, The Journal of Chemical Physics 49 (6) (1968) 2726. doi:10.1063/1.1670477.

[55] K. H. Welge, Formation of $N_2(A^3\Sigma_\mu^+)$ and N(^{2}D, ^{2}P) by photodissociation of HN_3 and N_2O and their reactions with NO and N_2O, The Journal of Chemical Physics 45 (1) (1966) 166. doi:10.1063/1.1727302.

[56] K. H. Welge, Formation of NH($c^1\Pi$) and NH($A^3\Pi_i$) in the vacuum-UV photolysis of HN_3, The Journal of Chemical Physics 45 (11) (1966) 4373.

[57] K.-H. Gericke, M. Lock, F. J. Comes, Photodissociation of HN_3: direct formation of hydrogen atoms, Chemical Physics Letters 186 (4) (1991) 427. doi:https://doi.org/10.1016/0009-2614(91)90203-L.

[58] M. Lock, K.-H. Gericke, F. J. Comes, Photodissociation dynamics of $HN_3(DN_3) + h\nu \rightarrow$ H(D)+ N_3, Chemical Physics 213 (1) (1996) 385. doi:https://doi.org/10.1016/S0301-0104(96)00239-X.

[59] J. C. Stephenson, M. P. Casassa, D. S. King, Energetics and spin- and Λ-doublet selectivity in the infrared multiphoton dissociation DN_3 DN $(X^3\Sigma^-, a^1\Delta) + N_2(X^1\Sigma_g^+)$: Experiment, The Journal of Chemical Physics 89 (3) (1988) 1378.

[60] B. Foy, M. Casassa, J. Stephenson, D. King, Overtone-excited HN_3 ($\tilde{X}^1A'$): Anharmonic resonance, homogeneous linewidths, and dissociation rates, The Journal of Chemical Physics 92 (5) (1990) 2782.

[61] B. R. L. Galvão, A. J. C. Varandas, Accurate study of the two lowest singlet states of HN_3: Stationary structures and energetics at the MRCI complete basis set limit, The Journal of Physical Chemistry A 117 (19) (2013) 4044. doi:10.1021/jp402090s.

[62] B. M. Dekoven, A. P. Baronavski, Photofragment spectroscopy of HN_3 cooled in a supersonic beam, Chemical Physics Letters 86 (4) (1982) 392. doi:https://doi.org/10.1016/0009-2614(82)83530-6.

[63] K. Gericke, M. Lock, R. Fasold, F. J. Comes, Influence of the electronic asymmetry in NH ($^1\delta$) state λ doublets on the photodissociation dynamics of HN_3 and DN_3, The Journal of Chemical Physics 96 (1) (1992) 422. doi:10.1063/1.462477.

[64] K. L. Carleton, K. H. Welge, S. R. Leone, Detection of nitrogen rotational distributions by resonant 2+ 2 multiphoton ionization through the $a^1\pi_g$ state, Chemical physics letters 115 (6) (1985) 492.

[65] K. H. Gericke, T. Haas, M. Lock, R. Theinl, F. J. Comes, Hydrazoic acid(A^1A'') hypersurface at excitation energies of 4.0-5.0 eV, The Journal of Physical Chemistry 95 (16) (1991) 6104. doi:10.1021/j100169a013.

[66] H. H. Nelson, J. R. McDonald, Energy partitioning in the 266 nm dissociation of HN_3 and relative transition probabilities in the NH ($c^1\pi \leftrightarrow a^1\delta$) system, The Journal of Chemical Physics 93 (12) (1990) 8777. doi:10.1063/1.459266.

[67] D. Townsend, M. P. Minitti, A. G. Suits, Direct current slice imaging, Review of scientific instruments 74 (4) (2003) 2530.

[68] A. T. Eppink, D. H. Parker, Velocity map imaging of ions and electrons using electrostatic lenses: Application in photoelectron and photofragment ion imaging of molecular oxygen, Review of Scientific Instruments 68 (9) (1997) 3477.

[69] H. Keller-Rudek, G. Moortgat, R. Sander, R. Sörensen, The MPI-Mainz UV/VIS spectral atlas of gaseous molecules of atmospheric interest, Earth System Science Data 5 (2) (2013) 365–373.

[70] Gaussian beam optics [online].

[71] M. A. Hines, H. A. Michelsen, R. N. Zare, 2+1 resonantly enhanced multiphoton ionization of CO via the $e^1\pi - x^1\sigma^+$ transition: From measured ion signals to quantitative population distributions, The Journal of Chemical Physics 93 (12) (1990) 8557.

[72] M. A. Hines, The interaction of CO with Ni(111): Inelastic scattering and trapping/desorption, Dissertation, Stanford University (1992).

[73] Y. Pak, R. C. Woods, Spectroscopic constants and potential energy functions of $OCCl^+$, ONP, ONS^+, $ArCN^+$, OCS, and NCCl using the coupled cluster method, The Journal of chemical physics 107 (13) (1997) 5094.

[74] S. Abbi, S. Ahmad, Nonlinear Optics and Laser Spectroscopy, Alpha Science Int'l Ltd., 2001.

[75] M. P. Grubb, Roaming in the dark: Deciphering the mystery of the $NO_3 \rightarrow NO + O_2$ photolysis, dissertation, Texas A&M (2012).

[76] G. Roberts, J. Nixon, J. Lecointre, E. Wrede, J. Verlet, Toward real-time charged-particle image reconstruction using polar onion-peeling, Review of Scientific Instruments 80 (5) (2009) 053104.

[77] M. P. Grubb, M. L. Warter, C. D. Freeman, N. A. West, K. M. Usakoski, K. M. Johnson, J. A. Bartz, S. W. North, A method for the determination of speed-dependent semi-classical vector correlations from sliced image anisotropies, Journal of Chemical Physics 135 (9) (2011) 094201. doi:10.1063/1.3631343.

[78] R. N. Zare, D. R. Herschbach, Doppler line shape of atomic fluorescence excited by molecular photodissociation, Proceedings of the IEEE 51 (1) (1963) 173.

[79] G. Hall, P. Houston, Vector correlations in photodissociation dynamics, Annual Review of Physical Chemistry 40 (1) (1989) 375.

[80] T. P. Rakitzis, Direct measurement of photofragment alignment from unnormalized Abel-invertible images, Chemical physics letters 342 (1-2) (2001) 121–126.

[81] M. P. Grubb, M. L. Warter, C. Daniel Freeman, N. A. West, K. M. Usakoski, K. M. Johnson, J. A. Bartz, S. W. North, Erratum:a method for the determination of speed-dependent semi-classical vector correlations from sliced image anisotropies[j. chem. phys. 135, 094201 (2011)], The Journal of Chemical Physics 136 (21) (2012) 219901.

[82] W. Wei, C. J. Wallace, M. P. Grubb, S. W. North, A method of extracting speed-dependent vector correlations from 2+1 REMPI ion images, Journal of Chemical Physics 147 (2017) 013947.

[83] G. Black, L. Jusinski, Rate coefficients for $S(^1D)$ removal at 300 K, The Journal of chemical physics 82 (2) (1985) 789.

[84] J. Steadman, T. Baer, The production and spectroscopy of excited sulfur atoms from the two-photon dissociation of H_2S, The Journal of chemical physics 89 (9) (1988) 5507.

[85] J. C. Tully, Molecular dynamics with electronic transitions, Journal of Chemical Physics 93 (2) (1990) 1061.

[86] J. A. Schmidt, private communication.

[87] R. G. Bray, R. M. Hochstrasser, Two-photon absorption by rotating diatomic molecules, Molecular Physics 31 (4) (1976) 1199. doi:10.1080/00268977600100931.

[88] A. Le Floch, Accurate energy levels for the C $^1\Sigma^+(v = 0)$ and E $^1\Pi(v = 0)$ states of $^{12}C^{16}O$, Journal of Molecular Spectroscopy 155 (1) (1992) 177. doi:https://doi.org/10.1016/0022-2852(92)90557-5.

[89] Z.-W. Qu, H. Zhu, S. Y. Grebenshchikov, R. Schinke, The triplet channel in the photodissociation of ozone in the Hartley band: Classical trajectory surface hopping analysis, Journal of Chemical Physics 122 (19) (2005) 191102.

[90] G. C. McBane, L. T. Nguyen, R. Schinke, Photodissociation of ozone in the Hartley band: Product state and angular distributions, Journal of Chemical Physics 133 (14) (2010) 144312. doi:10.1063/1.3491813.

[91] J. A. Schmidt, J. M. Olsen, Photodissociation of OCS: deviations between theory and experiment, and the importance of higher order correlation effects, Journal of Chemical Physics 141 (18) (2014) 184310. doi:10.1063/1.4901426.

[92] A. V. Demyanenko, V. Dribinski, H. Reisler, H. Meyer, C. X. W. Qian, Product quantum-state-dependent anisotropies in photoinitiated unimolecular decomposition, Journal of Chemical Physics 111 (16) (1999) 7383. doi:10.1063/1.480061.

[93] U. Meier, V. Staemmler, CASSCF and CEPA calculations for the photodissociation of HN_3. II, Photodissociation into N_2 and NH on the lowest ^1A surface of HN_3, Journal of Physical Chemistry 95 (16) (1991) 6111.

[94] J. I. Steinfeld, J. S. Francisco, W. L. Hase, Chemical kinetics and dynamics, Vol. 3, Prentice Hall Englewood Cliffs (New Jersey), 1989.

[95] D. Townsend, S. A. Lahankar, S. K. Lee, S. D. Chambreau, A. G. Suits, X. Zhang, J. Rheinecker, L. Harding, J. M. Bowman, The roaming atom: straying from the reaction path in formaldehyde decomposition, Science 306 (5699) (2004) 1158.

[96] P. Houston, S. Kable, Photodissociation of acetaldehyde as a second example of the roaming mechanism, Proceedings of the National Academy of Sciences 103 (44) (2006) 16079.

[97] B. R. Heazlewood, M. J. Jordan, S. H. Kable, T. M. Selby, D. L. Osborn, B. C. Shepler, B. J. Braams, J. M. Bowman, Roaming is the dominant mechanism for molecular products in acetaldehyde photodissociation, Proceedings of the National Academy of Sciences 105 (35) (2008) 12719.

[98] B. Friedrich, D. P. Pullman, D. R. Herschbach, Alignment and orientation of rotationally cool molecules, The Journal of Physical Chemistry 95 (21) (1991) 8118.

[99] A. J. Orr-Ewing, R. N. Zare, Orientation and alignment of reaction products, Annual Review of Physical Chemistry 45 (1) (1994) 315.

[100] K. Coles, F. Popper, Vapor-liquid equilibria. ethylene oxide-acetaldehyde and ethylene oxide-water systems, Industrial & Engineering Chemistry 42 (7) (1950) 1434.

[101] S. H. Kable, private communication.

[102] J. W. Hudgens, T. DiGiuseppe, M.-C. Lin, Two photon resonance enhanced multiphoton ionization spectroscopy and state assignments of the methyl radical, The Journal of Chemical Physics 79 (2) (1983) 571.

[103] I.-C. Chen, W. H. Green Jr, C. B. Moore, Bond breaking without barriers: Photofragmentation of ketene at the singlet threshold, The Journal of chemical physics 89 (1) (1988) 314.

[104] S. J. Klippenstein, R. Marcus, Application of unimolecular reaction rate theory for highly flexible transition states to the dissociation of CH_2CO into CH_2 and CO, The Journal of chemical physics 91 (4) (1989) 2280.

[105] W. H. Green Jr, C. B. Moore, W. F. Polik, Transition states and rate constants for unimolecular reactions, Annual Review of Physical Chemistry 43 (1) (1992) 591.

[106] S. J. Klippenstein, A. L. East, W. D. Allen, A high level ab initio map and direct statistical treatment of the fragmentation of singlet ketene, The Journal of chemical physics 105 (1) (1996) 118.

[107] C. G. Morgan, M. Drabbels, A. M. Wodtke, The correlated product state distribution of ketene photodissociation at 308 nm, The Journal of chemical physics 104 (19) (1996) 7460.

[108] B. G. Reuben, Vapor pressure of ketene, Journal of Chemical and Engineering Data 14 (2) (1969) 235.

[109] V. Dribinski, A. Potter, A. Demyanenko, H. Reisler, Photodissociation dynamics of the CH_2Cl radical: Ion imaging studies of the Cl+ CH_2 channel, The Journal of Chemical Physics 115 (16) (2001) 7474–7484.

APPENDIX A

ATTEMPTED EXPERIMENTS

A.1 Preface

This appendix describes two attempted experiments which were both ultimately unsuccessful. Acetaldehyde and Ketene were the subject of investigation to take advantage of the new 2+1 REMPI scheme and analysis to extract speed dependent vector correlations. Both were experiments were plagued by strong nonreasonant signal at $m/z = 28$ caused by the CO($E \leftarrow X$) REMPI transition. In each subsection, the molecule will be introduced, the experimental methods will be reviewed, and any results will be presented. In the future, given the cause was the short wavelength needed for the CO($E \leftarrow X$) REMPI transition, the solution would be to employ an alternative REMPI scheme using longer wavelengths.

A.2 Acetaldehyde[1]

The goal of the Acetaldehyde study was to investigate the β_{vj} associated with the roaming mechanism. In order to understand the roaming mechanism, it is first necessary to review the basics of transition state theory. Transition state theory is a kinetic rate theory that can successfully model a large number of reactions and can accurate predict both kinetic rates and energy partitioning of experimental results.[94] Despite the successes of transition state theory, there are reactions which are poorly modeled by transition state theory such as roaming. In TST a reactions can occur via one of two types of transition states: a loose tranisiton state or a tight transition state which result in radical and molecular products respectively. Typically loose transition state products result in a statistical distributions of products while tight transition state products have non-statistical internal energy distributions due to the directed forces and torques at the transition state and in the exit channel. In the case of the roaming mechanism the products do not match either of these

[1]Reprinted with permission from Two roaming pathways in the photolysis of CH_3CHO between 328 and 308 nm by K. Lee; M.S. Quinn;A.T. Maccarone; K. Nauta; P.L. Houston; S.A. Reid; M.J.T. Jordan; S.H. Kable, 2014. Royal Society of Chemistry, 5, 4633, Copyright [2014] by Royal Society of Chemistry

cases. Instead the result is a blend of the two expected outcomes, molecular products that have low rotational and high vibrational excitation. In order to create a better TST it is necessary to understand the dynamics of these outliers. Since the roaming mechanism has a long lifetime, it is not possible to use the $\beta_{\mu v}$ or $\beta_{\mu j}$ to investigate the dynamics of the reaction. This is because when a molecule is first excited the ensemble is aligned based on the overlap between the transition dipole moment and electric field vector of the laser, as seen in Equation 2.14. After the molecules are aligned, they are not fixed in space and will begin to move. The longer the time it takes to dissociation, the more the molecules will rotate losing the inital alignment. However, β_{vj} is not dependent on μ and is unaffected by the dissociation lifetime. The β_{vj} is embedded into the products when the reaction actually occurs, which in the case of roaming is when the two roaming radical fragments recombine and react to form the molecular fragments. By investigating the β_{vj} , which provides information about the forces and torques that occur in the exit channel of a reaction, the stereodynamics of the roaming mechanism can be studied.

The roaming mechanism can be described as a frustrated dissociation where a fragment of a molecule partially dissociates from the parent molecule. Rather than leave the parent molecule, as is the case with a loose transition state, the fragment instead orbits the parent molecule until a particular orientation is achieved where the orbiting fragment can then react with the parent molecule.[95] The roaming mechanism can occur in any barrierless bond cleavage process regardless of both eh electronic state and whether or not the it is the lowest energetic pathway.[27] The first identification of the roaming mechanism occurred in 2004 by Townsend *et al.* in formaldehyde.[95]

Acetaldehyde, CH_3CHO , is the second simplest aldehyde only behind formaldehyde. The reaction dynamics of CH_3CHO have been investigated over a broad range of dissociation wavelengths ranging from 230 nm up to 328 nm. The photodissociation of CH_3CHO in this wavelength range is on the ground state surface. Initally the CH_3CHO is excited into the S_1 state where it then rapidly relaxes back into the S_0 ground state where the molecule can dissociate via several different mechanisms.[27] The photodissociation of CH_3CHO at 308 nm results in a wide rotational

distribution ranging from j_{CO} = 0 up to 64. The initial studies of CH_3CHO at 308 nm determined a branching ratio of 0.85:0.15 between the transition state mechanism and the roaming mechanism. This result was well in line with the branching ratio in the dissociation of formaldehyde of 0.87:0.13.[95, 96] More recently a study utilizing VELMI and in conjuction with quasi-classical trajectory calculations determined a very different branching ratio.[27, 97] The majority of the photofragments were concluded to originate from the roaming mechanism, not the traditional transition state. Since CH_3CHO is asymmetric, unlike formaldehyde, there are two different roaming channels. In the dissociation of CH_3CHO the branching ratio was assigned to originate mostly from the roaming of the methyl fragment around the formyl fragment, with minor channels associated with the tight transition state and the H fragment roaming around the CH_3CO cofragment. The branching ratio was determined to be 0.71:0.13:0.16, where the CH_3 roaming channel contribution was 71±12%, the H roaming channel contribution was 0.13±3%, and the tight transition state channel contributed 16±10%.[27, 97]

The dissociation wavelength was also varied in this VELMI experiment ranging from 308 nm up to 328 nm. By changing the photolysis energy, it is possible to determine the dissociation thresholds of the various reaction pathways. At 308 nm, 322 nm, and 325 nm the H roaming channel becoming increasingly less important relative to the methyl roaming channel. At 328 nm the bimodal rotational distribution becomes a single distribution and the low speed CO fragments associated with the H roaming channel is no longer be observed. The closing of the H roaming channel has been theoretically calculated to occur at 325.4 nm, which is well corroborated by this experimental result.[27, 97] The bimodal rotational distribution of CO at 308 nm, 322 nm, 325 nm, and 328 nm can be seen in Figure A.1, where the blue Boltzmann distribution (T = $340 \pm 30, 310 \pm 30, 300 \pm 100$, N/A) at low speeds corresponds to the H roaming channel and the red Boltzmann distribution (T = $2700 \pm 300, 2650 \pm 300, 2780 \pm 300, 2730 \pm 500$) at high speed corresponds to the methyl roaming channel. Additionally in Figure A.1, the rotational distributions are shown for both high and low j_{CO} . At the j_{CO} = 30 there are no CO products originating from the H roaming channel at all of the wavelengths. This result is very similar to the results of H

roaming in formaldehyde where there is very little rotational excitation.[95, 96]

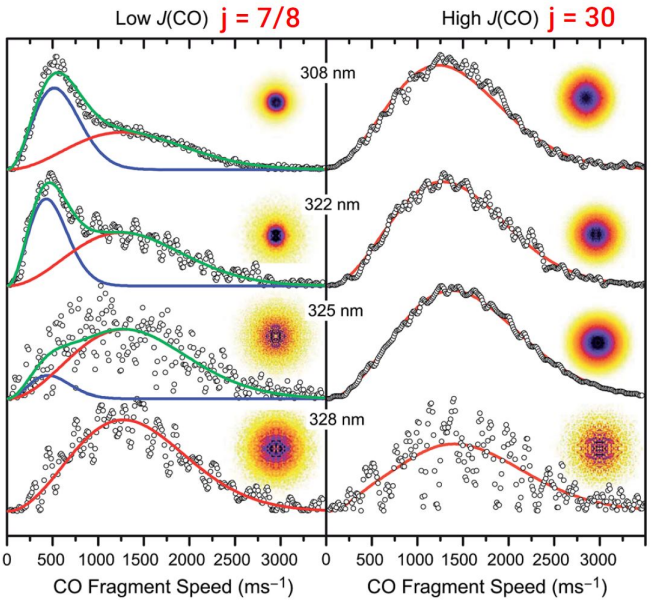

Figure A.1: CO images originating from the photodissociation of CH_3CHO at varying dissociation energies. The left panel refers to j_{CO} =7/8 and the right panel refers to j_{CO} =30. The red Boltzmann corresponds to methyl roaming and the blue Boltzmann corresponds to H roaming. This figure is adapted from Kim *et al.* [27][1]

All previous imaging studies of CH_3CHO used the $B(^1\Sigma^+) \leftarrow X(^1\Sigma^+)$ REMPI transition of CO, which can be seen in Figure 2.4 in Section 2.2.2 of the experimental. Due to the symmetry of both the ground and excited state, ($^1\Sigma^+$), it is possible to have a Q, O, and S branch in the REMPI spectrum. The intensity of these three states must be experimentally determined on a transition by transition basis. In the case of the $B(^1\Sigma^+) \leftarrow X(^1\Sigma^+)$ the Q-branch is 100× stronger than the S and O branches which are barely detectable using the available laser power. The Q-branch does is not rotationally aligned and thus is insensitive to $\beta_{\mu v}$ (and $\beta_{\mu j}$) which is dependent on j.[98, 99, 72] Due to the insensitivity of the probe laser in previous imaging experiments it was not possible to determine any vector properties of the roaming mechanism in acetaldehyde. In order to determine the β_{vj} the probe laser was changed from the often used $B(^1\Sigma^+) \leftarrow X(^1\Sigma^+)$ REMPI transition to the

$E(^1\Pi) \leftarrow X(^1\Sigma^+)$ REMPI transition. Since the E state of CO has a ($^1\Pi$) symmetry all five possible rotational branches O, P, Q, R, and S are populated at low j_{CO} as seen in Figure 2.5.

A.2.1 Experimental: Acetaldehyde

Acetaldehyde is readily available from Sigma Aldrich ($\geq$ 99.5%). The acetaldehyde was treated using the pump-freeze-thaw technique to degas the sample prior to use. As a liquid at room temperature acetaldehyde could easily be added to a glass bubbler and cooled to the correct temperatures to regulate the percent of acetaldehyde in the molecular beam based on the vapor pressure. Temperatures ranging from -50 to -70 °C were used to maintain percentages ranging from ~1% to ~3%.[100] Clustering of the acetaldehyde precursor was tested as a function of concentration in the flow. By imaging the CH_3 radical, described below, it was possible to see the clustering dependence which should present itself as a center dot of in CH_3 image. Helium flowed through the glass bubbler entraining a fraction of acetaldehyde into the flow. In Figure A.2 two different images are shown, an image with ~1% CH_3CHO and and image with ~3% entrained in to the helium flow. The corresponding translational energy distributions are shown for each image where red corresponds to a concentration of ~1% CH_3CHO and black corresponds to a concentration of ~3%. Based on the Figure A.2 it is apparent that there was small amounts of clustering of acetaldehyde.

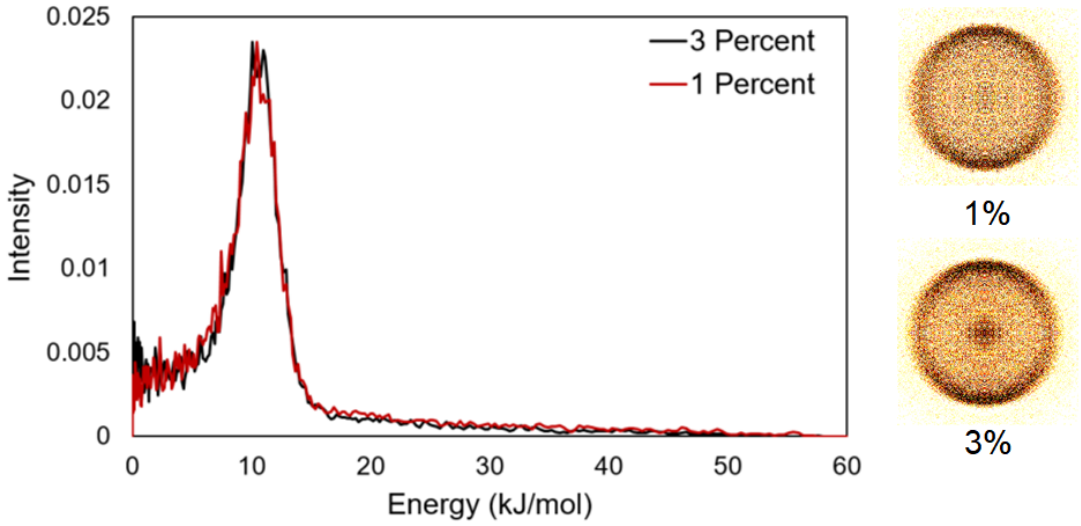

Figure A.2: The amount of clustering in CH_3CHO as a function of concentration is shown above. Two CH_3 radical images at concentrations of ~1% and ~3% are shown along with their corresponding translational energy distributions, shown as red and black respectively.

The intensity of the center of each image corresponds to the amount of clustering. In the translational energy distributions, this intensity will present itself near 0 kj mol$^-$1. When comparing the two concentrations, it is apparent that there is a small amount of clustering. On advice from Dr. Scott Kable stainless steel tubing was used instead of the typical Teflon tubing to connect the glass bubbler, outside the chamber, to the General Valve Series 9 pulse valve inside the source region of the chamber. The purpose of the stainless steel tubing was to reduce the clustering of acetaldehyde in the molecular beam.[101] The CH_3CHO/He flow is then pulsed into the chamber undergoing a free jet expansion rapidly cooling the parent molecules. The CH_3CHO molecules then enter the main chamber through a electroform skimmer collimating the molecular beam. Once the flow enters the main chamber it is first dissociated using wavelengths ranging from 288 nm to 308 nm. Once the CH_3CHO has been dissociated, either the CO or CH_3 fragmets are ionized via a 2+1 REMPI scheme. The pump-probe delay was set to ~50 ns. The majority of the CH_3CHO experiments utilized the $E(^1\Pi) \leftarrow X(^1\Sigma^+)$ 2+1 REMPI transition near 214 nm as the probe, while a small fraction of these experiments were conducted using the $B(^1\Sigma^+) \leftarrow X(^1\Sigma^+)$ 230 nm.[71, 72, 73] The

methyl fragment was probed at 333.4 nm using the CH_3 ($3p^2A_2''0_0^0$) transition.[102]

The 214 and 230 nm light were generated using the same method described above in Section 2.4.1. The 288 nm dissociation wavelength used R590 which generated 30 mJ/pulse of average dye power and 1.2 mJ/pulse of UV light. The 305 nm, 308 nm, and 310 nm dissociation wavelengths used R640 which generated 60 mJ/pulse and 5 mJ/pulse of UV light at 308 nm. The 333.4 nm CH_3 probe wavelength used DCM dye in DMSO/MeOH to generate ~25 mJ/pulse of dye power with ~1.5 mJ of UV light. In Figure A.3 the absorption cross section as a function of wavenumbers is shown.[28] The percentage of H roaming as a function of wavenumber at j_{CO} = 7/8 as red circles. The dotted vertical gray line represents the threshold energy for H roaming channel.[27]

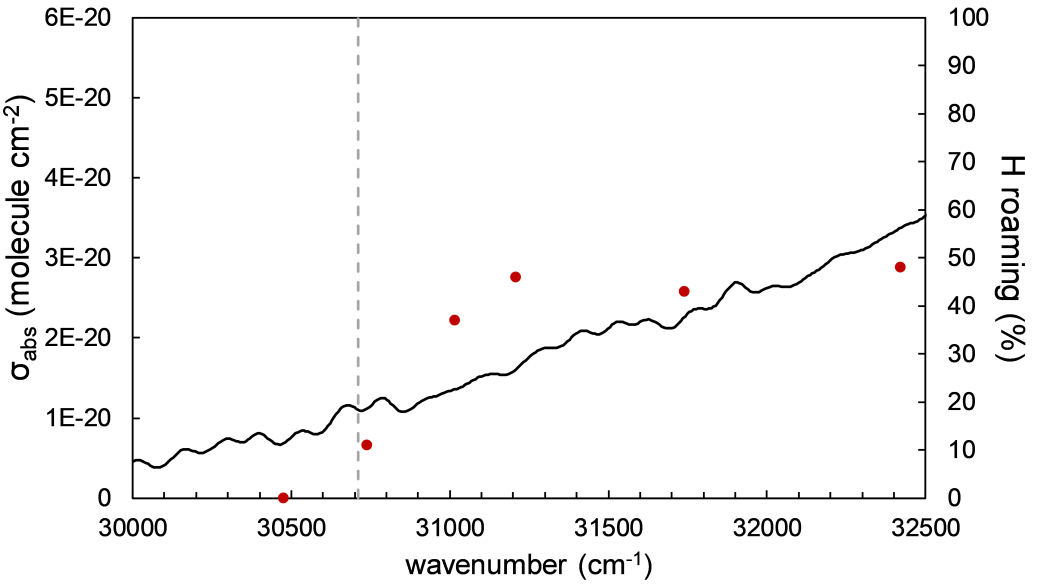

Figure A.3: The absorption cross section of CH_3CHO as a function of wavenumbers.[28] The percentage of H-roaming at j_{CO} = 7/8 is shown as red circles with the threshold energy for the H roaming channel shown as the gray vertical dotted line.[27]

A.2.2 Results and Discussion: Acetaldehyde

Testing the differences in dissociation wavelength on the methyl radical images. The initial wavelength used was 288 nm since the photodissociation OCS in conjuction with a nearby S(^1D)

could be used to overlap the pump and probe lasers with the molecular beam. At 288 nm a strong center dot was observed. Initally, this signal was assigned to clustering of CH_3CHO . Once the optical design and methodology was refined, other dissociation wavelengths were attempted at 305 nm, 308 nm, and 310 nm. While the overall S/N is clearly the best for the CH_3 image at 308 nm, the overall shape of the three images originating from these dissociation wavelengths is the same. In general the intensity at the center of the 288 nm image is no longer present under the same experimental conditions indicating that clustering was not the source of the low energy intensity in the 288 nm image.

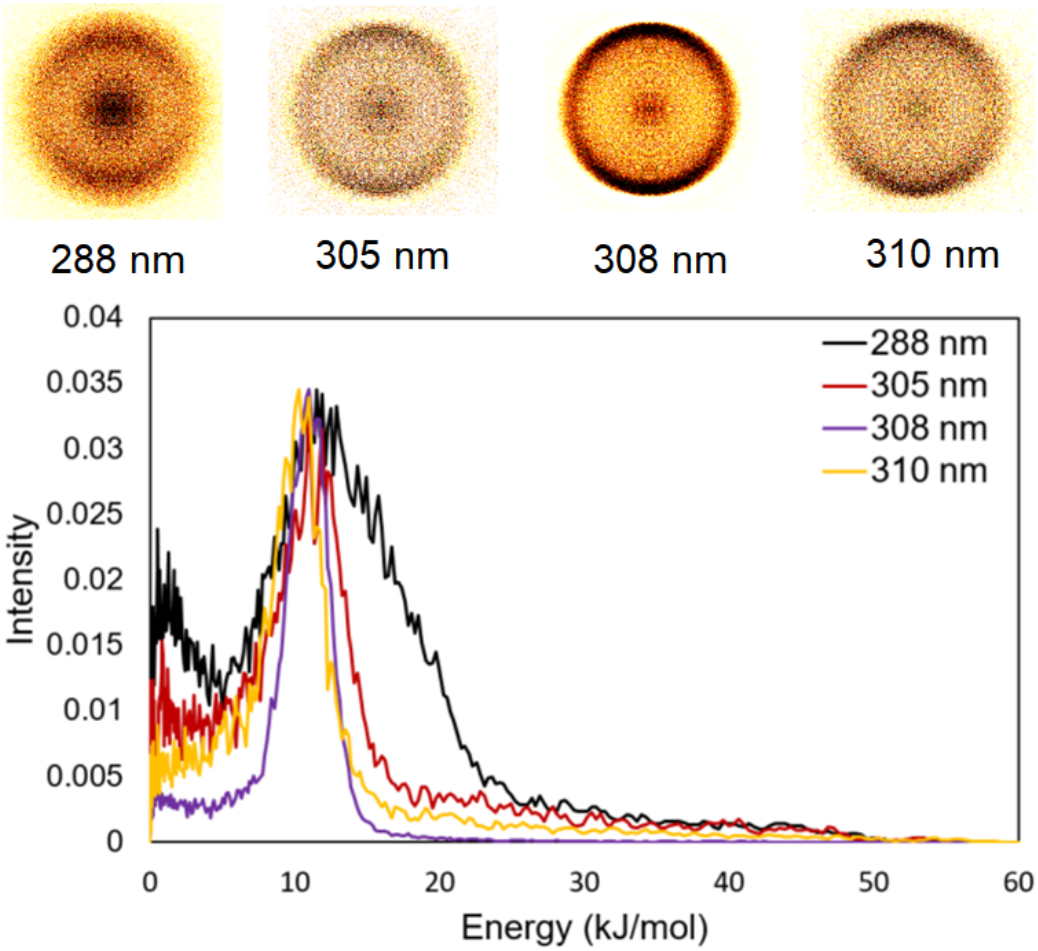

Figure A.4: The photodissociation of CH_3CHO as a function of wavelength. The total energy distributions and corresponding images are shown at the four dissociation wavelengths: 288 nm, 305 nm, 308 nm, and 310 nm. The 288 nm has strong intensity at very low energy which was assigned to CH_3 originating from the triple dissociation pathway shown in Equation A.1.

The intensity at the center of the 288 nm image was instead assigned to H atom originating from the triple dissociation of CH_3CHO shown in Equation A.1 where

$$CH_3CHO + \lambda_{h\nu}(\leq 293.9\ nm) \rightarrow CO + H + CH_3. \tag{A.1}$$

The wavelength dependent imaging study of the CH_3 fragment conjunction with the experiments on the concentration dependence of clustering, shown in Section A.2.1, indicated that under the experimental conditions used, clustering of CH_3CHO would not be an issue when imaging the

CO fragments. It was necessary to thoroughly verify there was no clustering of CH_3CHO in the molecular beam since CO fragments originating from the photodissociation of CH_3CHO clusters and those that originated from the roaming product channel will have similar isotropic, low speed fragments in the CO ion image.

Images of the CO fragments using the previously mentioned pump probe scheme at the varying dissociation wavelength were attempted. Unfortunately during the experiments there was a persistent nonresonant CO signal that was both pulse valve dependent and laser dependent. Based on the pulse valve dependence it was clear the CO signal originated from the CH_3CHO in the molecular beam. The signal was too strong to see any resonant two-color signal originating from the photodissociation of CH_3CHO . In Figure A.5, two total energy distributions are shown where the black distribution corresponds to two-color signal at 213.801 nm which corresponds to j_{CO} = 51, while the red distribution corresponds to the two color signal where the probe is at a nonresonant wavelength (213.810 nm). The near identical shape of the two different energy distributions indicates that there is no resonant signal present. Despite numerous attempts to dampen the nonresonant signal it was persistent.

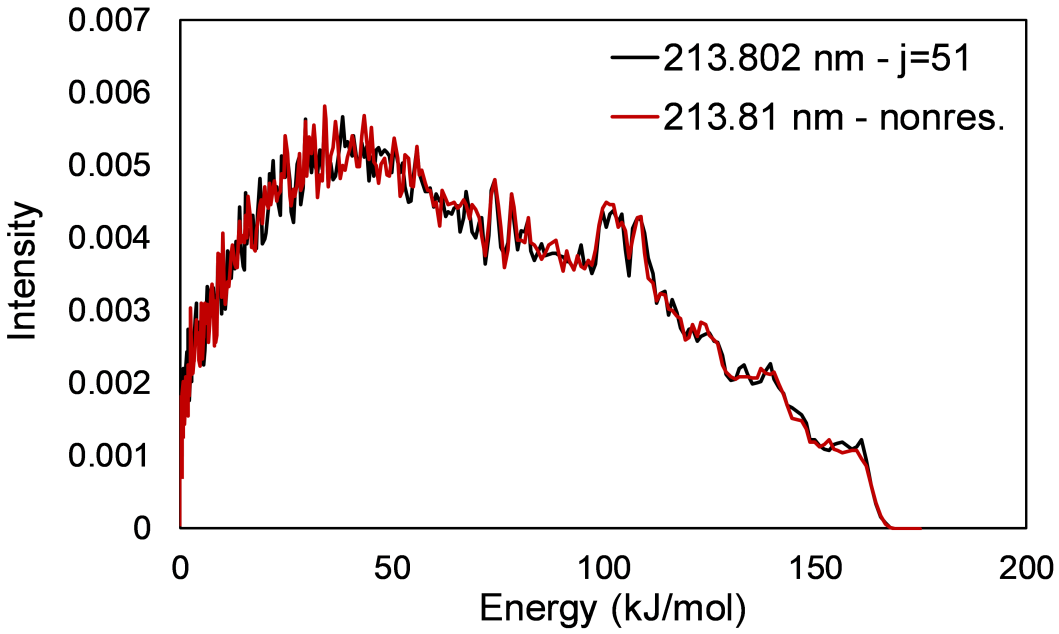

Figure A.5: Total energy distributions of CO orginating from the photodissociation of CH_3CHO near 288 nm. Two different probe wavelengths are shown, one at 213.802 nm which corresponds to $j_{CO} = 51$ and one at 213.81 nm which corresponds to a nonresonant CO wavelength. The intensity of the energy distributions has been area normalized.

A.3 Ketene

The goal of the ketene experiment was to measure speed dependent vector correlations, the same goal as the HN_3 experiments. Historically ketene has been used as a test case for statistical models to predict dissociation rate and product distributions of barrierless unimolecular reactions on a single potential energy surface.[103, 104, 105, 23] Variational Rice-Ramsperger-Kassel-Marcus (RRKM) theory has been able to successfully model the dissociation rates of ketene up to 6000 cm^{-1} above the dissociation threshold.[106] There has been only one measurement of speed dependent β_{vj} using neutral time-of-flight mass spectrometry.[107] Like the roaming mechanism, the dissociation of ketene has a long lifetime which results in the loss of any correlations related to μ leaving only the correlation between v and j. The photodissociation of ketene near 308 nm first excites ground state ketene from the S_0 surface to the S_1 surface where it rapidly internally converts back to the S_0 state resulting in highly vibrationally excited ketene.[103] A small fraction

of the excited ketene molecules can intersystem crossing to the triplet channel where the branching ratio between the $^3CH_2$:^{1} $CH_2(v = 0)$:^{1} $CH_2(v = 1)$ is 0.06:0.82:0.12 respectively.[23] The dissociation threshold for the $^1CH_2(v = 0)$ channel is 30116 cm^{-1}. Similarly to the CH_3CHO experiments, it was necessary to use the $E(^1\Pi) \leftarrow X(^1\Sigma^+)$ 2+1 REMPI transition to probe the CO fragments in order to see the β_{vj} .

A.3.1 Experimental: Ketene

Ketene was synthesized by the pyrolysis of acetic anhydride. Acetic anhydride is flowed over a hot filament (Osram-Sylvania air heater 016501) at a temperature of ~ 500°C. The ketene, water, and excess acetic anhydride from the pyroysis then traveled through a U-tube submerged in a dry ice/acetone bath where the water and unreacted acetic anhydride would solidify. The ketene exited the dry ice/acetone trap was trapped further down stream in a liquid nitrogen trap. Once trapped, the ketene was treated using the pump-freeze-thaw technique to degas the ketene sample. An experimental schematic of the synthesis is shown in Figure A.6.

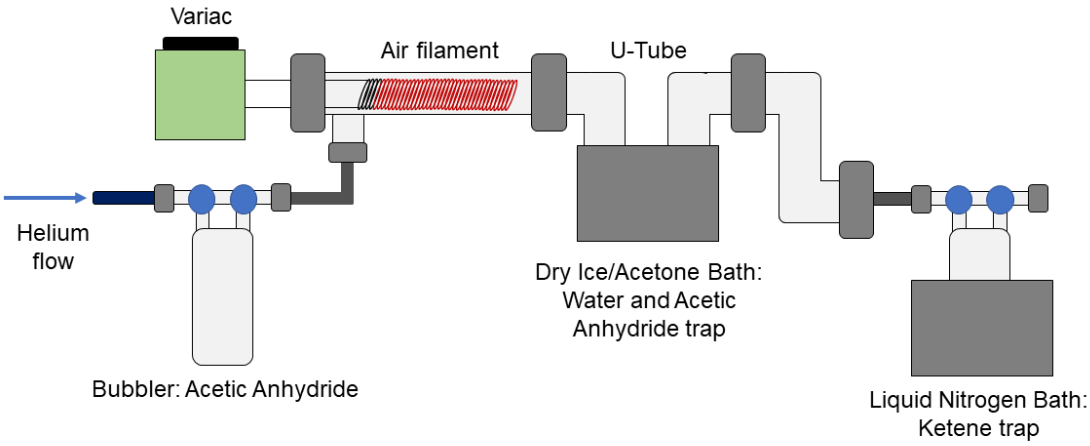

Figure A.6: An experimental schematic of the ketene synthesis.

The formation of ketene was verified by UV-vis. An example absorption spectrum of ketene overlaid with the absorption spectrum from Ref. [29] and is shown in Figure A.7.

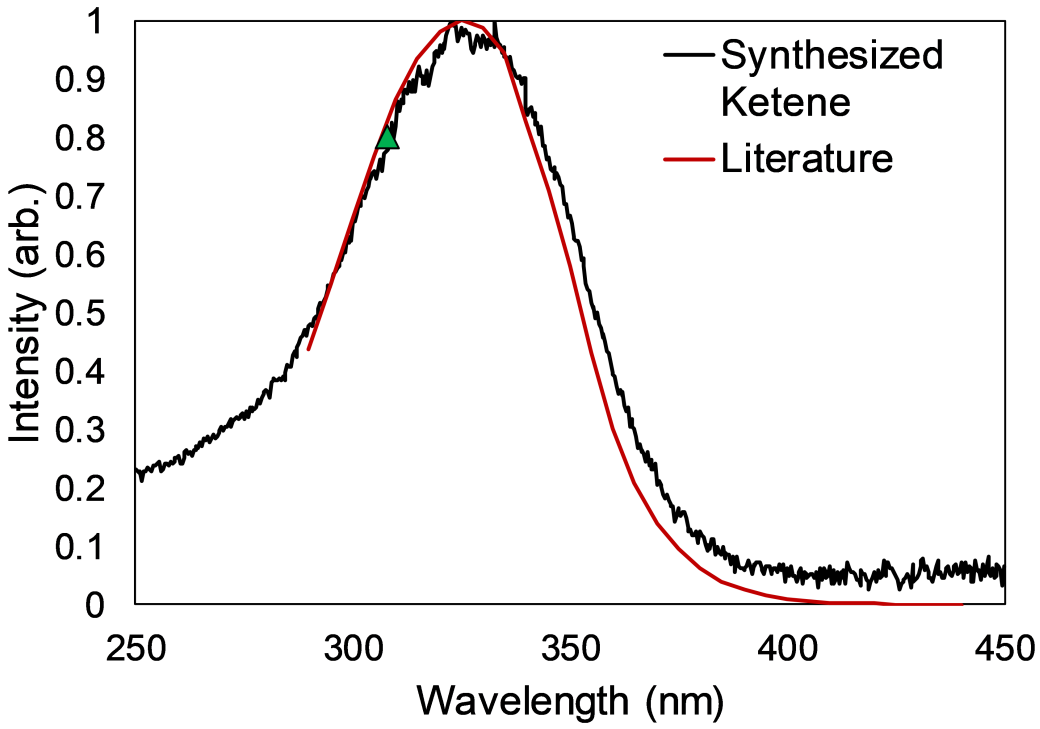

Figure A.7: The measured absorption of ketene compared to the absorption spectrum from Ref. [29]. The green triangle indicates 308 nm, the photodissociation wavelength used in this experiment.

During the experiment the ketene was kept in a liquid nitrogen/acetone bath at −96°C which resulted in a vapor pressure of ∼ 5% entrained in the helium flow.[108] The ketene/He flow entered the source region of the chamber where it underwent a free jet expansion and traveled through a electroform skimmer collimating the molecular beam as it entered the main chamber. The photodissociation of ketene at 308 nm used the same laser conditions mentioned in Section A.2.1. The CO fragments also used the same probe schemes at 214 nm and 230 nm mentioned in Section 2.4.1. While no attempts were made to image the CH_2 fragment, there is a 2+1 REMPI scheme for CH_2 ($\tilde{X}^3B_1$) at 311.80 nm which has been previously utilized in ion imaging.[109]

A.3.2 Results and Discussion: Ketene

Similar to the CH_3CHO study, images using the $E(^1\Pi) \leftarrow X(^1\Sigma^+)$ 2+1 REMPI transition near 214 nm images resulted in a strong non resonant CO signal that was pulse valve depen-

dent and laser dependent, but not wavelength dependent. The probe wavelength was then moved to $B(^1\Sigma^+) \leftarrow X(^1\Sigma^+)$ transition at 230 nm to replicate the experiments preformed in Komissarov *et al.* to determine if the probe wavelength or the experimental design was the issue.[23]

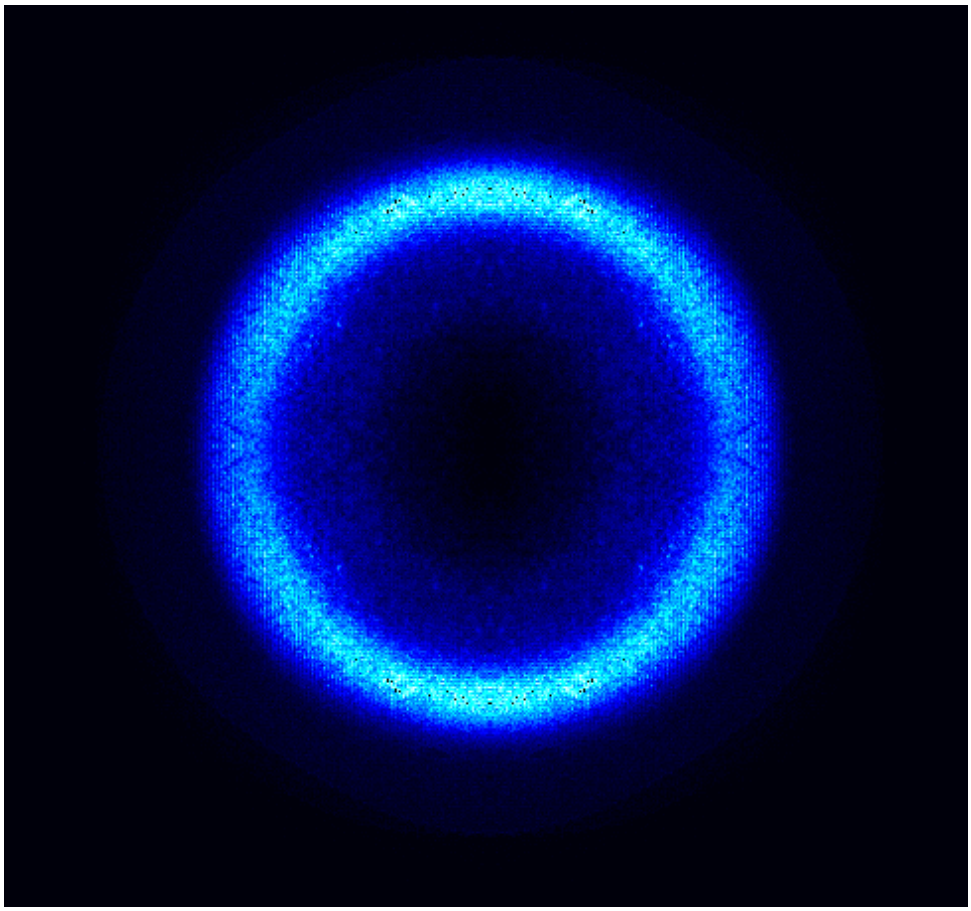

Figure A.8: The photodissociation of ketene at 308 nm. Above is a sliced image taken at 229.903 nm, the band head of the Q-branch of the $B(^1\Sigma^+) \leftarrow X(^1\Sigma^+)$.

The image shown above resembles the j=4 image presented in Komissarov *et al.* The intensity of the broad inner and outer rings are not well reproduced. The j=4 image from Komissarov has two main peaks which are nearly the same intensity. The ketene image collected here has very little intensity at the lower energy peak which corresponds to the $^1CH_2(v = 1)$ channel. The E_{trans} distributions from this work and Komissarov *et al.* are shown in Figure A.9.[23] The lack of

intensity at low translational energies is currently unknown.

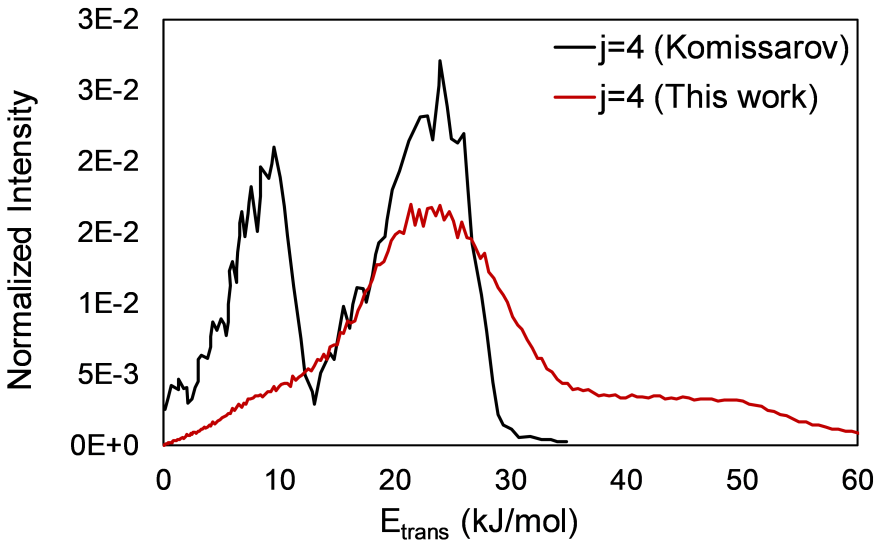

Figure A.9: The E_{trans} distribution from Figure A.8 is in red and the corresponding j=4 image from Komissarov *et al.* is shown in black. The intensities both both distributions are area normalized.[23]

A.4 Conclusion

Two attempted experiments involving acetaldhyde and ketene were attempted. Both of experiments were unable to overcome a pulse valve dependent, nonresonant CO background. The intensity of the background was very strong which lead to difficulty in detecting resonant CO signal using the $E(^1\Pi) \leftarrow X(^1\Sigma^+)$ 2+1 REMPI transition. The acetaldehyde experiments were able to detect the CH_3 fragment at 333.4 nm using the CH_3 ($3p^2A_2''0_0^0$) transition.[102] The molecular beam of acetaldehyde was verified to contain no clusters. This was determined by comparing the center spot intensity CH_3 ion images at different concentrations. Additionally the triple dissociation channel of acetaldehyde at the dissociation wavelength of 288 nm. The ketene experiments were successfully able to replicate measurements from the literature using the $B(^1\Sigma^+) \leftarrow X(^1\Sigma^+)$ 2+1 REMPI transition near 230 nm. Few attempts were made to use the nearby $C(^1\Sigma^+) \leftarrow X(^1\Sigma^+)$ 2+1 REMPI transition of CO. The nearby C state of CO, near 217 nm, was chosen due to its par-

ticularly strong S branch intensity for a $(^1\Sigma^+) \leftarrow (^1\Sigma^+)$ transition. This strong intensity has been attributed to intensity borrowing from the E state of CO.[21] Unfortunately due to the similarity in wavelengths to the $E(^1\Pi) \leftarrow X(^1\Sigma^+)$ 2+1 REMPI transition, the nonresonant signal persisted. Any future attempts at these experiments would require a different probing scheme that would avoid the 214 nm region. Possible schemes include using a 2+2 or 2+1′ REMPI process through the A state of CO. In order to use a 2+1′ REMPI scheme in the A state, it is necessary to excite to the CO(v=7) state in the A state. At these energies it would is theoretically possible to use a single 266 nm photon to ionize the excited CO fragment. Since the A state is a valence state, as opposed to the Rydberg states (B and E states) used in this dissertation it is necessary to carefully consider the Franck-Condon factor between the ground X and excited A states of CO. The Franck-Condon factor between the CO(X,v=0) and CO(A,v=7) states has been roughly calculated to be ~0.03 using the diatomic constants in the NIST webbook.[20]